

Copyright
by
Lindley Christin Graham
2015

The Dissertation Committee for Lindley Christin Graham
certifies that this is the approved version of the following dissertation:

**Adaptive Measure-Theoretic Parameter Estimation for
Coastal Ocean Modeling**

Committee:

Clint Dawson, Supervisor

Troy Butler

Irene Gamba

Omar Ghattas

Robert Moser

**Adaptive Measure-Theoretic Parameter Estimation for
Coastal Ocean Modeling**

by

Lindley Christin Graham, B.S.A.E.; M.S.C.S.E.M.

DISSERTATION

Presented to the Faculty of the Graduate School of
The University of Texas at Austin
in Partial Fulfillment
of the Requirements
for the Degree of

DOCTOR OF PHILOSOPHY

THE UNIVERSITY OF TEXAS AT AUSTIN

August 2015

Dedicated to my grandparents and the trailblazers that came before me
because of you this is possible.

Acknowledgments

I cannot adequately thank everyone who has helped me to get to and through graduate school. However, I will attempt to at least mention some of them. I would like to thank my family, especially my parents, for their encouragement and support of my interests in math and science, and for instilling in me the value of academics and hard work. I would like to thank my undergraduate professors at the my Alma mater, the Massachusetts Institute of Technology. I would like thank my undergraduate advisor Youssef Marzouk for co-teaching 16.90 *Computational Methods in Aerospace Engineering*, which introduced me to the fields of computational science and uncertainty quantification; he was instrumental in my decision to attend the University of Texas at Austin, and has provided advice for which I am extremely grateful. I would like to also thank Karen Willcox for her excellent instruction, advice, and encouragement; she was also instrumental in my decision to pursue graduate school. I would also like to thank Nicholas Roy for teaching me version control; this is an essential skill. I would also like to thank all those at my Alma mater who provided support in my life outside of academics: Abigail Francis, Sean Delmore, Jarek Koniusz and the many fencers and coaches (both collegiate and non-collegiate).

I wish to acknowledge and thank The National Science Foundation, The

University of Texas at Austin, The Institute for Computational Engineering and Sciences (ICES), and the Computational Hydraulics Group (CHG) for their support. The faculty, research scientists, postdoctoral associates, staff, and graduate students of ICES and CHG have been a font of knowledge, mentorship, and fellowship, without which I would not be at this point today. I would like to especially thank my committee: Troy Butler, Irene Gamba, Omar Ghattas, Robert Moser, and my supervisor Clint Dawson; your guidance through mentorship, lectures, office meetings, and informal discussions has been invaluable. As I have progressed through my studies I have become ever increasingly grateful for the role Clint Dawson has played as my advisor; thank you for the numerous discussions, guidance, and unwavering support. Thank you for encouraging me to attend ICES and for your influence in my understanding of many subjects most notably functional analysis, hurricane storm surge, and coastal ocean modeling. I wish to especially thank Troy Butler who has in many ways been a co-advisor in all but name; thank you for numerous lengthy discussions, specifically those regarding measure-theoretic stochastic inverse problems; and for your continued involvement after your departure from ICES to a tenure-track position. Without either of you this work would not exist. Joannes Westerink, thank you for valuable insights regarding Manning's n which ultimately led to the idea for the mesoscale parameterization of Manning's n presented herein. Seizo Tanaka and Zachary Cobell, thank you for developing Griddata and teaching me how to use it. Casey Dietrich, thank you for teaching me how to run ADCIRC. Discussions

with Don Estep also provided valuable insights into the characterization of the condition of the stochastic inverse problem. Kyle Mandli, thank you for your proselytization of Python.

I would like to extend a special thank you to my academic big siblings in the Computational Hydraulics Group: Talea Mayo, Jessica Meixner, Steve Mattis, and Nishant Panda. I would like to thank Kathryn Farrell-Maupin and Corey Bryant for many fruitful scientific and mathematical discussions. I cannot list all of my friends and fellow graduate students who have helped me in more ways than I can count, but I would like to thank Matthias Taus, Truman Ellis, Nicholas Fitzsimmons, Jesse Kelly, Nora Deram, Pearl Flath, Rebecca Morrison, and Juan Diego Rodriguez. Of my friends and mentors outside of ICES I must thank Asif Syed Hassan, Shane Whalley, Naomi Seyfer, and Sarah Abraham; y'all are family to me. I am grateful and honored to call you friends.

Finally, I would like to thank the trailblazers, the only ones, and the firsts, especially those from underrepresented groups; thank you for your tenacity and sacrifice. You made this possible.

This material is based upon work supported by the National Science Foundation Graduate Research Fellowship under Grant No. DGE-11100007. Any opinion, findings, and conclusions or recommendations expressed in this material are those of the author(s) and do not necessarily reflect the views of the National Science Foundation. The author also acknowledges the Texas Advanced Computing Center (TACC) at The University of Texas at Austin for

providing HPC resources that have contributed to the research results reported within this work.

Adaptive Measure-Theoretic Parameter Estimation for Coastal Ocean Modeling

Publication No. _____

Lindley Christin Graham, Ph.D.
The University of Texas at Austin, 2015

Supervisor: Clint Dawson

Since Hurricane Katrina (2005), there has been a marked increase in the quantity of field observations gathered during and after hurricanes. There has also been an increased effort to improve our ability to model hurricanes and other coastal ocean phenomena. The majority of death and destruction due to a hurricane is from storm surge. The primary controlling factor in storm surge is the balance between the surface stress due to the wind and bottom stress. Manning's formula can be used to model the bottom stress; the formula includes the Manning's n coefficient which accounts for momentum loss due to bottom roughness and is a spatially dependent field. It is impractical to measure Manning's n over large physical domains. Instead, given a computational storm surge model and a set of model observations, one may formulate and solve an inverse problem to determine probable Manning's n fields using observational data, which in turn can be used for predictive simulations. On land, Manning's n may be inferred from land cover classification maps. We leverage

existing land cover classification data to determine the spatial distribution of land cover classifications which we consider certain. These classifications can be used to obtain a parameterized mesoscale representation of the Manning's n field. We seek to estimate the Manning's n coefficients for this parameterized field.

The inverse problem we solve is formulated using a measure-theoretic approach; using the ADvanced CIRCulation model for coastal and estuarine waters as the forward model of storm surge. The uncertainty in observational data is described as a probability measure on the data space. The solution to the inverse problem is a non-parametric probability measure on the parameter space. The goal is to use this solution in order to measure the probability of arbitrary events in the parameter space. In the cases studied here the dimension of the data space is smaller than the dimension of the parameter space. Thus, the inverse of a fixed datum is generally a set of values in parameter space. The advantage of using the measure-theoretic approach is that it preserves the geometric relation between the data space and the parameter space within the probability measure. Solving an inverse problem often involves the exploration of a high-dimensional parameter space requiring numerous expensive forward model solves. We use adaptive algorithms for solving the stochastic inverse problem to reduce error in the estimated probability of implicitly defined parameter events while minimizing the number of forward model solves.

Table of Contents

Acknowledgments	v
Abstract	ix
List of Tables	xiii
List of Figures	xiv
Chapter 1. Introduction	1
1.1 Background and Motivation	1
1.2 Research Contributions	4
1.3 Outline	7
Chapter 2. The Advanced Circulation Model for Oceanic, Coastal, and Estuarine Waters (ADCIRC)	8
2.1 Modeling the Shallow Water Equations in ADCIRC	9
2.2 Modeling Flow Resistance in ADCIRC	11
Chapter 3. A Measure-Theoretic Framework for Stochastic In- verse Problems	16
3.1 Formulating the Stochastic Inverse Problem	17
3.2 Solving the Inverse Problem using Sigma-Algebras on Contour Maps (SACOM)	21
3.2.1 Existence and Uniqueness	22
3.2.2 Approximation	24
3.2.3 Error	26
3.2.4 Characterizing the Condition of the Inverse Problem . .	27

Chapter 4. Numerical Results	32
4.1 Definition of the Stochastic Inverse Problem for Manning's n parameter using ADCIRC	32
4.2 Defining a Mesoscale Representation of the Manning's n Coefficient	34
4.3 Inlet Case Study	38
4.3.1 Two Dimensional Parameter Space	38
4.3.2 Three Dimensional Parameter Space	43
4.4 Hurricane Gustav Case Study	53
4.4.1 Subdomain Parameter Space	59
4.4.2 Subdomain Data Space	59
4.4.3 Subdomain Parameter Estimation for Bay St. Louis	67
Chapter 5. Goal-Oriented Adaptive Sampling	79
5.1 Probability Based Adaptive Sampling	81
5.2 Probability Based Adaptive Sampling Results	82
5.3 Convergence of Adaptive Sampling	84
Chapter 6. Conclusion and Future Work	90
6.1 Conclusion	90
6.2 Future Work	95
Appendices	99
Appendix A. Modeling Flow Resistance with Manning's n	100
Appendix B. Scientific Software Contributions	107
Bibliography	112
Vita	133

List of Tables

2.1	Example ranges of values of LA-GAP Manning's n coefficients [15].	15
4.1	Manning's n Ranges for the Idealized Inlet.	39
4.2	The prediction of the time of inundation for the idealized inlet [32].	43
4.3	Manning's n values for C-CAP classification. Reproduced from [31].	55
4.4	Dominant land cover classifications for the subdomain.	60
4.5	Manning's n coefficient ranges for the subdomain.	60
4.6	Number of possible data spaces for the subdomain.	64
4.7	QoI map skew numbers for the subdomain.	67
5.1	Statistics of adaptive volume estimates for the idealized inlet for (q_1, q_2) for 20 sets of samples.	89
5.2	Statistics of adaptive volume estimates for the idealized inlet for (q_1, q_6) for 20 sets of samples.	89

List of Figures

2.1	An illustration of the the total water column height $H = h + \zeta$ where h is the bathymetric depth, and ζ is the free surface above the geoid or datum.	9
2.2	High resolution land cover classification data.	15
3.1	The response surface for a map $Q : \Lambda \rightarrow \mathcal{D}$ between a 2-dimensional parameter space and a 1-dimensional data space. The inverse image of $Q(\lambda)$ the contour $Q^{-1}(Q(\lambda))$. This illustrates an inherently set-valued inverse map Q^{-1} . This graphic has been reproduced with permission from Drs. Butler and Estep.	19
3.2	The response surface for a map $Q : \Lambda \rightarrow \mathcal{D}$ between a 2-dimensional parameter space and a 1-dimensional data space. We can use a <i>transverse parameterization</i> to identify each member $l \in \mathcal{L}$ of the set of equivalence classes \mathcal{L} with a particular contour C_l . This graphic has been reproduced with permission from Drs. Butler and Estep.	20
3.3	The response surface for a map $Q : \Lambda \rightarrow \mathcal{D}$ between a 2-dimensional parameter space and a 1-dimensional data space. The distribution on output values $\rho_{\mathcal{D}}$ and the corresponding marginal probability across the generalized contours. This graphic has been reproduced with permission from Drs. Butler and Estep.	23
3.4	Illustration of the Standard Choice for Ansatz where \mathcal{L} is the space of equivalence classes, $l \in \mathcal{L}$ is an index of \mathcal{L} , and $\pi_{\mathcal{L}}^{-1}(l)$ is a particular generalized contour in Λ . This graphic has been reproduced with permission from Drs. Butler and Estep. . . .	24
3.5	Illustration of linear QoI maps Q of varying skewness where q_i is a d-dimensional vector and q_{span} represents the hyperplane associated with $\text{span} \{ \{q_1, \dots, q_d\} \setminus q_i \}$. In (a) the generalized contours are <i>not</i> geometrically distinct. In (b)-(d) the generalize contours are geometrically distinct and progress from highly skewed (b) to perfectly unskewed (d).	29
4.1	The grid scale at the red node is shown as the red dashed box. The centroids are shown in blue. The underlying pixels are outlined in gray and the pixels within the grid scale are green. This is a modified figure from [26].	35

- 4.2 This demonstrates how to construct a prototypical mesoscale representation of Manning’s n values from basis vectors defining a linear mapping from land classification types. Top Left: Basis Vector 1. Top Right: Basis Vector 2. Bottom Left: Basis Vector 3. Bottom Right: Spatially averaged Manning’s n field using synthetic data. Note that in the inlet area (right-hand side) this is considered a shallow area and two land classification types are heavily mixed. Compare this to the deeper (left-hand) side of the domain where it is common practice to assign a single land classification type with lower Manning’s n value in such areas. 37
- 4.3 The physical domain for the idealized inlet. Top Left: Bathymetry of the physical domain Ω in Eq. (2.1.1) and Eq. (2.1.2) with observation stations marked by circles. Bottom Left: Discretization of the domain. Right: The xy -coordinates of observation stations in Ω for observing QoI. Observations of a QoI from the i^{th} observation station are designated $q_i(\lambda)$. We can then choose to examine a particular QoI map, e.g., $Q(\lambda) = (q_1(\lambda), q_5(\lambda), q_{12}(\lambda))$ or $Q(\lambda) = (q_1(\lambda), q_7(\lambda))$. Recall that $Q(\lambda) \in \mathbb{R}^d$ and $d \leq n$, so there are at most n geometrically distinct observation stations. 47
- 4.4 Left: The QoI map $Q(\lambda) = (q_1(\lambda))$ of the maximum elevation measured at station 1 computed on a finite element mesh that matches the mesoscale representation of Manning’s n . Right: The QoI map on the refined finite element mesh shown in Figure 4.3. Note the difference colorbar scales, smoothness of the responses, and changes in the gradient due to the use of the refined finite element mesh. 48
- 4.5 The estimated data domain $\mathcal{D} := Q(\Lambda) = \{q_1(\Lambda), q_n(\Lambda)\}$ for $n = 2$ (left), $n = 5$ (center), $n = 6$ (right) computed with a regular 121^2 grid of samples. The reference Q_{ref} for $(\lambda_1, \lambda_2) = (0.107, 0.106)$ is marked in red. 48
- 4.6 An illustration of a partitioning $\{I_i\}_{i=1}^9 \subset \mathcal{D}$ of $\mathcal{D} := Q(\Lambda)$ where there exists an $I_i = R_{ref}$ show in red. Q_{ref} is illustrated by a red dot. If we use this partition to create a simple function approximation of $\rho_{\mathcal{D}}$ where $\rho_{\mathcal{D}}$ is uniform on R_{ref} we can exactly represent $\rho_{\mathcal{D}}$ by $\rho_{\mathcal{D},9}$ with the partitioning of \mathcal{D} illustrated here. 49
- 4.7 Top Row: The approximation of ρ_{Λ} on for $Q(\lambda) = (q_1(\lambda), q_2(\lambda))$, $(q_1(\lambda), q_5(\lambda))$, and $(q_1(\lambda), q_6(\lambda))$ for the first, second, and third columns respectively where $\lambda_{ref} = (\lambda_1, \lambda_2) = (0.107, 0.106)$ is marked by a black dot. Bottom Row: The observation stations in the physical domain for $Q(\lambda) = (q_1(\lambda), q_2(\lambda))$, $(q_1(\lambda), q_5(\lambda))$, and $(q_1(\lambda), q_6(\lambda))$ for the first, second, and third columns respectively. 49

4.8	The set $Q(\Lambda) = (q_1(\Lambda), q_5(\Lambda), q_{12}(\Lambda))$ for $\Lambda = [-900, 1500] \times [0.07, 0.15] \times [0.1, 0.2]$. The points $Q(-750.0, 0.118, 0.135)$ and $Q(1200.0, 0.146, 0.128)$ are denoted by a red circle and green triangle, respectively.	50
4.9	Marginal plots of the approximation of $P_{\Lambda, N}(R_k)$ for the map $Q(\lambda) = (q_1(\lambda), q_5(\lambda))$ computed by inverting a uniform probability measure centered on Q_{ref} on 20^3 cubes partitioning Λ . The marginals for the λ_1, λ_2 - (left), λ_1, λ_3 - (middle), and λ_2, λ_3 - planes (right), respectively. The reference, Q_{ref} and $\lambda_{ref} = (-600.0, 0.073, 0.119)$ is denoted by red circles respectively.	50
4.10	Marginal plots of the approximation of $P_{\Lambda}(R_k)$ for the map $Q(\lambda) = (q_1(\lambda), q_5(\lambda), q_2(\lambda))$ computed by inverting a uniform probability measure centered on Q_{ref} on 20^3 cubes partitioning Λ . The marginals for the λ_1, λ_2 - (left), λ_1, λ_3 - (middle), and λ_2, λ_3 - planes (right), respectively. The reference Q_{ref} and $\lambda_{ref} = (-600.0, 0.073, 0.119)$ is denoted by red circles.	51
4.11	Marginal plots of the approximation of $P_{\Lambda}(R_k)$ for $Q(\lambda) = (q_1(\lambda), q_5(\lambda), q_{12}(\lambda))$ computed by inverting a uniform probability measure centered on Q_{ref} on 20^3 cubes partitioning Λ . The marginals for the λ_1, λ_2 - (left), λ_1, λ_3 - (middle), and λ_2, λ_3 - (right) planes, respectively. The reference Q_{ref} and $\lambda_{ref} = (-750.0, 0.118, 0.135)$ is denoted by red circles.	51
4.12	Marginal plots of the approximation of $P_{\Lambda}(R_k)$ for $Q(\lambda) = (q_1(\lambda), q_5(\lambda), q_{12}(\lambda))$ computed by inverting a uniform probability measure centered on Q_{ref} on 20^3 cubes partitioning Λ . The marginals for the λ_1, λ_2 - (left), λ_1, λ_3 - (middle), and λ_2, λ_3 - (right) planes, respectively. The reference, Q_{ref} and $\lambda_{ref} = (1200.0, 0.146, 0.128)$ is denoted by red circles.	52
4.13	Bathymetry/topography (m) of the full domain mesh in southeastern Louisiana.	56
4.14	Manning's n values of the full domain mesh in southeastern Louisiana.	56
4.15	The physical domain for the subdomain. Top Left: Bathymetry of the physical domain Ω in Eq. (2.1.1) and Eq. (2.1.2). Top Right: Discretization of the domain. Bottom: The Manning's n field extracted from the full domain.	58

4.16	This shows the mesoscale representation of Manning's n values from basis vectors defining a linear mapping from land classification types for the subdomain. Top Left: Basis Vector 1. Top Right: Basis Vector 2. Middle Left: Basis Vector 3. Right Left: Basis Vector 4. Bottom: Basis Vector 5. Note the first four basis vectors correspond to $\lambda_1, \lambda_2, \lambda_3, \lambda_4$ while the fifth is held constant.	61
4.17	The 16 clusters in Λ used in the preliminary study of the subdomain, where $\lambda^{(k)} = (\lambda_1, \lambda_2, \lambda_3, \lambda_4)$. Left: In order from top to bottom $(\lambda_1, \lambda_2), (\lambda_1, \lambda_4), (\lambda_2, \lambda_4)$. Right: In order from top to bottom $(\lambda_1, \lambda_3), (\lambda_2, \lambda_3), (\lambda_3, \lambda_4)$	63
4.18	Maximum difference in subdomain water elevation over a set of 80 preliminary model evaluations. Values shown are $(\max_k(Y_i^{(k)}) - \min_k(Y_i^{(k)}))$ in $[m]$ where $Y_i^{(k)} = Y_i(\lambda^{(k)})$ is the maximum water elevation at a finite element node i for the k^{th} parameter value $\lambda^{(k)} = (\lambda_1^{(k)}, \lambda_2^{(k)}, \lambda_3^{(k)}, \lambda_4^{(k)})$. Note that to show subtle variations in the bay the color scale has been reduced.	65
4.19	Left: Maximum water elevation observation stations with the top 10 QoI map skew numbers. Stations 11, 12, 14, 16, and 17 are shown in blue. Stations 191 and 192 are shown in white. Station 160 is shown in red. Finally, station 40 is shown in green. Right: Optimal maximum water elevation observation stations (11, 40, 160, 191). Bottom: Maximum difference in subdomain water elevation. See Figure 4.18.	66
4.20	The data domain $\mathcal{D} = \text{convhull}(Q(\lambda^{(k)}))$ for the subdomain where $Q = (q_1, q_2, q_3, q_4)$ for stations 11, 40, 160, 191 respectively. Left: In order from top to bottom $(q_1, q_2), (q_1, q_4), (q_2, q_4)$. Right: In order from top to bottom $(q_1, q_3), (q_2, q_3), (q_3, q_4)$	68
4.21	The uniform samples in the parameter space for the subdomain where $\lambda = (\lambda_1, \lambda_2, \lambda_3, \lambda_4)$ and $\lambda_{ref} = (0.1523, 0.1751, 0.1561, 0.0269)$ is marked in magenta. The samples are colored by $\rho_{\mathcal{D}}(Q)$. Left: In order from top to bottom $(\lambda_1, \lambda_2), (\lambda_1, \lambda_4), (\lambda_2, \lambda_4)$. Right: In order from top to bottom $(\lambda_1, \lambda_3), (\lambda_2, \lambda_3), (\lambda_3, \lambda_4)$	70
4.22	The propagation of uniform samples in the parameter space for the subdomain for optimal stations 11, 40, 160, 191 where $Q = (q_1, q_2, q_3, q_4)$ and Q_{ref} is marked in magenta. The samples are colored by $\rho_{\mathcal{D}}(Q)$. Left: In order from top to bottom $(q_1, q_2), (q_1, q_4), (q_2, q_4)$. Right: In order from top to bottom $(q_1, q_3), (q_2, q_3), (q_3, q_4)$	71

4.23	The uniform samples in the data space for the subdomain for suboptimal stations 16, 40, 22, 88 where $Q = (q_1, q_2, q_3, q_4)$ and Q_{ref} is marked in magenta. The samples are colored by $\rho_{\mathcal{D}}(Q)$. Left: In order from top to bottom $(q_1, q_2), (q_1, q_4), (q_2, q_4)$. Right: In order from top to bottom $(q_1, q_3), (q_2, q_3), (q_3, q_4)$	72
4.24	Plots of the marginals of ρ_{Λ} using uniform samples for optimal stations 11, 40, 160, 191 . Here, $\rho_{\mathcal{D}}$ is defined as a uniform density on a small rectangular box centered at the reference QoI values associated with $\lambda_{ref} = (0.1523, 0.1751, 0.1561, 0.0269)$. The reference value is illustrated by a white circle. Left: In order from top to bottom $(\lambda_1, \lambda_2), (\lambda_1, \lambda_4), (\lambda_2, \lambda_4)$. Right: In order from top to bottom $(\lambda_1, \lambda_3), (\lambda_2, \lambda_3), (\lambda_3, \lambda_4)$	74
4.25	Plots of the marginals of ρ_{Λ} using uniform samples for near optimal stations 16, 40, 160, 192 . Here, $\rho_{\mathcal{D}}$ is defined as a uniform density on a small rectangular box centered at the reference QoI values associated with $\lambda_{ref} = (0.1523, 0.1751, 0.1561, 0.0269)$. The reference value is illustrated by a white circle. Left: In order from top to bottom $(\lambda_1, \lambda_2), (\lambda_1, \lambda_4), (\lambda_2, \lambda_4)$. Right: In order from top to bottom $(\lambda_1, \lambda_3), (\lambda_2, \lambda_3), (\lambda_3, \lambda_4)$	75
4.26	Plots of the marginals of ρ_{Λ} using uniform samples for suboptimal stations 16, 40, 22, 88 . Here, $\rho_{\mathcal{D}}$ is defined as a uniform density on a small rectangular box centered at the reference QoI values associated with $\lambda_{ref} = (0.1523, 0.1751, 0.1561, 0.0269)$. The reference value is illustrated by a white circle. Left: In order from top to bottom $(\lambda_1, \lambda_2), (\lambda_1, \lambda_4), (\lambda_2, \lambda_4)$. Right: In order from top to bottom $(\lambda_1, \lambda_3), (\lambda_2, \lambda_3), (\lambda_3, \lambda_4)$	76
4.27	Plots of the marginals of ρ_{Λ} using uniform samples for stations 16, 40, 22. Here, $\rho_{\mathcal{D}}$ is defined as a uniform density on a small rectangular box centered at the reference QoI values associated with $\lambda_{ref} = (0.1523, 0.1751, 0.1561, 0.0269)$. The reference value is illustrated by a white circle. Left: In order from top to bottom $(\lambda_1, \lambda_2), (\lambda_1, \lambda_4), (\lambda_2, \lambda_4)$. Right: In order from top to bottom $(\lambda_1, \lambda_3), (\lambda_2, \lambda_3), (\lambda_3, \lambda_4)$	77
4.28	Plots of the marginals of ρ_{Λ} using uniform samples for stations 16, 40. Here, $\rho_{\mathcal{D}}$ is defined as a uniform density on a small rectangular box centered at the reference QoI values associated with $\lambda_{ref} = (0.1523, 0.1751, 0.1561, 0.0269)$. The reference value is illustrated by a white circle. Left: In order from top to bottom $(\lambda_1, \lambda_2), (\lambda_1, \lambda_4), (\lambda_2, \lambda_4)$. Right: In order from top to bottom $(\lambda_1, \lambda_3), (\lambda_2, \lambda_3), (\lambda_3, \lambda_4)$	78

5.1	The samples used to approximate ρ_Λ for the idealized inlet for $Q = (q_1, q_6)$ where $\lambda_{true} = (\lambda_1, \lambda_2) = (0.0781, 0.168)$ using Algorithm 3. Left: The samples $\lambda^{(j)} \in \Lambda$. Right: The corresponding data $Q(\lambda^{(j)}) \in \mathcal{D}$	83
5.2	The approximation of ρ_Λ for the idealized inlet for $Q = (q_1, q_6)$ where $\lambda_{true} = (\lambda_1, \lambda_2) = (0.0781, 0.168)$. Left: The approximation of ρ_Λ using a regular grid of 121^2 samples in Algorithm 1. Right: The approximation of ρ_Λ using the adaptive sampling Algorithm 3.	84
5.3	Mean results for 20 sets of uniform and adaptive samples for the idealized inlet. Top: The approximation of the relative volume of an implicitly defined region of interest $\mu_\Lambda(Q^{-1}(E))/\mu_\Lambda(\Lambda)$ for $Q = (q_1, q_2)$ on the left and (q_1, q_6) on the right respectively where $\lambda_{ref} = (\lambda_1, \lambda_2) = (0.0781, 0.168)$. Bottom: The corresponding error in the approximation of the relative volume for $Q = (q_1, q_2)$ on the left and (q_1, q_6) on the right.	86
A.1	Channel geometry reproduced from [9].	102
B.1	The basic flowchart for the BET and PolyADCIRC packages. The BET package handles every step in Algorithm 1 while using the PolyADCIRC package to efficiently interface to the ADCIRC computational model. Note in this figure <i>loadBalance</i> is a user created interface to PolyADCIRC.	108

Chapter 1

Introduction

1.1 Background and Motivation

In 2005, category 5 Hurricane Katrina caused 1833 fatalities, \$108 billion in damage, and was the costliest United States hurricane [1, 2]. In recent years, other hurricanes have caused significant damage to the U.S. coast, including Hurricane Wilma (2004), Hurricane Rita (2005), Hurricane Ike (2008), Hurricane Gustav (2008), Hurricane Irene (2011), and Hurricane Sandy (2012). The majority of damage and loss of life from a hurricane is caused by storm surge, i.e. flooding or inundation caused by storms as they approach and make landfall. One of the primary goals of the following work is to apply measure-theoretic computational algorithms for inverse sensitivity analysis to a set of coastal applications governed by the shallow water equations (SWEs). We will study these coastal applications using the ADvanced CIRCulation model for oceanic, coastal, and estuarine waters (ADCIRC) which incorporates a spatially varying bottom friction model. The balance between momentum loss from bottom stress due to bottom friction and vegetation, and wind stress due to the hurricane is one of the primary controlling factors of storm surge [3, 4]. The ADCIRC model solves the generalized wave continuity equation and the depth averaged momentum equations on an unstructured finite element mesh

using a finite difference scheme in time [5, 6]. The ADCIRC model depends on many parameter fields, including bottom friction. We will focus on bottom friction due to the sensitivity of the SWEs to bottom friction and the inherent uncertainty in this parameter.

Manning’s formula is currently used to model bottom friction in a variety of coastal applications (e.g., hurricane storm surge, tsunamis, flow over vegetation, etc). However, these applications are beyond the original scope of Manning’s formula [6–8]. Manning’s formula was originally developed to characterize bottom friction for open channel flow [9–11]. Despite this fact, Manning’s formula continues to be a *very useful*, if not entirely correct, model of flow resistance for environmental flows¹ [3, 14]. The Manning’s coefficient varies based on the type of “roughness” it is approximating. This means that a different Manning’s n value is required to represent different bottom coverings such as sand, silt, mud, large stones, small stones; various types of wetlands, forests, vegetation, agricultural lands; and different types of residential, commercial, and industrial developed land. The Coastal Change Analysis Program (C-CAP) Regional Land Cover database (NOAA) and the National Land Cover Database (NLCD, USGS) document the geographical distribution of these different types of land cover through the use of a land cover classification scheme. These data sets consist of pixelated (raster-based) land cover

1

Essentially, all models are wrong, but some are useful, George E.P. Box, page 424 of [12] via page 5 of [13].

classification data sets derived from Landsat imagery and high resolution aerial photography. We use these data sets to determine the spatial distribution of land cover classifications and consider the Manning's n coefficient associated with each land cover classification uncertain [7, 15].

We seek to quantify the uncertainty in Manning's n coefficients by using computed quantities of interest (QoIs) to define a map from the parameter domain to observable data (e.g. maximum water surface elevation at a set of gauge sites). We use the geometric information embedded in this map to compute non-parametric probability measures on the parameter domain using a measure-theoretic approach for formulating and solving stochastic inverse problems for physics-based maps. This measure-theoretic approach has been developed and analyzed in [16–20]. In this approach, the core deterministic inverse problem is well-defined with respect to set-valued inverses [16, 18, 20]. Uncertainty quantification often classifies uncertainty into two categories: aleatoric uncertainty and epistemic uncertainty. Aleatoric or statistical uncertainty is generally considered irreducible because it is the uncertainty due to probabilistic variability. Epistemic or systematic uncertainty is generally considered reducible because incorporating more information of the system reduces this type of uncertainty. Both aleatoric and epistemic uncertainty are quantified within this framework [19]. We employ a non-intrusive sample based algorithm developed in [19] to obtain a non-parametric probability measure on the parameter space. We propose a probability based goal-oriented adaptive sampling algorithm to more efficiently utilize a limited

number of forward model solves in order to approximate the probability of an implicitly defined set of model parameters (Manning’s n coefficients).

1.2 Research Contributions

The completed research covers the three concentration areas of the Computational Science, Engineering, and Mathematics program as follows:

Area A: Applicable mathematics. We have extended the algorithms used to approximate the probability measure on the parameter space to employ goal-oriented adaptive sampling techniques. This is key to combating the “curse of dimensionality” with regard to sampling high dimensional parameter spaces. There are two sources of error in approximating the probability measure: (1) the discretization of the probability measures themselves, and (2) error in the numerical computation of the forward model [19]. We focus on reducing errors of the first type through adaptively sampling the parameter space. We provide theoretical justification for the convergence of the goal-oriented adaptive sampling algorithm. We show numerical results regarding the convergence of a probabilistic goal-oriented sampling algorithm.

Area B: Numerical analysis and scientific computation. The current computational measure-theoretic algorithm is non-intrusive [18, 20]. This allows us to treat ADCIRC as a black box model. We have developed PolyADCIRC, an open-source Python package, to simultaneously evaluate P(arallel) ADCIRC for a given set of samples in the parameter space [21]. We

have also developed **BET**, as part of the **BET** development team with Steve Mattis, Troy Butler, and Scott Walsh, an open-source Python package for solving measure-theoretic stochastic inverse problems [22]. **BET** provides both serial and parallel implementations of the various algorithms discussed herein, examples, and visualization routines [22].

Given that the evaluation of the forward model is currently the most computationally intensive task, we have structured the adaptive implementation to group model evaluations to facilitate load balancing and parallel evaluation. To decrease the cost of model evaluations for more complex physical domains and forcing conditions we incorporate an existing subdomain implementation of **ADCIRC** [23–25]. Each different model evaluation requires us to map bottom friction parameter values to the finite element (FE) mesh through a node centered spatial averaging procedure utilizing the pixelated land cover classification data. We have moved the majority of this process off-line by decomposing this procedure into a set of linear operations. We leverage existing software (**GridData** [26]) in the creation of a set of linear maps from pixelated land-classification data to the FE mesh used by **ADCIRC**. The remaining on-line computation to map bottom friction parameter values to the FE mesh is a single dot product per model evaluation and a matrix product for a group of model evaluations. **PolyADCIRC** includes sub-packages that automate and parallelize the above processes [21].

Area C: Mathematical modeling and application. We have applied this approach in the case of an idealized inlet domain for two and three

dimensional parameter fields. We expanded this approach to study parameter estimation for bottom friction for coastal inundation using Hurricane Gustav as a test bed. Inundation of coastal areas only occurs with hurricanes and other catastrophic events. We employ a subdomain implementation of ADCIRC [23–25] to reduce simulation time and allow us to focus on specific subdomains of particular interest rather than the much larger physical domain necessary for hurricane simulations. Subdomains of interest can feature as few as four dominant land classifications whereas the full domain can feature as many as twenty-three different land classifications [7, 15].

For both the idealized inlet and hurricane case studies we have shown that choosing gauge sites that provide geometrically distinct quantities of interest *and* are nearly perpendicular in a non-linear sense (have small skewness) has a marked effect on the parameter estimation results. We demonstrate the effect the choice of gauge sites has on the solution to the inverse problem and prediction using that solution. It is especially important to identify QoI that result in a well-conditioned inverse as the number of geometrically distinct QoI is at most the dimension of the parameter space [18, 19]. Since there is no adjoint currently available for ADCIRC we approximate gradient information using finite differences (central, forward, and radial basis function). We have used gradient information to optimally choose gauge sites for the Hurricane Gustav case study [22, 27]. We have focused primarily on estimating the bottom friction parameter, Manning’s n . We have developed this parameter estimation framework in order to obtain estimates of parameters and their

associated probability densities for use in ensemble hurricane forecasts.

1.3 Outline

The outline of this dissertation is as follows. In Chapter 2, we give a brief overview of the the ADCIRC model. We summarize the methodology for modeling flow resistance with Manning’s n in ADCIRC². In Chapter 3, we summarize the measure-theoretic framework used to formulate and solve the stochastic inverse problem. We summarize sources of approximation error within this framework. In Chapter 4, we give a detailed description of the stochastic inverse problem for ADCIRC and develop the mesoscale representation of Manning’s n coefficient for a finite element mesh. We also describe the integration of the measure-theoretic algorithm, the ADCIRC model, and the mesoscale representation of Manning’s n . We review numerical results for an example with uncertain Manning’s n coefficients for an idealized inlet where the flow is partially obstructed by an earthen jetty. We examine both two-dimensional and three-dimensional parameter spaces. We also review numerical results for a case study involving Hurricane Gustav. Chapter 5 provides a probabilistic goal-oriented adaptive sampling algorithm to adaptively address error in numerical set approximation. Finally, in Chapter 6 we provide concluding remarks and opportunities for future work.

²We include an in-depth review of the derivation of Manning’s n for shallow water environments in Appendix A.

Chapter 2

The Advanced Circulation Model for Oceanic, Coastal, and Estuarine Waters (ADCIRC)

We will study hurricane storm surge using the ADvanced CIRCulation model for oceanic, coastal and estuarine waters (ADCIRC). ADCIRC is a prominent finite element model that solves the generalized wave continuity equation (GWCE) and the shallow water equations (SWEs) for momentum on an unstructured mesh with a finite difference temporal discretization [6]. The ADCIRC model has been extensively verified and validated using hindcasts of several hurricanes including Hurricane Ike, Katrina, and Gustav [7, 28–31]. The ADCIRC model also allows for the specification of nodal model parameters including Manning’s n . Hence, it provides an appropriate test bed to study the estimation of bottom friction in coastal areas. We summarize the governing equations pertinent to the formulation and implementation of ADCIRC. For a more detailed discussion we direct the reader to [6]. This is followed by a description of the frictional flow resistance model used by ADCIRC in Section 2.2. Note portions of this chapter were originally published in [32].

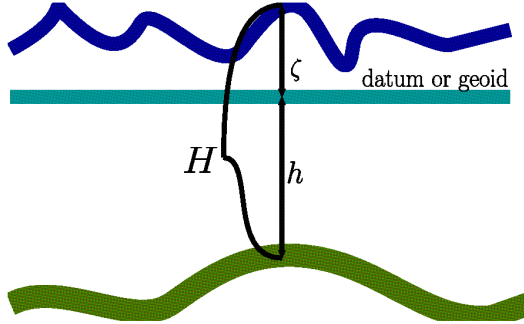


Figure 2.1: An illustration of the the total water column height $H = h + \zeta$ where h is the bathymetric depth, and ζ is the free surface above the geoid or datum.

2.1 Modeling the Shallow Water Equations in ADCIRC

The shallow water equations (SWEs) are derived by vertically integrating the incompressible Navier-Stokes equations with a hydrostatic pressure [6]. The derivation of the SWEs closely parallels the derivation of the equations governing open channel flow for which Manning’s formula was originally derived. See Appendix A for a summary of the derivation of Manning’s formula. The continuity equation is

$$\frac{\partial H}{\partial t} + \frac{\partial Q_x}{\partial x} + \frac{\partial Q_y}{\partial y} = 0 \quad (2.1.1)$$

where $Q_x = UH$, $Q_y = VH$ are the x, y -directed flux per unit width, U, V are the depth-averaged velocities, $H = h + \zeta$ is the total water column height, h is the bathymetric depth, and ζ is the free surface above the geoid as show in Figure 2.1 [6]. The accompanying momentum equations in conservative form

are

$$\begin{aligned}
\frac{\partial Q_x}{\partial t} + \frac{\partial U Q_x}{\partial x} + \frac{\partial V Q_x}{\partial y} - f Q_y &= -gH \frac{\partial[\zeta + (P_s/g\rho_0) - \alpha\eta]}{\partial x} \\
&\quad + \frac{\tau_{sx} - \tau_{bx}}{\rho_0} + M_x - D_x - B_x \\
\frac{\partial Q_y}{\partial t} + \frac{\partial U Q_y}{\partial y} + \frac{\partial V Q_y}{\partial x} + f Q_x &= -gH \frac{\partial[\zeta + (P_s/g\rho_0) - \alpha\eta]}{\partial y} \\
&\quad + \frac{\tau_{sy} - \tau_{by}}{\rho_0} + M_y - D_y - B_y
\end{aligned} \tag{2.1.2}$$

where g is gravity, f is the Coriolis parameter, P_s is the atmospheric pressure at the sea surface, ρ_0 is the reference density of water, and η is the Newtonian equilibrium tidal potential. The terms $\tau_{b(\cdot)}$ are the bottom stresses, $\tau_{s(\cdot)}$ are the imposed surface stresses, $M_{(\cdot)}$ are the vertically-integrated lateral stress gradients, $D_{(\cdot)}$ are momentum dispersion terms, and $B_{(\cdot)}$ are the vertically-integrated baroclinic pressure gradients [6]. The bottom stress terms are defined using a quadratic or linear drag law and the Manning's n formula as described in Section 2.2.

ADCIRC replaces the continuity equation, Equation (2.1.1), with the Generalized Wave Continuity Equation (GWCE) by using a second order hyperbolic formulation of the continuity relation in Eq. (2.1.1) [6]. The GWCE is a more computationally tractable version of the continuity equation, as this formulation removes spurious oscillations that are associated with the primitive Galerkin finite element solution of the SWEs [6]. The GWCE is formulated by taking the time derivative ($\partial/\partial t$) of Eq. (2.1.1) and then adding the result to Eq. (2.1.1) multiplied by a parameter $\tau_0 \geq 0$. We also assume that bathymetric depth is constant with respect to time (i.e., $\partial H/\partial t = \partial \zeta/\partial t$) [6]. Next we

use the weighted residual method, and integrate by parts, and finally substitute the vertically-integrated momentum equations (2.1.2) into this modified continuity equation (2.1.1) [6]. For a detailed derivation of the GWCE we direct the reader to [6].

2.2 Modeling Flow Resistance in ADCIRC

Manning's coefficient or Manning's n encapsulates the momentum loss due to bottom friction represented in the Gauckler-Manning-Strickler formula (Equation (2.2.7)) which relates average cross-sectional velocity, hydraulic radius, and the channel bed slope [9–11,33,34]. The Gauckler-Manning-Strickler formula was originally developed for open-channel flow in a fully-turbulent fairly regular unvegetated domain [9–11,33–35]. For open-channel flow that meets these assumptions Manning's coefficient may be determined empirically from field or laboratory measurements or from a sampling of the diameters of roughness elements [36–39]. Arcement and Schneider [40], along with Chow [41], and Barnes [37] have provided guides for selecting Manning's coefficient that extend the original domain of application to flood plains, vegetated water ways, and channels with irregular boundaries. These guides consist of tables [41], photographic guides [37], and a combination thereof [40]. However, even with their use the selection of Manning's coefficient remains difficult for inexperienced users.

Furthermore, Manning's formula although extremely useful is not the correct model of momentum loss due to vegetation in natural waterways. Man-

ning’s formula models bottom friction, not the more complex form drag due to flexible vegetation [42–44]. Complex hydrological models require some representation of momentum loss due to a combination of bottom friction, vegetation, bed-forms, and the porous media-like structures that occur in coastal estuaries [28,31,45]. Often these sub-gridscale processes require some upscaled drag model. We use the Gauckler-Manning-Strickler formulation to parameterize the spatially varying friction field due to its prevalence in civil engineering. Unfortunately, it is extremely cost prohibitive to use field measurements to estimate Manning’s n for these conditions over a large physical domain, especially as this representation would be subject to seasonal and temporal variation. We aspire to leverage the land cover and classification data collected by the NCLD and C-CAP projects to estimate Manning’s coefficient fields for these types of computational modeling problems [43,46–48]. Other methods of estimating Manning’s coefficient using Bayesian parameter estimation techniques [49,50], Kalman filtering [51], and adjoint based techniques [52] focus on determining a single parameter or single vector of parameters. However, the solution to the parameter estimation problem is inherently set-valued when the dimension of the parameter space $\Lambda \subset \mathbb{R}^n$ is greater than (or sometimes equal to) the dimension of the data space $\mathcal{D} \subset \mathbb{R}^d$. The measure-theoretic parameter estimation methodology fully acknowledges this set-valued nature and instead seeks to determine the set of vectors of Manning’s coefficients that is of highest probability rather than a single value.

Flow resistance is modeled in ADCIRC with a quadratic or linear drag

coefficient and Manning’s formula. The two dimensional, depth-integrated version of ADCIRC utilizes a generalized slip formulation for the bottom stress term:

$$\frac{\tau_{bx}}{\rho_0} = \frac{K_{slip}Q_x}{H} = K_{slip}U, \quad \frac{\tau_{by}}{\rho_0} = \frac{K_{slip}Q_y}{H} = K_{slip}V \quad (2.2.1)$$

where

$$K_{slip} = C_d\sqrt{U^2 + V^2}. \quad (2.2.2)$$

In the “ADCIRC User Manual” [5, 6] the drag coefficient, C_d , used for the bottom friction is defined

$$C_d(t, x, y) = \frac{gn(x, y)^2}{(h(x, y) + \zeta(t, x, y))^{1/3}} = \frac{gn(x, y)^2}{H(t, x, y)^{1/3}} \quad (2.2.3)$$

where n is the Manning’s n value. The generalized slip formulation can be rearranged

$$\frac{\tau_{bx}^2 + \tau_{by}^2}{\rho_0^2} = K_{slip}^2(U^2 + V^2) \quad (2.2.4)$$

$$\frac{|\boldsymbol{\tau}_b|^2}{\rho_0^2(U^2 + V^2)} = K_{slip}^2 = C_d^2(U^2 + V^2) \quad (2.2.5)$$

$$\frac{|\boldsymbol{\tau}_b|}{\rho_0|\mathbf{U}|^2} = C_d. \quad (2.2.6)$$

The same scalings used by Gioia and Bombardelli may be applied so that $|\boldsymbol{\tau}_b| \sim RgS$ [9]. Then we substitute in Manning’s formula in Equation (2.2.7)

$$|\mathbf{U}| = \frac{1}{n}S^{1/2}R^{2/3} \quad (2.2.7)$$

[9, 11, 33] (for metric units) to obtain

$$\begin{aligned}
 C_d &= \frac{|\boldsymbol{\tau}_b|}{\rho_0 |\mathbf{U}|^2} \sim \frac{\rho_0 R g S}{\rho_0 |\mathbf{U}|^2} = \frac{R g S}{|\mathbf{U}|^2} = \frac{R g S}{\left(\frac{1}{n} S^{1/2} R^{2/3}\right)^2} \\
 &= \frac{R g S}{\frac{1}{n^2} S R^{4/3}} = \frac{n^2 g R}{R^{4/3}} = \frac{n^2 g}{R^{1/3}}.
 \end{aligned} \tag{2.2.8}$$

In this case the hydraulic radius is equal to the total water column height, $R = H(t, x, y)$ so

$$C_d(t, x, y) \approx \frac{n(x, y)^2 g}{R(t, x, y)^{1/3}} = \frac{gn(x, y)^2}{H(t, x, y)^{1/3}}. \tag{2.2.9}$$

Resistance is modeled using a linear slip condition in shallow regions near wet/dry boundaries where H approaches zero to prevent an erroneous C_d [6]. For a more thorough discussion of the Manning's formula and its derivation see Appendix A.

The Manning's n coefficient is a highly variable spatial parameter often defined on a sub-grid scale, e.g., using land classification data defined pixel-by-pixel from high resolution imagery (e.g., see Figure 2.2). The Manning's n values themselves are often assigned from tables based on empirical estimates of common land classifications found in the hydraulic literature [7](e.g., see Table 2.1). For the purpose of numerical evaluation of the ADCIRC model, the Manning's n coefficient is specified at nodes for a given discretization of a physical domain and a continuous, piecewise-linear representation of bottom friction is then constructed. Data is often collected on a sub-grid scale so an upscaling procedure (e.g., local spatial averaging) is used to define the values at the nodes [15]. This procedure, described in Chapter 4, defines a specific

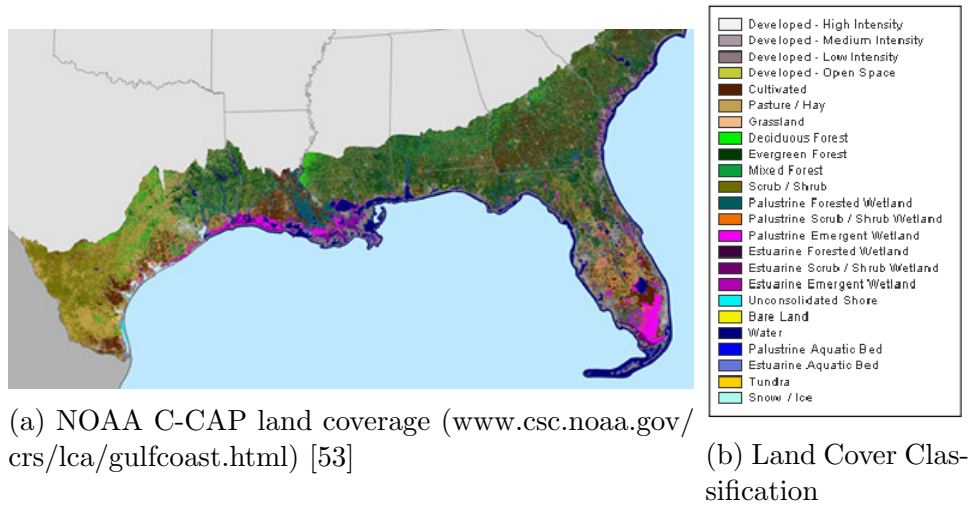


Figure 2.2: High resolution land cover classification data.

Class	Description	Min	Max
23	Water	0.015	0.030
4	Saline Marsh	0.020	0.065
3	Brackish Marsh	0.020	0.070
2	Intermediate Marsh	0.025	0.080
1	Fresh Marsh	0.030	0.085
5	Wetland Forrest	0.080	0.160

Table 2.1: Example ranges of values of LA-GAP Manning’s n coefficients [15].

mesoscale representation of the Manning’s n coefficient parameterized by the land cover classification in the physical domain.

Chapter 3

A Measure-Theoretic Framework for Stochastic Inverse Problems

We formulate and solve the stochastic inverse problem using a measure-theoretic framework. In Chapter 4, we apply this framework to quantify uncertainty in Manning's n coefficient. This measure-theoretic approach utilizes all of the geometric information inherent in the QoI map, $Q : \Lambda \rightarrow \mathcal{D}$, between the parameter space and data space. Below we summarize the framework and formulation of the stochastic inverse problem from *A Measure-Theoretic Computational Method for Inverse Sensitivity Problems III: Multiple Quantities of Interest* [17] and *Solving Stochastic Inverse Problems using Sigma-Algebras on Contour Maps* [19] by Butler, et. al. We refer the interested reader to [16–20] for an in-depth theoretical description of the formulation, framework, theorems on existence and uniqueness, algorithmic implementation, and error analysis. The computational algorithms in this section are available as a fully documented Python package at [22].

3.1 Formulating the Stochastic Inverse Problem

Let $M(Y, \lambda)$ denote a physics based model with solutions $Y = Y(\lambda)$ where $\lambda \in \Lambda \subset \mathbb{R}^n$ denote the parameter domain for the model. For example, $M(Y, \lambda)$ could be ADCIRC, Y could be the water column height, and λ could be the Manning's n coefficients associated with a set of land classification types [32]. Let $Q : \Lambda \rightarrow \mathcal{D}$ denote the vector-valued QoI map where $\mathcal{D} \subset \mathbb{R}^d$ denotes the data domain. We assume the dimension of the data space d is less than or equal to the dimension of the parameter space n , $d \leq n$. This represents this situation where we have fewer observations than parameters so that we have an under-constrained rather than an over-constrained inverse problem. The components of the vector valued QoI map are defined by functionals of the solutions to the model so that $Q(\lambda) = (q_1(\lambda), \dots, q_d(\lambda))$ where $q_i(\lambda) := q_i(Y(\lambda))$. For example, the maximum water elevations at some set of points in the physical domain. We also assume that Λ is imbued with a metric that is specified as a part of the model. This yields the measure space $(\Lambda, \mathcal{B}_\Lambda, \mu_\Lambda)$ where \mathcal{B}_Λ is a Borel σ -algebra on Λ and μ_Λ is the volume measure induced by the metric on Λ .

We say that the components of Q are *geometrically distinct* if Q is locally differentiable a.e. and the Jacobian of Q has full-rank a.e. in Λ . Assuming Q is geometrically distinct μ_Λ induces a push forward measure $\mu_{\mathcal{D}}$ on \mathcal{D} , yielding the measure space $(\mathcal{D}, \mathcal{B}_{\mathcal{D}}, \mu_{\mathcal{D}})$ where $\mathcal{B}_{\mathcal{D}}$ is the Borel σ -algebra on \mathcal{D} and for all measurable $A \in \mathcal{B}_{\mathcal{D}}$, $\mu_{\mathcal{D}}(A) = \mu_\Lambda(Q^{-1}(A))$. We consider the evaluation of the map Q as the forward problem. The evaluation of $\mu_{\mathcal{D}}(A)$ for

$A \in \mathcal{B}_{\mathcal{D}}$ is the forward sensitivity analysis problem. For the forward stochastic problem, we assume a probability measure P_{Λ} is given on Λ that is absolutely continuous with respect to μ_{Λ} . This yields the probability space $(\Lambda, \mathcal{B}_{\Lambda}, P_{\Lambda})$ and the associated probability density function ρ_{Λ} (i.e. the Radon-Nikodym derivative of P_{Λ} with respect to μ_{Λ}). The forward stochastic problem involves the measurement of arbitrary events $E \in \mathcal{B}_{\mathcal{D}}$,

$$P_{\mathcal{D}}(E) = \int_E \rho_{\mathcal{D}} d\mu_{\mathcal{D}} = \int_{Q^{-1}(E)} \rho_{\Lambda} d\mu_{\Lambda} = P_{\Lambda}(Q^{-1}(E)), \quad (3.1.1)$$

i.e. the computation of $P_{\mathcal{D}}(E)$ given $(\Lambda, \mathcal{B}_{\Lambda}, P_{\Lambda})$ and $Q : \Lambda \rightarrow \mathcal{D}$. The stochastic inverse problem is the direct inverse: given $(\mathcal{D}, \mathcal{B}_{\mathcal{D}}, P_{\mathcal{D}})$ and $Q : \Lambda \rightarrow \mathcal{D}$, determine the probability of arbitrary events $A \in \mathcal{B}_{\Lambda}$. The solution of the stochastic inverse problem relies on the mapping between various sets in $\mathcal{B}_{\mathcal{D}}$ and \mathcal{B}_{Λ} .

Ideally, we desire the mapping $Q : \Lambda \rightarrow \mathcal{D}$ to be a bijection so that the deterministic inverse problem is well-posed in the sense that $Q^{-1}(Q(\lambda)) = \{\lambda\}$. Unfortunately, most inverse problems of interest are ill-posed in the sense that $Q^{-1}(Q(\lambda))$ is a set of values in Λ . Indeed, the most interesting case mathematically and most common in practice has $d < n$ implying Q *cannot* be 1 – 1. In this case the inverse map Q^{-1} is inherently set-valued in Λ see Figure 3.1.

We call the set-valued inverse of the map Q for any fixed point $q \in \mathcal{D}$ a *generalized contour*. Assuming Q is piecewise-smooth, Implicit Function Theorem guarantees the existence of these generalized contours as locally smooth

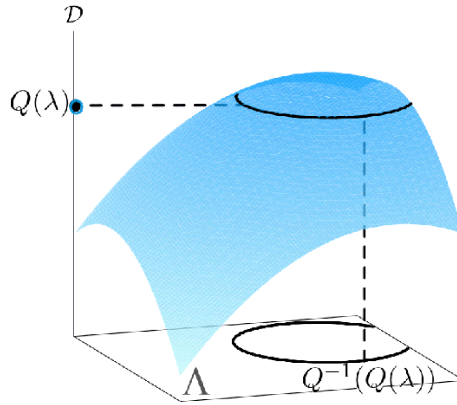


Figure 3.1: The response surface for a map $Q : \Lambda \rightarrow \mathcal{D}$ between a 2-dimensional parameter space and a 1-dimensional data space. The inverse image of $Q(\lambda)$ the contour $Q^{-1}(Q(\lambda))$. This illustrates an inherently set-valued inverse map Q^{-1} . This graphic has been reproduced with permission from Drs. Butler and Estep.

$(n - d)$ -dimensional manifolds. The map Q^{-1} defines an equivalence class relation on Λ . We denote the space of equivalence classes imposed by Q^{-1} as $(\mathcal{L}, \mathcal{B}_{\mathcal{L}}, \mu_{\mathcal{L}})$ where $\mathcal{B}_{\mathcal{L}}$ is the σ -algebra generated by the inverse images of the generating sets of $\mathcal{B}_{\mathcal{D}}$ and the measure $\mu_{\mathcal{L}}$ is induced by $\mu_{\mathcal{D}}$. Each point in \mathcal{L} can be identified with a generalized contour, so the map Q defines a bijection between \mathcal{L} and \mathcal{D} . Consequently, this is a bijection between points in \mathcal{D} (assuming that \mathcal{D} is the proper range of the map Q over domain Λ) and generalized contours in Λ . We can identify each member of \mathcal{L} with a (possibly piecewise defined) d -dimensional manifold in Λ that indexes the generalized contours which we call a *transverse parameterization* see Figure 3.2. Note that the union of all generalized contours contains every point in Λ , but we cannot distinguish between two individual points in the same equivalence class

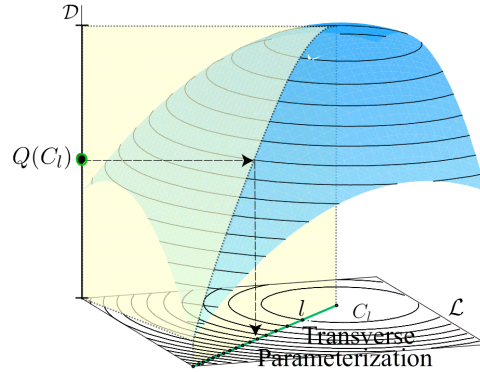


Figure 3.2: The response surface for a map $Q : \Lambda \rightarrow \mathcal{D}$ between a 2-dimensional parameter space and a 1-dimensional data space. We can use a *transverse parameterization* to identify each member $l \in \mathcal{L}$ of the set of equivalence classes \mathcal{L} with a particular contour C_l . This graphic has been reproduced with permission from Drs. Butler and Estep.

(generalized contour). At this point we have exploited all of the geometric information in Q^{-1} . We can not distinguish between or measure sets contained within an individual generalized contour hence we can only measure probabilities of contour events rather than arbitrary events in \mathcal{B}_Λ . In order to compute a probability measure on $(\Lambda, \mathcal{B}_\Lambda)$, we require measures along the generalized contours. Below we summarize the proof from that the desired σ -algebras exist and that the stochastic inverse problem is well-posed under the adoption of an ansatz.

3.2 Solving the Inverse Problem using Sigma-Algebras on Contour Maps (SACOM)

Any σ -algebra on the parameter space can be rewritten as a product of σ -algebras *along* each generalized contour and *across* each generalized contour. If the map Q is linear, the $(n - d)$ -dimensional generalized contours and d -dimensional transverse parameterization are hyperplanes, and the Borel σ -algebra on the product space Λ is simply $\mathcal{B}_\Lambda = \mathcal{B}_\mathcal{L} \otimes \mathcal{B}_{C_l}$ where $C_l := \pi^{-1}(l)$, for arbitrary $l \in \mathcal{L}$ and $\pi_l(\lambda)$ is the projection map from Λ to \mathcal{L} , see Figure 3.2. The contour σ -algebra $\mathcal{C}_\Lambda \subset \mathcal{B}_\Lambda$ can be identified by $\mathcal{B}_\mathcal{L}$ and $\mathcal{C}_\Lambda = \mathcal{B}_\mathcal{L} \otimes \mathcal{T}_{C_l}$ where \mathcal{T}_{C_l} is the trivial σ -algebra on C_l . In this linear case, the solution to the stochastic inverse problem reduces to a form similar to the standard Fubini Theorem over sets in Λ using a simple change of coordinates with respect to the hyperplanes defining the generalized contours and transverse parameterization. The transverse product σ -algebras $\mathcal{C}_\Lambda = \otimes_{\mathcal{B}_\mathcal{L}} \{\mathcal{T}_{C_l}\}$ and $\mathcal{B}_\Lambda = \otimes_{\mathcal{B}_\mathcal{L}} \{\mathcal{B}_{C_l}\}$ are used in the more general case of nonlinear Q and solutions to the stochastic inverse problem are defined in terms of iterated integrals. The disintegration theorems and the incorporation of an ansatz give us the means to determine the conditional probability measures *along* generalized contours and the marginal probability *across* generalized contours, which defines the unique solution to the stochastic inverse problem [18, 19, 32]

3.2.1 Existence and Uniqueness

We complete the summary of the proof for existence and uniqueness for the stochastic inverse problem on $(\Lambda, \mathcal{C}_\Lambda)$ and $(\Lambda, \mathcal{B}_\Lambda)$ by applying two forms of the Disintegration Theorem.

Theorem 3.2.1. (*Disintegration of Contour Map Probabilities*). *Assume that P_Λ is a probability measure on $(\Lambda, \mathcal{C}_\Lambda)$. There exists a family of conditional probability measures $\{P_l\}$ on $\{(C_l, \mathcal{T}_\Lambda)\}$ giving the disintegration:*

$$P_\Lambda(A) = \int_{\pi_{\mathcal{L}}(A)} \left(\int_{\pi_{\mathcal{L}}^{-1}(l) \cap A} dP_l(\lambda) \right) dP_{\mathcal{L}}(l), \quad \forall A \in \mathcal{C}_\Lambda. \quad (3.2.1)$$

This family of conditional probability measures are $\{P_l\}$ such that

$$P_l(A) = \begin{cases} 1 & \text{if } \pi^{-1}(l) \subset A \in \mathcal{C}_\Lambda \\ 0 & \text{otherwise} \end{cases} \quad (3.2.2)$$

. The marginal probability, $P_{\mathcal{L}}$, across generalized contours is completely determined by the the quantity of interest map Q and $P_{\mathcal{D}}$ as depicted in Figure 3.3. This is the unique solution on $(\Lambda, \mathcal{C}_\Lambda)$. However, we desire a unique solution on $(\Lambda, \mathcal{B}_\Lambda)$. We can apply a second form of the Disintegration Theorem to show the existence of a unique solution of $(\Lambda, \mathcal{B}_\Lambda)$.

Theorem 3.2.2. (*Disintegration Theorem*). *Assume that P_Λ is a probability measure on $(\Lambda, \mathcal{B}_\Lambda)$. There exists a family of conditional probability measures $\{P_l\}$ on $\{(C_l, \mathcal{B}_\Lambda)\}$ giving the disintegration:*

$$P_\Lambda(A) = \int_{\pi_{\mathcal{L}}(A)} \left(\int_{\pi_{\mathcal{L}}^{-1}(l) \cap A} dP_l(\lambda) \right) dP_{\mathcal{L}}(l), \quad \forall A \in \mathcal{B}_\Lambda. \quad (3.2.3)$$

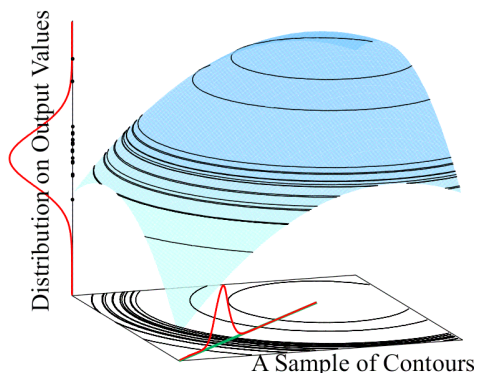


Figure 3.3: The response surface for a map $Q : \Lambda \rightarrow \mathcal{D}$ between a 2-dimensional parameter space and a 1-dimensional data space. The distribution on output values $\rho_{\mathcal{D}}$ and the corresponding marginal probability across the generalized contours. This graphic has been reproduced with permission from Drs. Butler and Estep.

To show uniqueness we must extend the P_l from Theorem 3.2.1. However, we do not have enough information to determine conditional probability measures on $\{(C_l, \mathcal{B}_{C_l})\}$ from the map $Q : \Lambda \rightarrow \mathcal{D}$. We must assume a family of probability measures are given or adopt an ansatz. We adopt the “non-preferential” Standard Choice for Ansatz illustrated in Figure 3.4 where we set the family of probability measures along the generalized contours to be uniform with respect to the volume(length) of the generalized contours, $P_l(A) = \mu_{C_l}(A)/\mu_{C_l}(C_l)$, $\forall l \in \mathcal{L}$, $A \in \Lambda$ which is based on the Disintegration of Volume Measure. See [19] for the Disintegration of Volume Measure Theorem. Note that the Standard Choice of Ansatz is valid for $\mu_{\Lambda}(\Lambda) < \infty$ which is easily satisfied if Λ is compact (or pre-compact). In the many engineering and scientific applications Λ is bounded and finite dimensional and thus pre-compact.

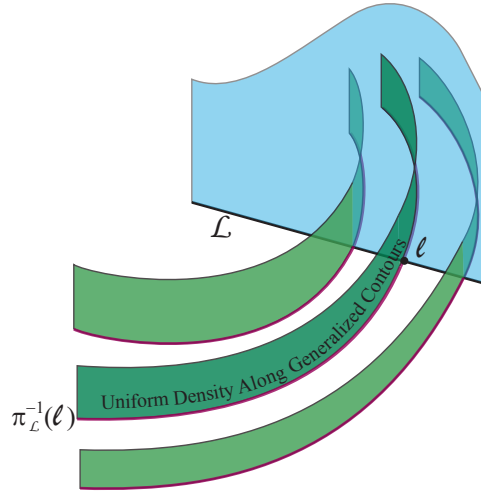


Figure 3.4: Illustration of the Standard Choice for Ansatz where \mathcal{L} is the space of equivalence classes, $l \in \mathcal{L}$ is an index of \mathcal{L} , and $\pi_{\mathcal{L}}^{-1}(l)$ is a particular generalized contour in Λ . This graphic has been reproduced with permission from Drs. Butler and Estep.

3.2.2 Approximation

We describe the basic algorithm for the approximation of P_{Λ} and briefly outline issues in the practical computation of P_{Λ} . It was shown through repeated application of the Lebesgue Dominated Convergence Theorem that

Theorem 3.2.3. *Given probability measure $P_{\mathcal{D}}$, absolutely continuous with respect to $\mu_{\mathcal{D}}$, on $(\mathcal{D}, \mathcal{B}_{\mathcal{D}})$ with density $\rho_{\mathcal{D}}$ and event $A \in \mathcal{B}_{\Lambda}$, there exists a sequence of approximations $P_{\Lambda, N}(A)$ using simple function approximations to probability densities $\rho_{\Lambda, N}$ and $\rho_{\mathcal{D}, M}$ requiring only calculations of volumes in Λ that converges to $P_{\Lambda}(A)$ as $N, M \rightarrow \infty$.*

Within the for-loop of Algorithm 1 we set the probability $P_{\Lambda, N}(\mathcal{V}_j)$ of a particular Voronoi cell $\mathcal{V}_j \subset \Lambda$ to be the probability of $I_i : Q_j \in I_i \subset \mathcal{D}$ which

Algorithm 1: A Sampled Based Approximation of the Inverse Density [19, 54]

Choose samples $\{\lambda^{(j)}\}_{j=1}^N$ defining the partition $\{\mathcal{V}_j\}_{j=1}^N \subset \Lambda$ of Λ .

Assign values $Q_j = Q(\lambda^{(j)})$ for the points $\lambda^{(j)}$, $j = 1, \dots, N$.

Choose a discretization partition of \mathcal{D} , $\{I_i\}_{i=1}^M$.

Form the simple function approximation

$$\rho_{\mathcal{D},M}(q) = \sum_{i=1}^M P_{\mathcal{D},i} \mathbf{1}_{I_i}(q), \quad q \in \mathcal{D}$$

where

$$\mathbf{1}_{I_i}(q) = \begin{cases} 1 & \text{if } q \in I_i \\ 0 & \text{otherwise} \end{cases} \quad (3.2.4)$$

and $P_{\mathcal{D},i} \approx P_{\mathcal{D}}(I_i) = \int_{I_i} \rho_{\mathcal{D}} d\mu_{\mathcal{D}}$, $i = 1, \dots, M$.

Let $C_i = \{j : Q_j \in I_i\}$, $i = 1, \dots, M$.

Let $O_j = \{i : Q_j \in I_i\}$, $j = 1, \dots, N$.

Let $V_j \approx \mu_{\Lambda}(\mathcal{V}_j)$, $j = 1, \dots, N$.

for $j = 1, \dots, N$ **do**

 | Set $P_{\Lambda,N}(\mathcal{V}_j) = (V_j / \sum_{k \in C_{O_j}} V_k) P_{\mathcal{D},O_j}$

end

is $P_{\mathcal{D},O_j}$ normalized $(V_j / \sum_{k \in C_{O_j}} V_k)$ which is the volume of the particular Voronoi cell V_j divided by the volume of all the Voronoi cells $\{V_k : k \in C_{O_j}\}$ that map to the same set in the data space $I_i \subset \mathcal{D}$.

We use Algorithm 1 to form the simple function approximation

$$\rho_{\Lambda,N}(\lambda) = \sum_{j=1}^N \frac{P_{\Lambda,N}(\mathcal{V}_j)}{\mu_{\Lambda}(\mathcal{V}_j)} \mathbf{1}_{\Lambda}(\lambda) \quad (3.2.5)$$

[19, 54]. There are various strategies we can use to choose the samples $\{\lambda^{(j)}\}_{j=1}^N$ based on the desired goal. We will address these strategies in Chapter 5. The samples $\{\lambda^{(j)}\}_{j=1}^N$ implicitly define a Voronoi tessellation $\{\mathcal{V}_j\}_{j=1}^N \subset \Lambda$ such that $\mathcal{V}_j := \{\lambda \in \Lambda : d_v(\lambda^{(i)}, \lambda) \leq d_v(\lambda^{(j)}, \lambda), \forall j = 1, \dots, N\}$

where $d_v(\cdot, \cdot)$ is a specified metric on Λ [19, 54]. We can then approximate $P_\Lambda(A)$ for any arbitrary event $A \in \mathcal{B}_\Lambda$ in the usual way with inner and outer sums of $P_{\Lambda, N}$ or by direct integration of $\rho_{\Lambda, N}$ [16, 18–20]. If we are interested in events, $A \in \mathcal{B}_\Lambda$, that are larger than the Voronoi cells, $\{\mathcal{V}_j\}$, we can estimate $P_\Lambda(A)$ using the counting measure $\tilde{P}_{\Lambda, N}$ defined by

$$\tilde{P}_{\Lambda, N}(A) := \sum_{j=1}^N P_{\Lambda, N}(\mathcal{V}_j) \mathbf{1}_{\lambda^{(j)}}(A). \quad (3.2.6)$$

Note that $\tilde{P}_{\Lambda, N}$ can be calculated as the summation of the probabilities of the Voronoi cells associated with samples binned to a particular event [32].

3.2.3 Error

The fundamental sources of error in approximating any measure (e.g. probability or volume measures) is the approximation of sets in various σ -algebras (i.e. \mathcal{B}_Λ , $\mathcal{B}_\mathcal{D}$, and \mathcal{C}_Λ). The numerical approximation issues are approximating $P_\mathcal{D}$ on partitions of \mathcal{D} , P_Λ on partitions of Λ , and ameliorating discretization error in the evaluation of the QoI map from the numerical model. The first type of error results from the approximation of volumes of sets in \mathcal{D} and Λ and is essentially sampling error. The second type of error is due to numerical error in the evaluation of the QoI map and results in the possible misidentification of volumes of contour events. We will discuss strategies to reduce error of the first type in Chapter 5. For an in depth discussion and a priori and a posteriori analysis of the errors of the first type we refer the interested reader to [54] and for second type we refer the interested reader to [19].

In essence we are approximating the integral $\int_A \rho_{\mathcal{D}} d\mu_{\mathcal{D}}$ by a weighted sum [54]. In the simplest case we assume the samples $\{\lambda^{(j)}\}_{j=1}^N$ are independently and identically distributed (i.i.d.) uniformly with respect to the volume measure μ_{Λ} . If we choose to approximate the volumes $\mu_{\Lambda}(\mathcal{V}_j) \approx \mu_{\Lambda}(\Lambda)/N$ then the approximation corresponds to a standard Monte Carlo scheme or

$$\int_A \rho_{\mathcal{D}} d\mu_{\mathcal{D}} \approx \sum_{i=1}^N \rho_{\Lambda}(\lambda^{(j)}) \mu_{\Lambda}(\mathcal{V}_j \cap A) \approx (1/N) \sum_{i=1}^N \rho_{\Lambda}(\lambda^{(j)}) \mathbf{1}_{\lambda^{(j)}}(A) \quad (3.2.7)$$

[54]. Under this interpretation all Voronoi cells are assumed to have the same volume or from a statistical point of view the *expected* volume of *any particular* Voronoi cell is the same [54]. This approximation should only be used for a sufficiently large set of uniform i.i.d. samples. Often we are restricted to a small N due to the cost of solving the map Q . Furthermore, we may choose $\{\lambda^{(j)}\}_{j=1}^N$ samples in a non-uniform manner due to non-linearities in Q or to approximate a particular set A , see Chapter 5. In the majority of cases the Voronoi cells are not explicitly constructed. Instead we use nearest neighbor or (approximate nearest neighbor) searches to appropriately bin samples to events and approximate volumes though volume emulation in Algorithm 2 to reduce the error from the use of a limited set of fixed samples. Note Algorithm 2 can also be used to approximate $\mu_{\Lambda}(\mathcal{V}_j \cap A)$.

3.2.4 Characterizing the Condition of the Inverse Problem

This section is summarized from previously published material in *Definition and solution of a stochastic inverse problem for the Manning's n parameter field in hydrodynamic models* by Butler et. al. [32]. The accuracy of

Algorithm 2: Volume emulation of Voronoi samples [19, 54]

Choose samples $\{\lambda^{(j)}\}_{j=1}^N$ defining the partition $\{\mathcal{V}_j\}_{j=1}^N \subset \Lambda$ of Λ .

For $M \gg N$, let $\{\lambda_e^{(i)}\}_{i=1}^M \subset \Lambda$ denote a set of uniform i.i.d. (with respect to μ_Λ) random samples.

Let $V_j \approx \mu_\Lambda(\mathcal{V}_j)$, $j = 1, \dots, N$.

for $i = 1, \dots, M$ **do**

for $j = 1, \dots, N$ **do**

if $\lambda_e^{(i)} \in \mathcal{V}_j$ **then**

$\iota(i) = j$

end

end

$\mu(\mathcal{V}_j) \approx V_j = \frac{\mu_\Lambda(\Lambda)}{M} \#\{i : \iota(i) = j\}$.

the numerical solution to the stochastic inverse problem is dependent on the accuracy of approximating sets in Λ and \mathcal{D} . Recall, that the component maps of Q are assumed geometrically distinct. That is the Jacobian of Q has full rank at almost every point in Λ . Similarly, if A is a $d \times n$ matrix with $d \leq n$, then a solution $Ax = b$ exists for all $b \in \mathbb{R}^d$ if and only if A has full rank. The accuracy of the solution of $Ax = b$ depends on the condition number of A , in the same way the accuracy of the numerical solution of the stochastic inverse problem depends on a “skewness” property of the Jacobian of Q .

For simplicity consider the case where Q is a $d \times n$ matrix. This represents a linear mapping $Q : \Lambda \subset \mathbb{R}^n \rightarrow \mathcal{D} \subset \mathbb{R}^d$. We can restrict Q to $Q_\mathcal{L} : \mathcal{L} \rightarrow \mathcal{D}$ by fixing a transverse parameterization. This is analogous to restricting Q to an invertible $d \times d$ matrix. The condition of the inverse problem depends on the dependencies between the rows of $Q_\mathcal{L}$. If each row of $Q_\mathcal{L}$ rep-

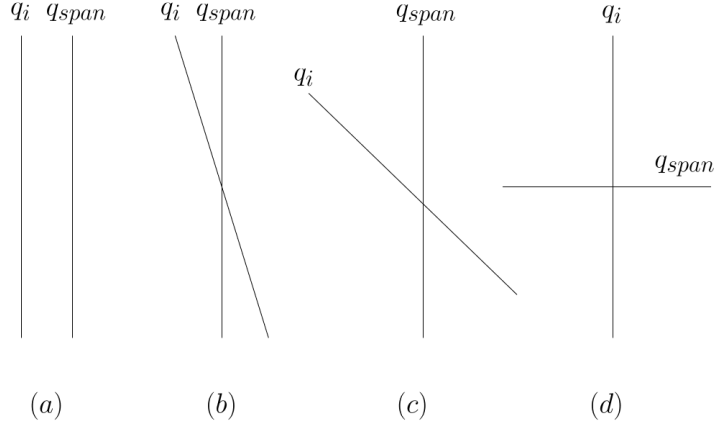


Figure 3.5: Illustration of linear QoI maps Q of varying skewness where q_i is a d -dimensional vector and q_{span} represents the hyperplane associated with $\text{span} \{ \{q_1, \dots, q_d\} \setminus q_i \}$. In (a) the generalized contours are *not* geometrically distinct. In (b)-(d) the generalized contours are geometrically distinct and progress from highly skewed (b) to perfectly unskewed (d).

resents a vector in \mathbb{R}^d the dependencies between the rows of $Q_{\mathcal{L}}$ are reflected by the angles the row vectors of $Q_{\mathcal{L}}$ make with respect to each other, these correspond with the angles of intersection the generalized contours of the component maps make with respect to each other. If the generalized contours of component maps are parallel, then the rows of $Q_{\mathcal{L}}$ are linearly dependent and the component maps of Q are not geometrically distinct. Figure 3.5 illustrates linear QoI maps Q of varying skewness where q_i is a d -dimensional vector and q_{span} represents the hyperplane associated with $\text{span} \{ \{q_1, \dots, q_d\} \setminus q_i \}$.

Definition 3.2.1. Given a vector q_i and a map $Q_{\mathcal{L}}$ we can define,

$$\text{skew}(Q_{\mathcal{L}}, q_i) = \frac{\|q_i\|}{\|q_i^\perp\|} \quad (3.2.8)$$

where q_i is a column of $Q_{\mathcal{L}}$, $q_i = q_i^\perp + q_i^0$, $q_i^\perp \perp q_i^0$, $q_i^0 \in \text{span} \{ \{q_1, \dots, q_d\} \setminus q_i \}$.

Correspondingly, we define,

$$\text{skew}(Q_{\mathcal{L}}) = \max_i (\text{skew}(Q_{\mathcal{L}}, q_i)) \quad (3.2.9)$$

If we imagine the transformation of a hyper-rectangle $A \subset \mathcal{L}$ under $Q_{\mathcal{L}}$ we will obtain a generalized parallelepiped in \mathcal{D} whose volume is $\det(Q_{\mathcal{L}})\mu_{\mathcal{L}}(A)$. In [32], it is shown that $\det Q_{\mathcal{L}} = \prod_i \|q_i^\perp\|$. If the map $Q_{\mathcal{L}}$ is “perfectly conditioned” (i.e., $\text{skew}(Q_{\mathcal{L}}) = 1$) then the resulting parallelepiped will still be a hyper-rectangle although it may be scaled or rotated, scaling does not affect the numerical solution of the inverse problem. However, if the map $Q_{\mathcal{L}}$ is not perfectly conditioned, the resulting parallelepiped will be skewed or sheared. These q_i^\perp , q_i^0 exist and can be ordered such that $\text{skew}(Q_{\mathcal{L}}, q_1) \geq \dots \geq \text{skew}(Q_{\mathcal{L}}, q_{d-1}) \geq 1$.

Recall that Algorithm 1 requires a discrete partitioning of both Λ and \mathcal{D} . If we assume $\text{skew}(Q_{\mathcal{L}}) = \text{skew}(Q_{\mathcal{L}}, q_1) \gg \text{skew}(Q_{\mathcal{L}}, q_d)$ and $\prod_{i=2}^d \|q_i^\perp\| \approx \|q_1\|^{d-1}$. Let $\epsilon = \text{skew}(Q_{\mathcal{L}})$. If we discretize \mathcal{D} with hypercubes then their size must be $(\gamma\epsilon\|q_1\|)^d$ for some $0 < \gamma \ll 1$ to avoid a poor set approximation of \mathcal{D} . We must also discretize \mathcal{L} . To avoid errors in the computation of the inverse images of cells in \mathcal{D} the cells that discretize \mathcal{L} must have a volume in \mathcal{D} such that $\sigma^d \det(Q_{\mathcal{L}}) \leq (\gamma\epsilon\|q_1\|)^d$ where σ^d is the volume of the cell in \mathcal{L} . This

implies that the number of samples $\{\lambda^{(j)}\}_{j=1}^N$ required to solve the stochastic inverse in Algorithm 1 is proportional to

$$\gamma^{-d}(\text{skew}(Q_{\mathcal{L}}))^{d-1}. \quad (3.2.10)$$

When Q is nonlinear the number of samples $\lambda^{(j)}$ required to solve the stochastic inverse in Algorithm 1 is proportional to

$$\left(\max_i(\text{skew}(J_{Q_{\mathcal{L}}}(\lambda^{(i)})))\right)^{d-1} \quad (3.2.11)$$

where $\lambda^{(i)} \in \mathcal{V}_i$ such that $Q_{\mathcal{L}}$ is locally linear in \mathcal{V}_i around $\lambda^{(i)}$ [32].

Ultimately, the goal is to use the solution of the inverse problem for prediction. Generally, a set of possible parameters with a smaller support will result in a set of possible outcomes with a smaller support and more precision in predictive modeling. However, if the QoI map used for the stochastic inverse problem has large skewness the solution to the stochastic inverse $Q^{-1}(E)$ problem will have a large support even if the region $E \in \mathcal{D}$ has small support, thus the volume of possible outcomes from the prediction problem may also be large. This emphasizes that *both* for the stochastic inverse problem and related prediction problems the careful selection of quantities of interest to form the QoI map is important.

Chapter 4

Numerical Results

4.1 Definition of the Stochastic Inverse Problem for Manning's n parameter using ADCIRC

We formulate the stochastic inverse problem to quantify uncertainty in the Manning's n coefficient using the ADCIRC model. Recall in Chapter 3 that the inverse problem is defined by a parameter domain and a vector-valued QoI map. The parameter domain, $\Lambda \subset \mathbb{R}^{+n}$, is the bounded n -dimensional hyper-rectangle (orthotope) defined by the product of n intervals of Manning's n values. We determine these intervals based on empirical data and expert engineering knowledge so that the parameter domain contains physically plausible Manning's n coefficients for each land cover classification. We choose the QoI map $Q : \Lambda \rightarrow \mathcal{D}$ to be the map from the Manning's n coefficients to $\mathcal{D} := Q(\Lambda)$, some subspace of all the physically plausible observable data (e.g., maximum water elevations at d gauge sites over a specific simulation time-window) simulated by the ADCIRC model.

Since the ADCIRC model is deterministic and Q is a (piecewise-smooth) vector-valued function, there exist at most $d = n$ geometrically distinct QoI. If we define the possible set of QoI as the maximum water elevations defined at d gauge sites, then our experience dictates that we must select hydraulically

isolated gauge sites to choose geometrically distinct QoI. The quality of the approximation $P_{\Lambda, N}$ can generally be improved if the hydraulics at each gauge site are unaffected by the hydraulic conditions at the other gauge sites (i.e. the hydraulics at a gauge site are dominated by the local conditions at that site) [55]. Determining $d = n$ geometrically distinct QoI can be challenging as demonstrated in Section 4.3. However, we believe that this is highly dependent on the characteristics of the spatial domain and the model source terms. Even if $d = n$ geometrically distinct QoI are found the map Q may be significantly skewed so that inverting this map may be computationally impractical [32]. Recall in Section 3.1 that when $d < n$ the inverse, Q^{-1} , is set-valued. This implies that there exists an equivalence class of Manning's n coefficients that produce the same maximum water elevations at the d gauge sites simulated by the ADCIRC model. This is an example of deterministic aleatoric uncertainty that is fully represented and captured within the measure-theoretic framework for the non-stochastic inverse problem. Epistemic uncertainty is accounted for by solving the stochastic inverse problem with a given probability measure $P_{\mathcal{D}}$ defined by a probability density $\rho_{\mathcal{D}}$ on the *observable* data space \mathcal{D} . In this setting, the probability density $\rho_{\mathcal{D}}$ characterizes the uncertainty in a particular observation of $Q(\lambda) \in \mathcal{D}$ which is often due to measurement error.

We developed the Python package PolyADCIRC [21] to efficiently conduct parameter sweeps of Λ of P(arallel)ADCIRC on HPC systems. The Python package BET [22] provides non-model-specific tools for sampling (on regular grids, with uniform random sampling, and adaptive sampling) and im-

plementations of Algorithms 1 to 3 for post-processing the samples. Given the desired samples in Λ using a sub-package in BET, a set of land classification basis vectors, and the required input files for a particular ADCIRC simulation, PolyADCIRC runs batches of PADCIRC simulations and saves that output after each batch. The number of PADCIRC simulations per batch is user determined as is the number of processors per ADCIRC simulation. Individual ADCIRC simulations are assumed to require the same resources. Thus load balancing the PADCIRC simulations is trivial. Approximations of P_Λ using Algorithm 1 along with visualizations of results can be computed through post-processing via the BET package. The documentation for the PolyADCIRC package is available at [21] and the BET package and associated documentation are available at [22].

4.2 Defining a Mesoscale Representation of the Manning’s n Coefficient

We define a specific mesoscale representation of the Manning’s n field that is parameterized by the land cover classification in the physical domain. We consider the spatial distribution of land classifications to be certain. This parameterization removes the consideration of spatial uncertainty in the bottom friction field (as opposed to using a Karhunen–Loève expansion) thus significantly reducing the problem size. We summarize the numerical framework through which the parameter space, Λ , is explored. We briefly describe the spatial averaging procedure used to map land classification data onto the

unstructured finite element mesh used by ADCIRC. For more details on the current implementation see Appendix B. We also direct the interested reader to [21] where up-to-date code and documentation are available.

Given a computational mesh, pixelated land cover classification data, and $\boldsymbol{\lambda} = \{\lambda_i\}_{i=1}^n \in \mathbb{R}^{+n}$, where λ_i is the Manning's n coefficient associated with the i^{th} land classification and n is the number of land classifications, we desire a mapping of Manning's n to the M nodes of the computational mesh that is cheap to evaluate. For a fixed $\boldsymbol{\lambda}$, the spatial averaging process to map Manning's n values to the nodes is as follows. Define the grid scale at each node in the computational mesh as the rectangle that encloses the maximum and minimum x, y -coordinates of the centroids of the elements that contain the node (see Figure 4.1) [26]. Set the nodal Manning's n value to the average

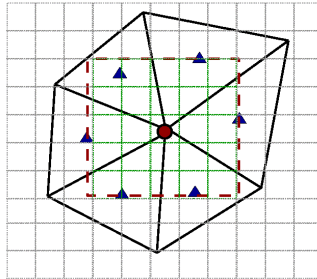


Figure 4.1: The grid scale at the red node is shown as the red dashed box. The centroids are shown in blue. The underlying pixels are outlined in gray and the pixels within the grid scale are green. This is a modified figure from [26].

of the Manning's n coefficients of the land cover classification pixels contained within the grid scale. We can also choose to spatially average data within $1\times$, $2\times$, $4\times$, or $8\times$ the grid scale. However, $2\times$ is recommended to prevent

over/under smoothing of the data [15, 32]. Hence, the Manning's n coefficient at the j^{th} node in the mesh is

$$n_j = \frac{1}{N_j} \sum_{i=1}^m a_{ij} \lambda_i, \quad \forall j \in \{1, \dots, M\} \quad (4.2.1)$$

where λ_i is the Manning's n coefficient for the i^{th} land classification, a_{ij} is the number of pixels within the grid scale at the j^{th} node for the i^{th} land classification, and $N_j = \sum_{i=1}^m a_{ij}$ is the total number of pixels within the grid scale at the j^{th} node.

This spatial averaging process is a linear map. Thus, we can construct a set of land cover classification meshes $\{\mathbf{b}_i\}_{i=1}^m$ with $\{b_{ij}\}_j = a_{ij}$ such that we can represent a given Manning's n field for a particular finite element mesh as the vector \mathbf{n} where,

$$\mathbf{n} = [\mathbf{b}_1 \dots \mathbf{b}_m] \cdot \boldsymbol{\lambda} \quad (4.2.2)$$

$$\mathbf{n} = \{n_j\}_{j=1}^M. \quad (4.2.3)$$

We call these \mathbf{b}_i basis vectors since the \mathbf{n} in Equation (4.2.3) is a linear combination of these vectors. Figure 4.2 shows the basis vectors for a physical domain modeling an inlet with three land classifications and a particular mesoscale representation of the Manning's n field with $\lambda_1 = 0.142$, $\lambda_2 = 0.161$, and $\lambda_3 = 0.012$.

The above process defines the mesoscale representation of Manning's n fields in terms of a linear mapping from Λ to $\mathbf{n} \in \mathbb{R}^{+M} \subset \mathbb{R}^{+\infty}$ where \mathbf{n} is the vector representation of the continuous, piecewise-linear mesoscale parameter

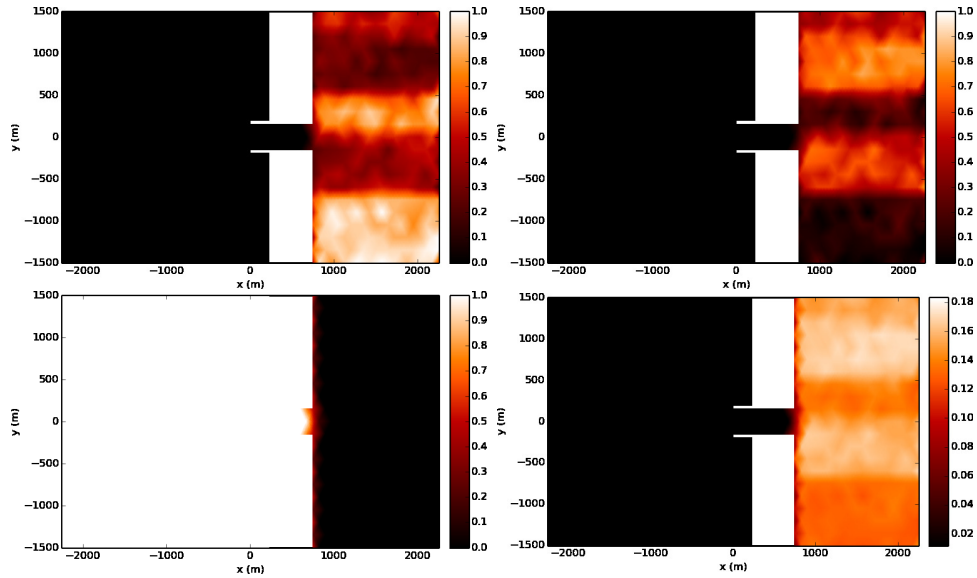


Figure 4.2: This demonstrates how to construct a prototypical mesoscale representation of Manning’s n values from basis vectors defining a linear mapping from land classification types. Top Left: Basis Vector 1. Top Right: Basis Vector 2. Bottom Left: Basis Vector 3. Bottom Right: Spatially averaged Manning’s n field using synthetic data. Note that in the inlet area (right-hand side) this is considered a shallow area and two land classification types are heavily mixed. Compare this to the deeper (left-hand) side of the domain where it is common practice to assign a single land classification type with lower Manning’s n value in such areas.

field for a given set of empirical land classification data. We construct these basis vectors in parallel using PolyADCIRC [21] which contains a Python wrapped version of GridData [26]. The process of upscaling from the land classifications to the type of mesoscale representation described above has been well studied and is a generally accepted method for determining the Manning’s n field [15]. A large source of uncertainty is in the specification of the associated Manning’s n coefficients to each type of land classification. Thus, the uncertain

parameters $\boldsymbol{\lambda} \in \Lambda$ are the Manning's n coefficients associated with each land cover classification.

4.3 Inlet Case Study

We model the SWEs on an idealized inlet with sloped bathymetry shown in Figure 4.3 using ADCIRC. The left boundary is an open ocean boundary with a M_2 tidal amplitude of $1.2 [m^2/s]$ entering the domain normal to the boundary. The remainder of the boundary is a land boundary ($\mathbf{u} \cdot \mathbf{n} = 0$ and no slip). The flow is obstructed by an earthen jetty extending from $y = 1500 [m]$ along the y -coordinate into the domain between $x = 1420 [m]$ and $1580 [m]$.

We define the QoI from the maximum elevation¹ recorded at specific locations within Ω . The physical coordinates in Ω for these QoI are listed and shown in Figure 4.3, and we henceforth refer to these locations as observation stations. Note results from this section have been previously published in [32].

4.3.1 Two Dimensional Parameter Space

We consider the situation where the Manning's coefficients λ_1 and λ_2 for the land cover classifications 1 and 2 in Figure 4.2 are uncertain with known bounds (see Table 4.1). Let $\Lambda = [0.07, 0.15] \times [0.1, 0.2] \subset \mathbb{R}^2$ denote the parameter domain. For this example, the length of the earthen jetty is fixed

¹Other possible QoIs of interest may be the time of inundation, maximum velocity, time of maximum inundation, etc.

Parameter	Range of Manning's n values	Land Classification
λ_0	0.012	Water
λ_1	[0.07, 0.15]	Wetland
λ_2	[0.1, 0.2]	Forest

Table 4.1: Manning's n Ranges for the Idealized Inlet.

and extends from $y = 1500[m]$ to $y = -1050[m]$.

Usually the mesoscale representation of Manning's n is defined on the finite element mesh (see [7,15]). However, significant numerical errors can arise when the finite element mesh scale matches the mesoscale of the Manning's coefficient field since we are modeling the flow at a scale where both the assumptions of the SWEs apply and the finite element mesh adequately resolves variability in the Manning's coefficient field. We reduce these errors by using the refined finite element mesh shown in Figure 4.3 and maintain the fixed mesoscale representation of Manning's coefficient by interpolating the values (as shown in Figure 4.2) onto the refined finite element mesh.

The resulting QoI maps are noticeably smoother due to the reduction in numerical model error from both the inadequate representation of the earthen jetty and resolution of the variation of the mesoscale Manning's coefficient field. For example, compare the two plots in Figure 4.4 where the use of a refined finite element mesh removes spurious numerical results, shifts the QoI values by approximately $0.5 [m]$ over the entire domain, and significantly alters the slopes of the contours. In the case where a posteriori error estimates are available, these may be used to improve the QoI map and geometry of the generalized

contours as demonstrated with adjoints in [18, 20, 56]. Unfortunately, these error estimates are not available for ADCIRC. Instead we have refined the finite element mesh until the QoI values have appeared to converge with respect to the mesoscale mesh size. Ideally, this should be done so that the scale of the mesoscale mesh is larger than that of the finite element mesh. We form a surrogate (piecewise-linear interpolant) with the resulting smooth QoI map on a regular 21×21 grid of forward model solves of Λ defining a 20×20 rectangular partition $\{R_k\}_{k=1}^{20^2}$ of Λ on which we desire to estimate P_Λ . We sample from the surrogate on a regular 121×121 grid and use Algorithm 1 to estimate P_Λ using the resulting counting measure.

Ideally we desire $d = 2$ geometrically distinct QoI to invert the map from \mathcal{D} to Λ . Given 12 observation stations recording maximum water elevations, we determine which of these QoI result in a well-conditioned inverse problem (i.e. $\text{skew}(Q) \approx 1$, see Section 3.2.4). In this chapter q_i, q_1 correspond to the station numbering and not the q_i, q_1 in the skewness derivation. For the sake of simplicity and presenting representative results, we fix the maximum elevation at station 1, q_1 as the first component of Q . Maximum elevation data from stations 2 - 12 produce the domains $\mathcal{D} = \{q_1, q_n\} \forall n = 2, \dots, 12$ (see representative plots in Figure 4.5). Plots of these data domains are useful diagnostic tools for determining which additional QoI impose a family of generalized contours that are most orthogonal to those imposed by q_1 . Each contour from one component map intersects a “set of contours” from the other component map. The orthogonality of these families of contours cor-

responds directly to the relative size of the domain \mathcal{D} . With this in mind, we see that the map $Q(\lambda) = (q_1(\lambda), q_6(\lambda))$ produces the “best” \mathcal{D} and the map $Q(\lambda) = (q_1(\lambda), q_2(\lambda))$ produces the “worst” \mathcal{D} in Figure 4.5. We note that station 6 is located upstream of a location dominated by land cover classification 2 whereas station 1 is located in an area dominated by land cover classification 1. As we move from station 2 to station 6, we move further from station 1 in the spatial domain and the data domain \mathcal{D} “thickens” indicating that the skewness of $Q = (q_1, q_n)$ is decreasing, thus we have a better conditioned inverse problem. The ranges of QoI produced from the omitted stations 7 – 12 are comparable to expected measurement errors and are thus not very useful.

We define and show three stochastic inverse problems to quantify uncertainty in Manning’s n values using three different QoI maps. We define $\rho_{\mathcal{D}}$ as a uniform distribution on a rectangle² centered at Q_{ref} . We define $Q_{ref} = Q(\lambda_{ref})$ for a reference parameter. Since $\rho_{\mathcal{D}}$ is uniform on a hyper-rectangle we can exactly represent $\rho_{\mathcal{D}}$ with a simple function $\rho_{\mathcal{D},M}$ by choosing a partition $\{I_i\}$ such that there exists a subset of $\{I_i\}$ equal to R_{ref} where $\rho_{\mathcal{D}}$ is uniform on R_{ref} as illustrated in Figure 4.6. We then follow the steps of Algorithms 1 and 2 in Section 3.2 using the 121^2 samples of Λ to estimate P_{λ} .

Figure 4.7 shows the resulting estimates of $\rho_{\Lambda,N}$. We correctly identify a region of high probability in Λ containing λ_{ref} for each of the three stochastic inverse problems. The results from the map $Q(\lambda) = (q_1(\lambda), q_6(\lambda))$ identify a

²We choose the lengths of the sides to be 15% the length of q_1 and q_n .

region of high probability in parameter space containing the reference parameter of comparatively small volume. This is due to the near orthogonality of the families of generalized contour generated by the QoI component maps as shown by the size of the domain \mathcal{D} in Figure 4.5. Thus we can choose QoI maps based on the underlying geometric structure of the generalized contours to obtain probability measures with smaller support (than other QoI maps). If the goal is to solve a stochastic inverse problem for parameter estimation then identifying small regions of highly probable parameter configurations provides valuable information towards that aim.

Ultimately, one further goal may be to use the results of parameter estimation for prediction. Let $Q_a = (q_1, q_2)$ and $Q_b = (q_1, q_6)$ be two different QoI maps. Figures 4.5 and 4.7 demonstrate that $\text{skew}(Q_a) > \text{skew}(Q_b)$ and $\mu_\Lambda(Q_a^{-1}(E_a)) > \mu_\Lambda(Q_b^{-1}(E_b))$ where $E_a = \text{supp}(\rho_{\mathcal{D}_a})$, $E_b = \text{supp}(\rho_{\mathcal{D}_b})$ are defined by the reference values $Q_a(\lambda_{ref}) \in \mathcal{D}_a$, $Q_b(\lambda_{ref}) \in \mathcal{D}_b$ respectively. Note that $E_a \cap E_b \neq \emptyset$, $Q_a(\lambda_{ref}) \cap Q_b(\lambda_{ref}) \neq \emptyset$ and $Q_a^{-1}(E_a) > Q_b^{-1}(E_b) \neq \emptyset$. Now consider a prediction map $F : \Lambda \rightarrow \mathcal{P}$ to be a mapping from the parameter space to some prediction space composed of functionals on the model solution $Y(\lambda)$. We expect $\mu_{\mathcal{P}}(F(Q_a^{-1}(E_a))) > \mu_{\mathcal{P}}(F(Q_b^{-1}(E_b)))$. In other words when making a prediction using the solution of an inverse problem the image in the prediction space \mathcal{P} of the solution to the inverse problem with smaller skewness, Q_b , will be smaller than if we had used a map Q_a with more skewness. We demonstrate this by predicting the time of inundation at $(x_1, y_1) = (1593.75, -1087.5)$ and $(x_2, y_2) = (1593.75, -1012.5)$ for regions

Location (x, y)	Interval, Interval size		Inundation t
	(q_1, q_2)	(q_1, q_6)	
(x_1, y_1)	[16:36:50, 19:08:56], 9126s	[18:01:36, 19:08:56], 4040s	18:36:58
(x_2, y_2)	[26:35:38, 27:18:52], 2596s	[27:14:24, 27:19:14], 290s	27:17:08

Table 4.2: The prediction of the time of inundation for the idealized inlet [32].

in Λ containing 95% of the total probability using the solution of the inverse problem for the maps $Q = (q_1, q_2)$ and (q_1, q_6) . The intervals of possible time of inundation are shown in Section 4.3.1. The intervals of possible time of inundation at (x_1, y_1) and (x_2, y_2) for the worse conditioned map $Q = (q_1, q_2)$ is respectively about 2.3 and 9 times the size of the intervals for the map $Q = (q_1, q_6)$ which is better conditioned. Thus choosing a well-conditioned map to solve the stochastic inverse problem can have dramatic effects on the forward prediction problem.

4.3.2 Three Dimensional Parameter Space

The focus of this section is on the problem of determining $d = n$ geometrically distinct QoI and the effect that the choice of QoI has on the approximation of P_Λ . We form a surrogate (linear interpolant) of the model and explore this issue numerically. We consider the scenario where both the length of the earthen jetty and the Manning's n coefficients for the land cover classifications 1 and 2 in Figure 4.2 are uncertain with known bounds. Hence, the parameters for this problem are the Manning's n coefficients for land cover classifications 1, 2, and the lowermost y -coordinate of the wall. Let $\Lambda = [-900, 1500] \times [0.07, 0.15] \times [0.1, 0.2] \subset \mathbb{R}^3$ denote the parameter domain

with jetty length as the first component. Thus we seek $d = 3$ geometrically distinct QoI to invert the map from \mathcal{D} to Λ . We again approach this problem from the perspective of parameter estimation. We consider three different QoI maps and three choices of $\rho_{\mathcal{D}}$ defined by different λ_{ref} as in Section 4.3.1. We use a piecewise-linear interpolant formed on a regular rectangular partition of Λ generated by 21^3 model evaluations as a surrogate to sample Q on a regular grid of 51^3 samples. We use these samples in Algorithm 1 to estimate P_{Λ} using a counting measure.

Figures 4.9 to 4.11 show the resulting approximation of $P_{\Lambda,N}(R_k)$ computed on 20^3 regular rectangular boxes $\{R_k\}$ partitioning Λ for various choices of the QoI where the density $\rho_{\mathcal{D}}$ is defined by a uniform density on a hyper-rectangle centered at λ_{ref} . In Figure 4.9, we can identify a relatively small area defined by the 1-dimensional generalized contours containing λ_{ref} with high probability using the approximation $P_{\Lambda}(R_k)$ computed using the map $Q(\lambda) = (q_1(\lambda), q_5(\lambda))$.

If we define $Q(\lambda) = (q_1(\lambda), q_5(\lambda), q_2(\lambda))$ we observe that the plots of the approximation $P_{\Lambda}(R_k)$ in Figure 4.10 are essentially the same as those shown in Figure 4.9. The structure of $P_{\Lambda}(R_k)$ is nearly identical because q_1 and q_2 produce nearly parallel generalized contours as shown in Figure 4.10 (i.e. q_1 and q_2 have large skewness). In essence, the observations at station 2 provide nearly the same geometric information as the observations at station 1. This implies that \mathcal{D} is not a “true” 3-dimensional subdomain of $q_1(\Lambda) \times q_5(\Lambda) \times q_2(\Lambda)$. Instead \mathcal{D} resembles a 2-dimensional manifold with some incidental thickness.

Similar results are obtained for the QoI map $Q(\lambda) = (q_1(\lambda), q_5(\lambda), q_{12}(\lambda))$ and are shown in Figures 4.11 and 4.12 . We encountered this problem for all of the combinations of the QoI we simulated. This suggests that we should only use two QoI which result in 1-dimensional generalized contours in Λ [32].

The local skewness of the Jacobian of the map Q about $Q(\lambda_{ref})$ also plays a significant role in the quality of the approximate probability measure $P_\Lambda(R_k)$. The Jacobian of the map $Q = (q_1, q_5, q_2)$ about $Q(-600.0, 0.073, 0.119)$ is locally relatively well-conditioned with results nearly identical to Figure 4.10, however this is not true for all $\lambda \in \Lambda$. We solve the stochastic inverse problem using the map $Q(\lambda) = (q_1(\lambda), q_5(\lambda), q_{12}(\lambda))$ for two values of λ_{ref} . We first choose $\lambda_{ref} = (-750.0, 0.118, 0.135)$ as shown in Figure 4.11. We are able to correctly identify a small interval containing the reference jetty length, (λ_1) , and a high probability region in the λ_2, λ_3 -plane containing (λ_2, λ_3) values.

The reference solutions in the previous data domain $Q = (q_1, q_5, q_2)$ were contained in a region of the data domain that resembles a 2-dimensional manifold with incidental thickness. Now, consider the case where $\lambda_{ref} = (1200.0, 0.146, 0.128)$, $Q(\lambda_{ref})$ is contained in the lowermost portion of $Q(\Lambda) = \{q_1(\Lambda), q_5(\Lambda), q_{12}(\Lambda)\}$ as shown in Figure 4.12. In this region of \mathcal{D} the 2-dimensional manifold has collapsed to resemble a 1-dimensional curve. This corresponds to large skewness. Near $\lambda_{ref} = (1200.0, 0.146, 0.128)$ the QoI map appears to give only lower-dimensional information in this region of Λ . The aleatoric uncertainty increases as the apparent dimension of generalized contours increases. We observe in Figure 4.12 that the resulting estimates of

$P_\Lambda(R_k)$ assign non-zero probability to a large region of parameter space containing λ_{ref} (as opposed to a high probability region with small μ_Λ -measure). There is simply not enough useful geometric information to correctly identify an event of high probability in the λ_2, λ_3 -plane with small area. In conclusion, the problem of finding $d = n$ geometrically distinct QoI that form a locally well-conditioned map Q can be difficult.

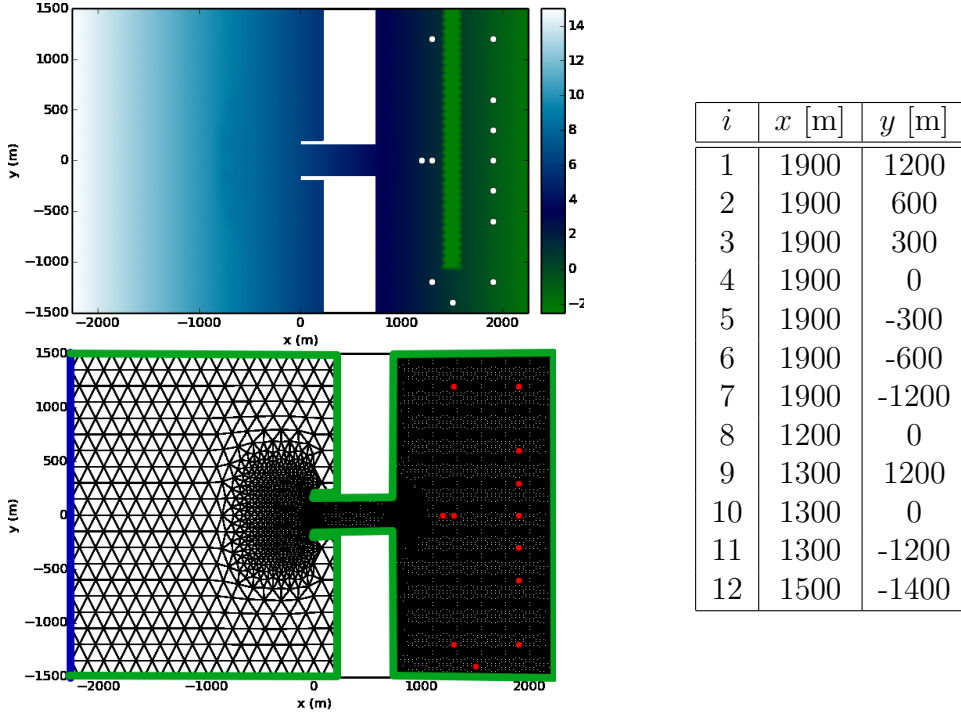


Figure 4.3: The physical domain for the idealized inlet. Top Left: Bathymetry of the physical domain Ω in Eq. (2.1.1) and Eq. (2.1.2) with observation stations marked by circles. Bottom Left: Discretization of the domain. Right: The xy -coordinates of observation stations in Ω for observing QoI. Observations of a QoI from the i^{th} observation station are designated $q_i(\lambda)$. We can then choose to examine a particular QoI map, e.g., $Q(\lambda) = (q_1(\lambda), q_5(\lambda), q_{12}(\lambda))$ or $Q(\lambda) = (q_1(\lambda), q_7(\lambda))$. Recall that $Q(\lambda) \in \mathbb{R}^d$ and $d \leq n$, so there are at most n geometrically distinct observation stations.

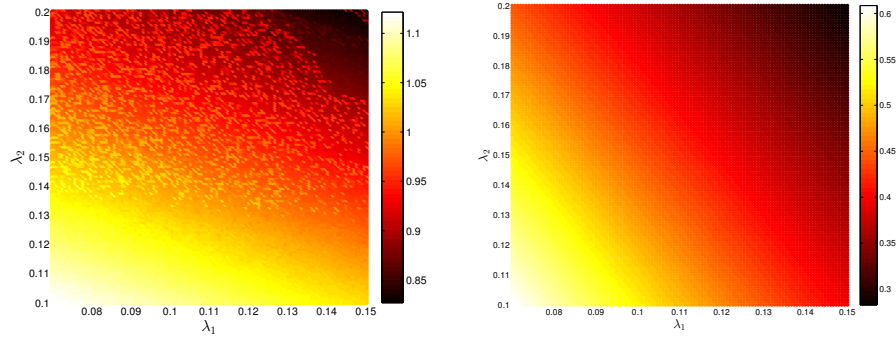


Figure 4.4: Left: The QoI map $Q(\lambda) = (q_1(\lambda))$ of the maximum elevation measured at station 1 computed on a finite element mesh that matches the mesoscale representation of Manning's n . Right: The QoI map on the refined finite element mesh shown in Figure 4.3. Note the difference colorbar scales, smoothness of the responses, and changes in the gradient due to the use of the refined finite element mesh.

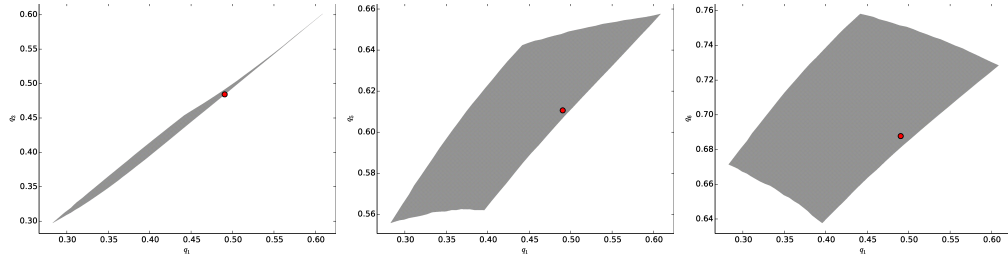


Figure 4.5: The estimated data domain $\mathcal{D} := Q(\Lambda) = \{q_1(\Lambda), q_n(\Lambda)\}$ for $n = 2$ (left), $n = 5$ (center), $n = 6$ (right) computed with a regular 121^2 grid of samples. The reference Q_{ref} for $(\lambda_1, \lambda_2) = (0.107, 0.106)$ is marked in red.

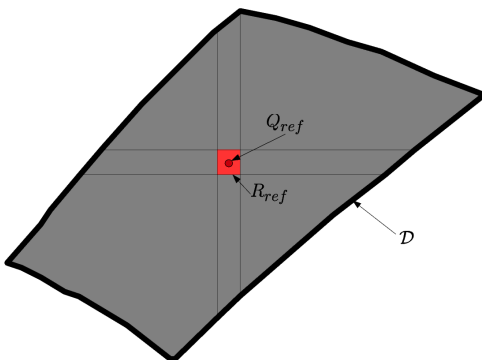


Figure 4.6: An illustration of a partitioning $\{I_i\}_{i=1}^9 \subset \mathcal{D}$ of $\mathcal{D} := Q(\Lambda)$ where there exists an $I_i = R_{ref}$ show in red. Q_{ref} is illustrated by a red dot. If we use this partition to create a simple function approximation of $\rho_{\mathcal{D}}$ where $\rho_{\mathcal{D}}$ is uniform on R_{ref} we can exactly represent $\rho_{\mathcal{D}}$ by $\rho_{\mathcal{D},9}$ with the partitioning of \mathcal{D} illustrated here.

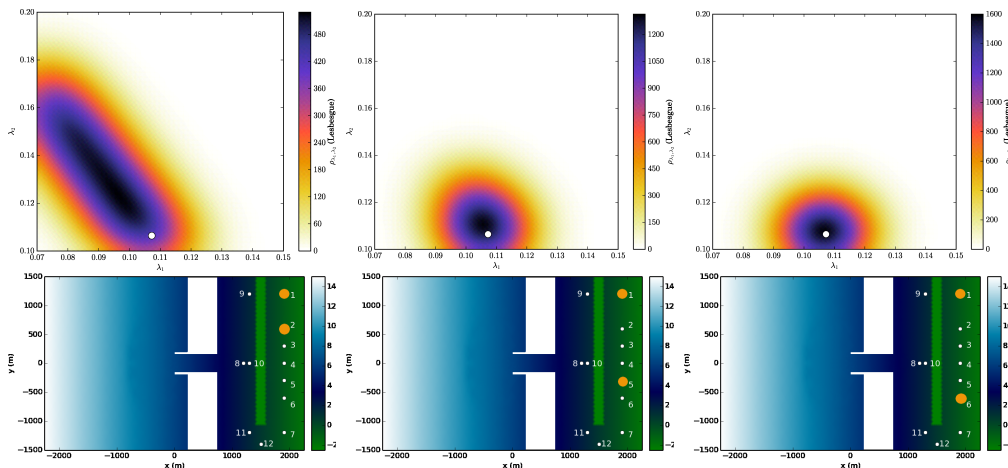


Figure 4.7: Top Row: The approximation of ρ_{Λ} on for $Q(\lambda) = (q_1(\lambda), q_2(\lambda))$, $(q_1(\lambda), q_5(\lambda))$, and $(q_1(\lambda), q_6(\lambda))$ for the first, second, and third columns respectively where $\lambda_{ref} = (\lambda_1, \lambda_2) = (0.107, 0.106)$ is marked by a black dot. Bottom Row: The observation stations in the physical domain for $Q(\lambda) = (q_1(\lambda), q_2(\lambda))$, $(q_1(\lambda), q_5(\lambda))$, and $(q_1(\lambda), q_6(\lambda))$ for the first, second, and third columns respectively.

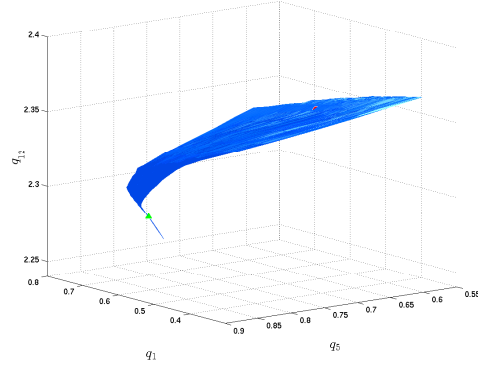


Figure 4.8: The set $Q(\Lambda) = (q_1(\Lambda), q_5(\Lambda), q_{12}(\Lambda))$ for $\Lambda = [-900, 1500] \times [0.07, 0.15] \times [0.1, 0.2]$. The points $Q(-750.0, 0.118, 0.135)$ and $Q(1200.0, 0.146, 0.128)$ are denoted by a red circle and green triangle, respectively.

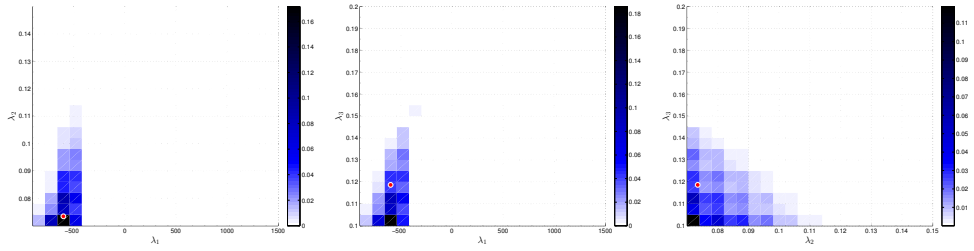


Figure 4.9: Marginal plots of the approximation of $P_{\Lambda, N}(R_k)$ for the map $Q(\lambda) = (q_1(\lambda), q_5(\lambda))$ computed by inverting a uniform probability measure centered on Q_{ref} on 20^3 cubes partitioning Λ . The marginals for the λ_1, λ_2 - (left), λ_1, λ_3 - (middle), and λ_2, λ_3 - planes (right), respectively. The reference, Q_{ref} and $\lambda_{ref} = (-600.0, 0.073, 0.119)$ is denoted by red circles respectively.

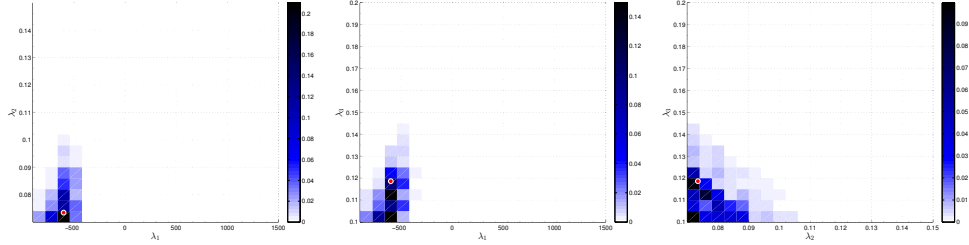


Figure 4.10: Marginal plots of the approximation of $P_\Lambda(R_k)$ for the map $Q(\lambda) = (q_1(\lambda), q_5(\lambda), q_2(\lambda))$ computed by inverting a uniform probability measure centered on Q_{ref} on 20^3 cubes partitioning Λ . The marginals for the λ_1, λ_2 - (left), λ_1, λ_3 - (middle), and λ_2, λ_3 - planes (right), respectively. The reference Q_{ref} and $\lambda_{ref} = (-600.0, 0.073, 0.119)$ is denoted by red circles.

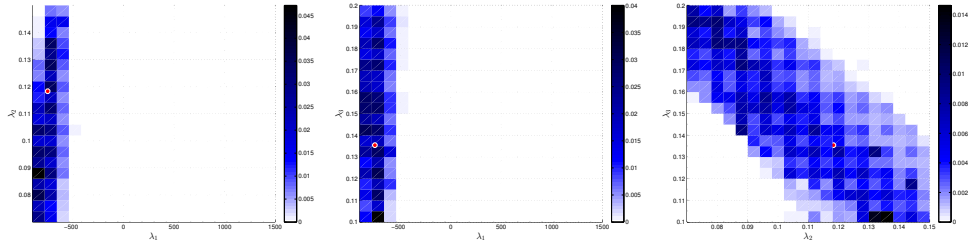


Figure 4.11: Marginal plots of the approximation of $P_\Lambda(R_k)$ for $Q(\lambda) = (q_1(\lambda), q_5(\lambda), q_{12}(\lambda))$ computed by inverting a uniform probability measure centered on Q_{ref} on 20^3 cubes partitioning Λ . The marginals for the λ_1, λ_2 - (left), λ_1, λ_3 - (middle), and λ_2, λ_3 - (right) planes, respectively. The reference Q_{ref} and $\lambda_{ref} = (-750.0, 0.118, 0.135)$ is denoted by red circles.

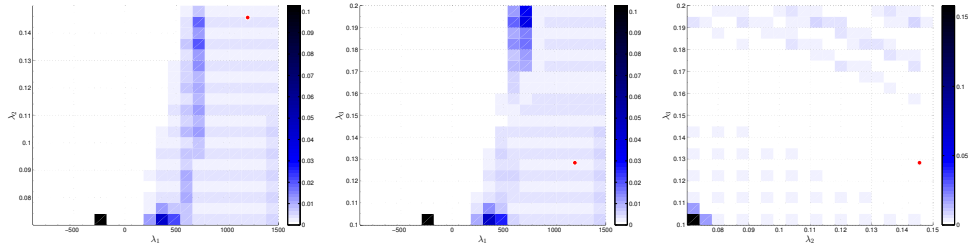


Figure 4.12: Marginal plots of the approximation of $P_\Lambda(R_k)$ for $Q(\lambda) = (q_1(\lambda), q_5(\lambda), q_{12}(\lambda))$ computed by inverting a uniform probability measure centered on Q_{ref} on 20^3 cubes partitioning Λ . The marginals for the λ_1, λ_2 - (left), λ_1, λ_3 - (middle), and λ_2, λ_3 - (right) planes, respectively. The reference, Q_{ref} and $\lambda_{ref} = (1200.0, 0.146, 0.128)$ is denoted by red circles.

4.4 Hurricane Gustav Case Study

In this section we show results from a case study for Hurricane Gustav. We have applied computational measure-theoretic algorithms for quantifying uncertainty in mesoscale representations of Manning's n fields for an idealized inlet domain with a simple forcing scheme for two and three dimensional parameter domains. We have demonstrated the difficulty (and importance) of choosing geometrically distinct QoI maps that are also well-conditioned for the approximation of the probability measure P_Λ [32]. More complicated physical domains and forcing conditions increase the abundance of hydraulically isolated areas and make it easier to find geometrically distinct QoI. In this section we examine parameter estimation of Manning's coefficients using data of storm surge for Hurricane Gustav. We focus on a coastal region in Southern Louisiana and Mississippi affected by Hurricane Gustav. Hurricane simulations on meshes fine enough to resolve inundation are computationally expensive. We employ a recently available subdomain implementation of ADCIRC [23–25] to reduce simulation time and allow us to focus on specific regions of interest rather than the much larger domain normally required for hurricane simulations. Subdomains can feature as few as four distinct land classifications whereas the full domain may feature as many as twenty-three land classifications [15, 31].

The full domain ADCIRC model for Hurricane Gustav is based on the model in *Hurricane Gustav (2008) Waves and Storm Surge: Hindcast, Synoptic Analysis, and Validation in Southern Louisiana* [31] using the mesh shown

in Figure 4.13 developed over a number of years by various researchers. We use the same wind field and riverine inflows developed in [31]. We also increase water levels for Gustav by 0.22 [m] to adjust for steric expansion and vertical datum. After a 20 day tidal and riverine spin up we begin wind forcing at 15-minute intervals starting at 0000 UTC 26 August 2008 (approximately 6.5 days before landfall) and ending at 0000 UTC 4 September 2008 (approximately 2.5 days after landfall). However, this model differs from the hindcast in that we do not model waves with Simulating WAVes Nearshore (SWAN). SWAN is a spectral wave model developed at Delft University of Technology that can be tightly coupled to ADCIRC in the SWAN+ADCIRC model [57]. The full domain model contains 2,720,591 elements and runs to completion on 288 processors on Stampede [58] in approximately 11.5 hours. We use land cover classification data from the Coastal Change Analysis Program Regional Land Cover Atlas (C-CAP) [53] to create a set of land cover classification basis vector meshes. We fill in regions not covered by the C-CAP data with existing Manning’s n nodal data from the `cpra_2017_v07a` mesh. We use a $2\times$ grid scale so that the effective mesoscale of the Manning’s coefficient field is larger than the finite element mesh scale to prevent the computational issues shown in Section 4.3.1. The Manning’s n coefficients used for the full domain model are summarized in Table 4.3, the values on the continental shelf in the Gulf of Mexico are set to $n = 0.022$ for sand/gravel bottoms and $n = 0.012$ for muddy bottoms.

We reduce the cost of forward model evaluations by using Subdomain

C-CAP Class	Description	Manning's n
2	High-intensity developed	0.120
3	Medium-intensity developed	0.120
4	Low-intensity developed	0.120
5	Developed open space	0.035
6	Cultivated land	0.100
7	Pasture/hay	0.050
8	Grassland	0.035
9	Deciduous forest	0.160
10	Evergreen forest	0.180
11	Mixed forest	0.170
12	Scrub/shrub	0.080
13	Palustrine forested wetland	0.150
14	Palustrine scrub/shrub wetland	0.075
15	Palustrine emergent wetland	0.060
16	Estuarine forested wetland	0.150
17	Estuarine scrub/shrub wetland	0.070
18	Estuarine emergent wetland	0.050
19	Unconsolidated shore	0.030
20	Bare land	0.030
21	Open water	0.025
22	Palustrine aquatic bed	0.035
23	Estuarine aquatic bed	0.030

Table 4.3: Manning's n values for C-CAP classification. Reproduced from [31].

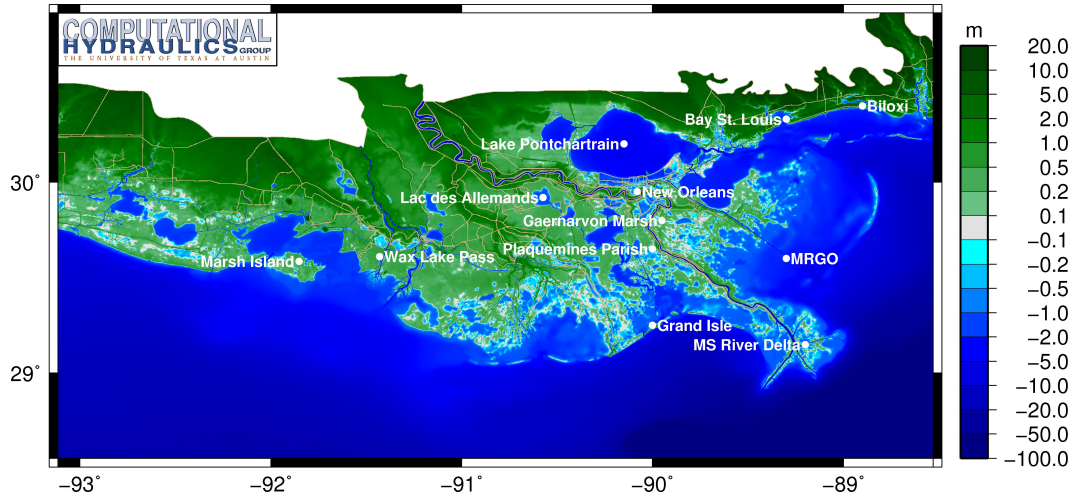


Figure 4.13: Bathymetry/topography (m) of the full domain mesh in south-eastern Louisiana.

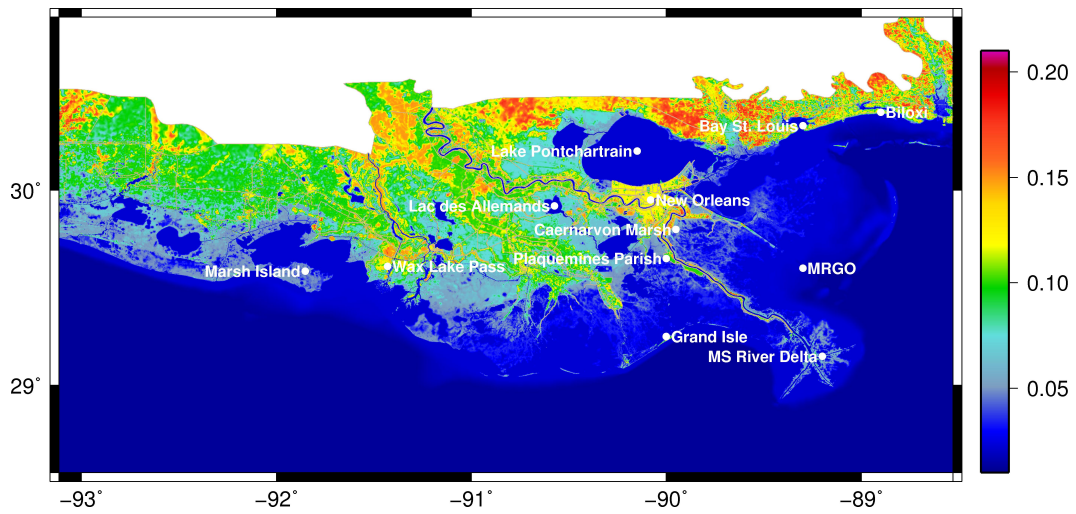


Figure 4.14: Manning's n values of the full domain mesh in southeastern Louisiana.

ADCIRC [23–25]. Results are shown for a subdomain extracted from the `cpra_2017_v07a` mesh in the Southern Louisiana and Mississippi area. The subdomain was chosen for the proximity to existing buoy data sites and geographic interest (e.g. inundation and complex local land classification distributions). The subdomain is focused on Bay St. Louis in Mississippi and contains 15,001 elements and is shown in Figure 4.15. Subdomain ADCIRC reduces the cost of forward model evaluations by forcing the boundary of the subdomain with the conditions from the full domain (velocity, sea surface height, wet/dry condition) [23–25]. Below is a brief overview of subdomain modeling in ADCIRC:

1. Create full domain ADCIRC model.
2. Create subdomain ADCIRC model:
 - (a) Extract input files from full domain ADCIRC model.
 - (b) Create subdomain specific files.
 - (c) Link meteorological forcing files in the subdomain directory.
3. Generate full domain control file to control output of subdomain boundary forcing data.
4. Run ADCIRC on the full domain.
5. Extract subdomain boundary forcing data from the full domain.
6. Run ADCIRC on the subdomain.

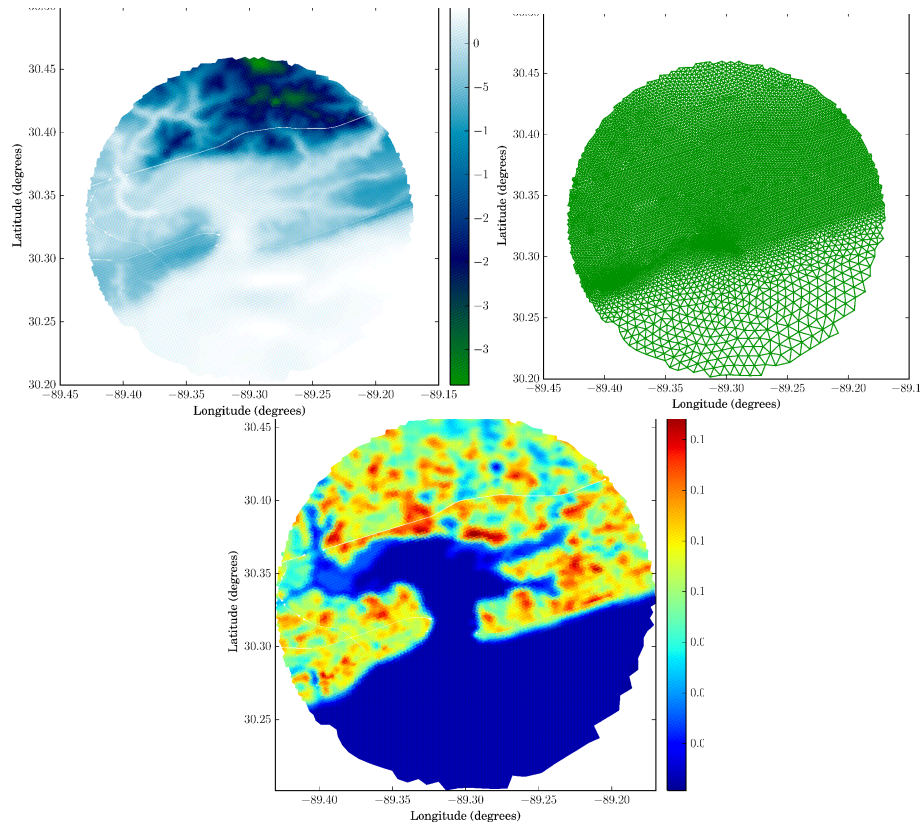


Figure 4.15: The physical domain for the subdomain. Top Left: Bathymetry of the physical domain Ω in Eq. (2.1.1) and Eq. (2.1.2). Top Right: Discretization of the domain. Bottom: The Manning's n field extracted from the full domain.

4.4.1 Subdomain Parameter Space

The parameter space for the subdomain model is determined as follows. Define a mesoscale representation of the Manning's n field parameterized by land cover classification as described in Section 4.2. Calculate the total fraction of each land cover classification as the sum of the nodal fractions of the land cover classification normalized by the total number of nodes, $\|\mathbf{b}_i\|_1/M$ where the $\{\mathbf{b}_i\}_{i=1}^m$ are from Equation (4.2.3) and M is the total number of nodes in the finite element mesh. This allows us to determine the dominant land cover classifications for each subdomain which are tabulated by percentage in Table 4.4 for the subdomain.

We choose the parameters to be the Manning's coefficients for the first four dominant land cover classifications and hold the Manning's coefficients constant for the remaining land cover classifications. We vary the Manning's coefficients between 33% and 175% of their original values based on tables available at [59]. The resulting 4 dimensional parameter domain is shown in Table 4.5 and the corresponding land cover classification meshes are shown in Figure 4.16.

4.4.2 Subdomain Data Space

We also must define the data space. Recall in Chapter 3 that we assume that the QoI are geometrically distinct. There might be multiple pairwise geometrically distinct QoI, however, the cardinality of a given set of geometrically distinct QoI is at most $d = n = 4$. In other words, the data space manifold

Percentage	C-CAP Class	Description	Manning's n
23.95	21	Open water	0.025
13.45	10	Evergreen forest	0.180
12.57	13	Palustrine forested wetland	0.150
12.33	4	Low-intensity developed	0.120
7.93	12	Scrub/shrub	0.080
7.07	18	Estuarine emergent wetland	0.050
4.97	5	Developed open space	0.035
4.19	14	Palustrine scrub/shrub wetland	0.075
3.70	7	Pasture/hay	0.050
3.41	8	Grassland	0.035
1.61	3	Medium-intensity developed	0.120
1.60	15	Palustrine emergent wetland	0.060
1.26	20	Bare land	0.030
0.78	2	High-intensity developed	0.120
0.46	6	Cultivated land	0.100
0.41	19	Unconsolidated shore	0.030
0.13	11	Mixed forest	0.170
0.12	17	Estuarine scrub/shrub wetland	0.070
0.01	23	Estuarine aquatic bed	0.030
0.01	9	Deciduous forest	0.160
0.00	22	Palustrine aquatic bed	0.035
0.00	16	Estuarine forested wetland	0.150

Table 4.4: Dominant land cover classifications for the subdomain.

Parameter	Range of Manning's n values	Land Classification
λ_1	[0.0396, 0.21]	4
λ_2	[0.0594, 0.315]	10
λ_3	[0.0495, 0.2625]	13
λ_4	[0.00825, 0.04375]	21

Table 4.5: Manning's n coefficient ranges for the subdomain.

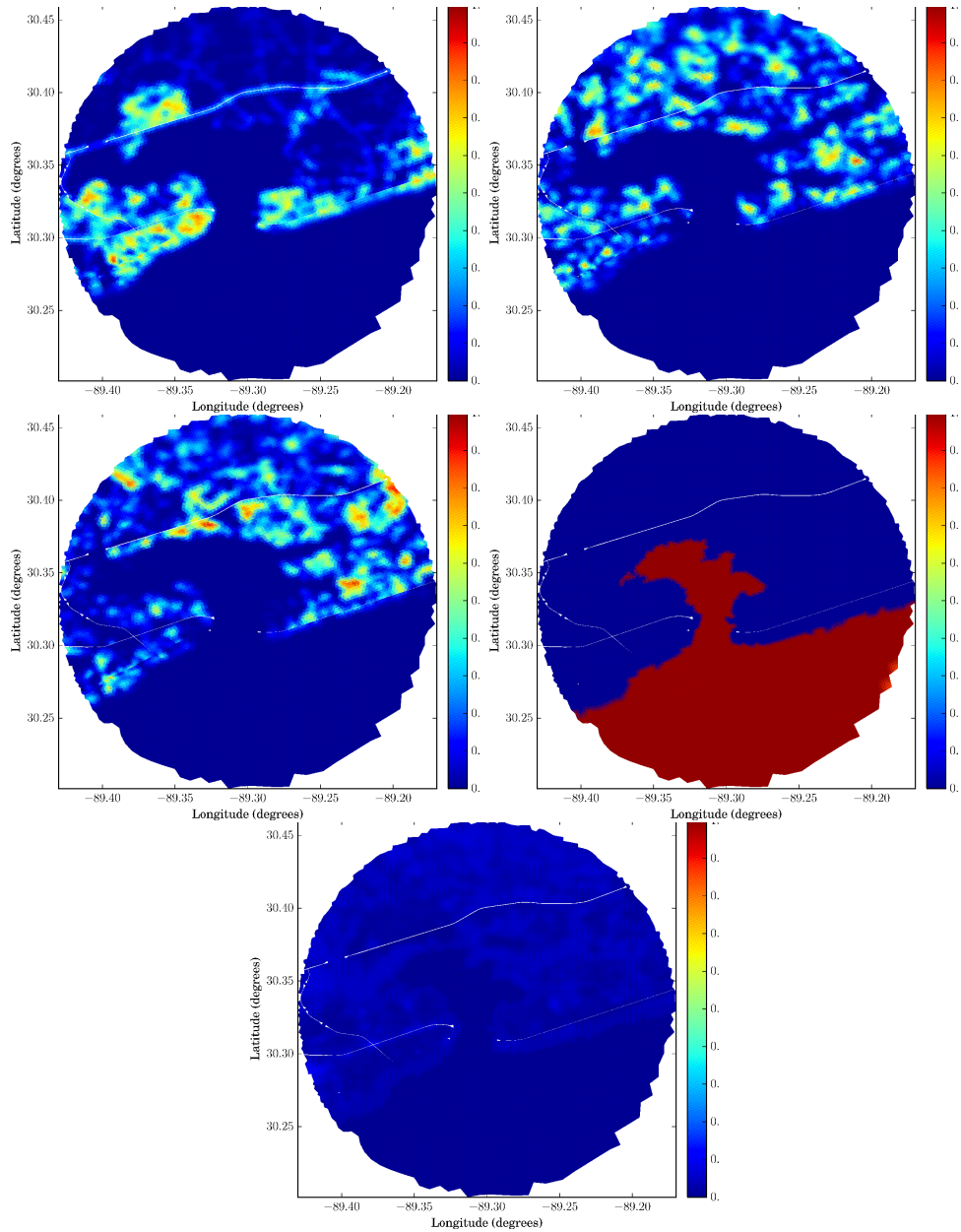


Figure 4.16: This shows the mesoscale representation of Manning's n values from basis vectors defining a linear mapping from land classification types for the subdomain. Top Left: Basis Vector 1. Top Right: Basis Vector 2. Middle Left: Basis Vector 3. Right Left: Basis Vector 4. Bottom: Basis Vector 5. Note the first four basis vectors correspond to $\lambda_1, \lambda_2, \lambda_3, \lambda_4$ while the fifth is held constant.

can only be of local dimension 4 or less. We examine maximum water elevation at a given set of observation stations in the physical domain. Given the difficulty of finding observation stations that result in a well-conditioned stochastic inverse problem we conduct a preliminary study of the subdomain to attain approximate gradient data using finite forward differences. We randomly select 16 points in the parameter space and approximate the gradient or Jacobian J_Q of Q with respect to λ . These clusters are shown in Figure 4.17 for the subdomain.

A full twenty-nine day hurricane subdomain simulation runs to completion on Stampede in approximately 5.5 hours on 2 processors (this time includes reconstructing and distributing the Manning's n mesh across the processors)³. If we were to examine every possible combination of maximum water elevation at every point in the finite element mesh we would have an infeasibly large set of options to examine. We interpolate the finite element solution onto a set of observation stations on a regular grid and then further reduce the problem size by limiting the set of possible observation stations to the set of stations exhibiting sensitivity to the parameters where the maximum change in maximum water elevation over the set of 80 forward model solves is greater than 0.10 [m]. Let $Y_i^{(k)} = Y_i(\lambda^{(k)})$ be the maximum water elevation at a particular station i for the k^{th} parameter value $\lambda^{(k)} = (\lambda_1^{(k)}, \lambda_2^{(k)}, \lambda_3^{(k)}, \lambda_4^{(k)})$ then the set of possible observation

³We used PolyADCIRC to simultaneously run a batch of 80 samples $\{\lambda^{(j)}\}_{j=1}^8$, $0 \in \Lambda$ on 160 processors.

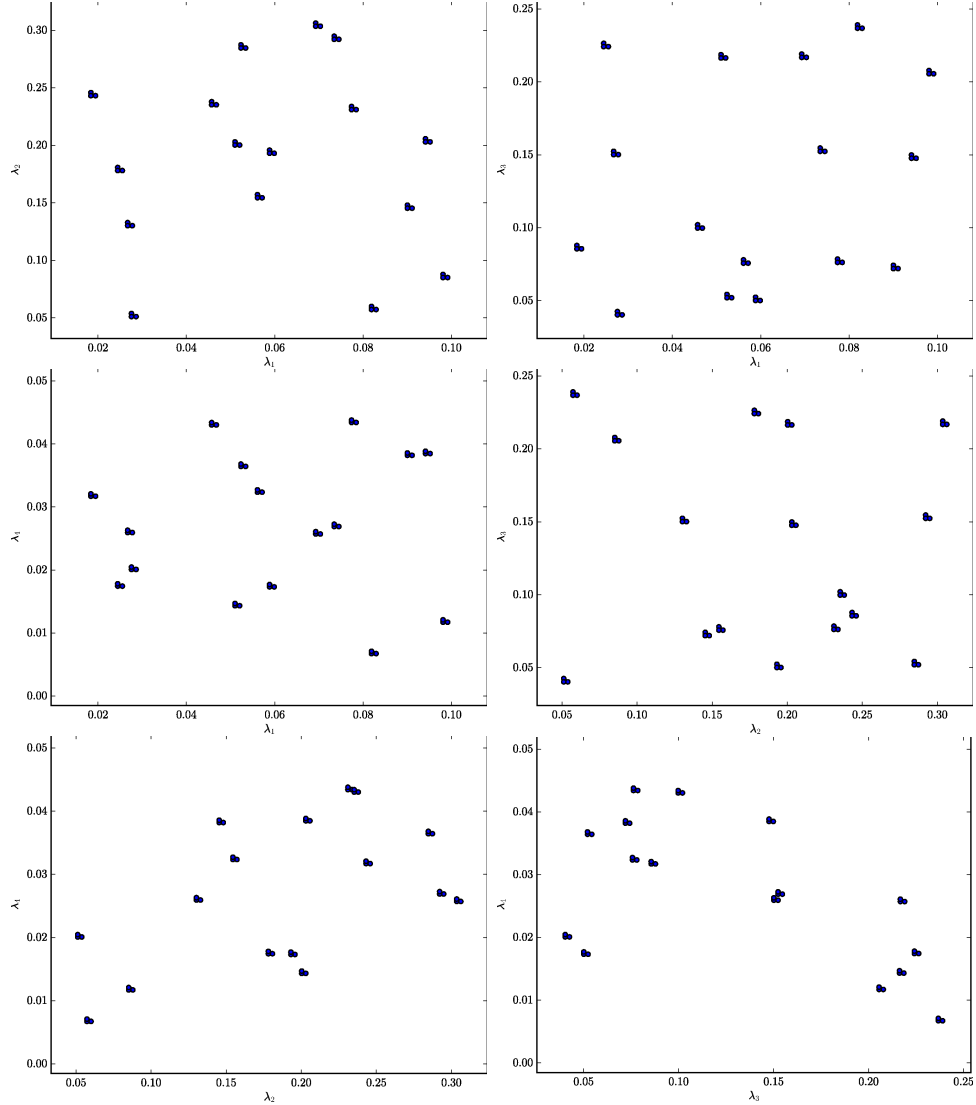


Figure 4.17: The 16 clusters in Λ used in the preliminary study of the subdomain, where $\lambda^{(k)} = (\lambda_1, \lambda_2, \lambda_3, \lambda_4)$. Left: In order from top to bottom $(\lambda_1, \lambda_2), (\lambda_1, \lambda_4), (\lambda_2, \lambda_4)$. Right: In order from top to bottom $(\lambda_1, \lambda_3), (\lambda_2, \lambda_3), (\lambda_3, \lambda_4)$.

	Number of Stations	Number of Data Spaces $\binom{n}{4}$
All	1970	$6.26 \cdot 10^{11}$
Reduced	194	$5.72 \cdot 10^7$

Table 4.6: Number of possible data spaces for the subdomain.

stations is $\left\{i : \max_i \left(\max_k (Y_i^{(k)}) - \min_k (Y_i^{(k)}) \right) > 0.10([m]) \right\}$ Figure 4.18 shows $\left(\max_k (Y_i^{(k)}) - \min_k (Y_i^{(k)}) \right)$ for the entire finite element mesh. Table 4.6 shows the number of possible data spaces for the original set of possible observation stations and the reduced set of observation stations.

To optimally choose QoI to result in a well-conditioned stochastic inverse problem with optimal skewness we use the `sensitivity` sub-package of BET developed by Scott Walsh at UC Denver [22]. Let $J_{i,j}^{(k)} = J_Q(\lambda^{(k)})$ where k is the k^{th} forward model evaluation and define the skew number $\hat{\kappa}$ for a given map $Q = (q_1, \dots, q_d)$ from the condition numbers of $J_Q(\lambda^{(k)})$ as

$$\hat{\kappa}(Q) = \frac{\left(\sum_{\{k: \kappa(J_Q(\lambda^{(k)})) < \infty\}} \kappa(J_Q(\lambda^{(k)})) \right) + 10^9 \cdot \#\{k : \kappa(J_Q(\lambda^{(k)})) = \infty\}}{K} \quad (4.4.1)$$

where K is the total number of k forward model solves. Table 4.7 show the condition number $\hat{\kappa}(Q)$ of the top 10 QoI maps. Figure 4.19 shows the location of the observation stations chosen by this a method. Note that these stations are well spaced in regions that appear to the eye to be rather hydraulically isolated. Since the stations in the first and last columns of Table 4.7 are nearly collocated it make intuitive sense that the skew numbers for the sets of stations show in Table 4.7 are nearly identical.

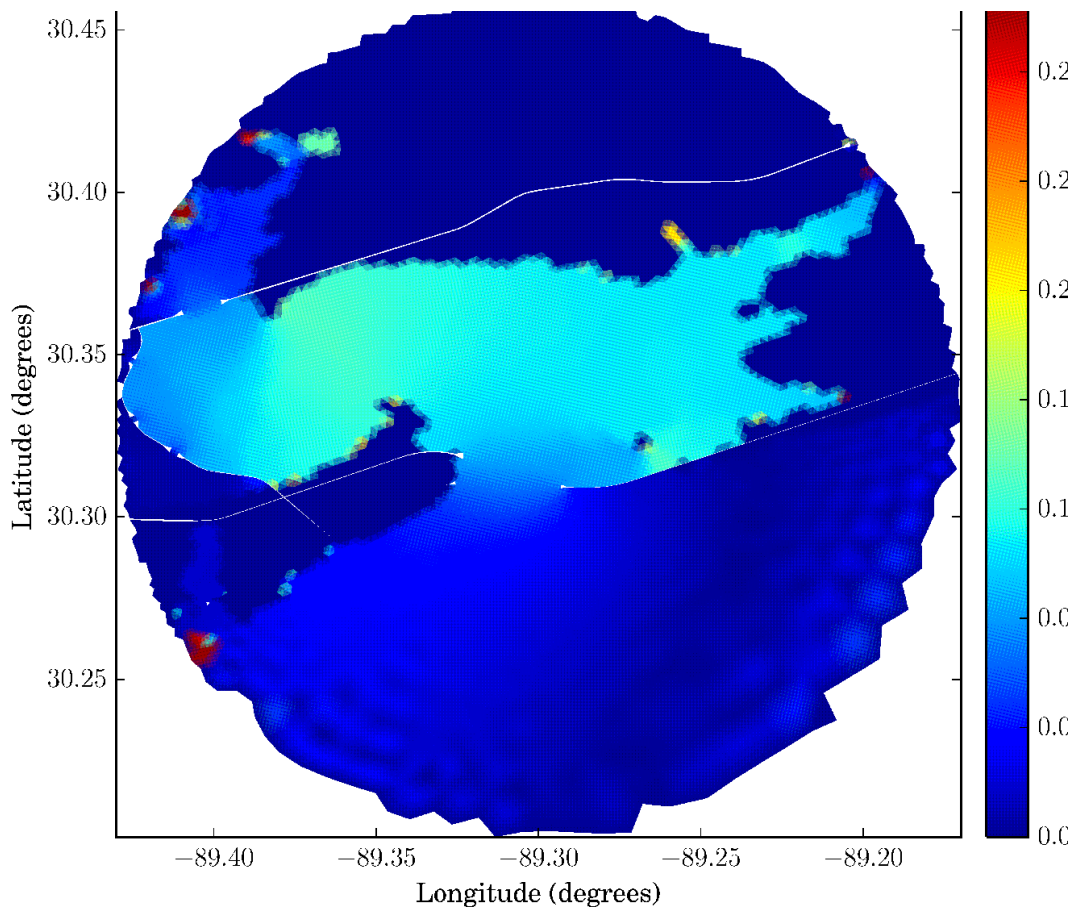


Figure 4.18: Maximum difference in subdomain water elevation over a set of 80 preliminary model evaluations. Values shown are $(\max_k(Y_i^{(k)}) - \min_k(Y_i^{(k)}))$ in $[m]$ where $Y_i^{(k)} = Y_i(\lambda^{(k)})$ is the maximum water elevation at a finite element node i for the k^{th} parameter value $\lambda^{(k)} = (\lambda_1^{(k)}, \lambda_2^{(k)}, \lambda_3^{(k)}, \lambda_4^{(k)})$. Note that to show subtle variations in the bay the color scale has been reduced.

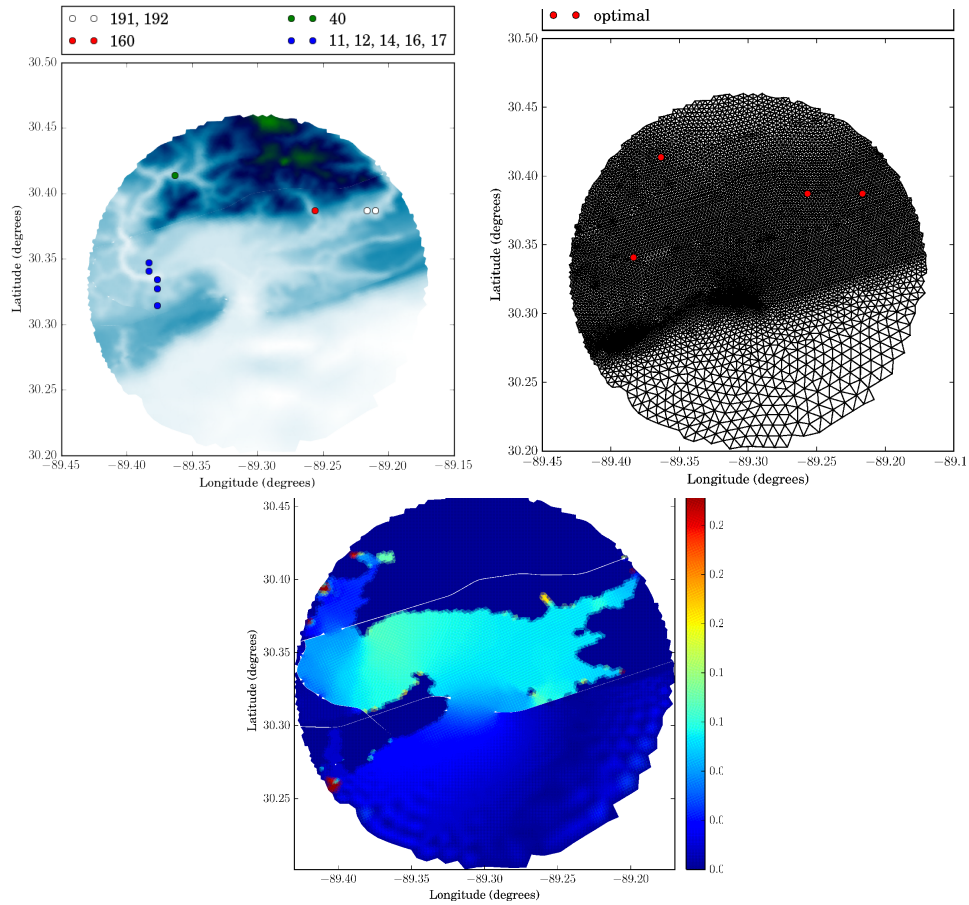


Figure 4.19: Left: Maximum water elevation observation stations with the top 10 QoI map skew numbers. Stations 11, 12, 14, 16, and 17 are shown in blue. Stations 191 and 192 are shown in white. Station 160 is shown in red. Finally, station 40 is shown in green. Right: Optimal maximum water elevation observation stations (11, 40, 160, 191). Bottom: Maximum difference in subdomain water elevation. See Figure 4.18.

Table 4.7: QoI map skew numbers for the subdomain.

$\hat{\kappa}(Q)$	Station Numbers
4.37e+02	11, 40, 160, 191
4.39e+02	12, 40, 160, 191
4.39e+02	11, 40, 160, 192
4.41e+02	17, 40, 160, 191
4.41e+02	12, 40, 160, 192
4.41e+02	10, 40, 160, 191
4.42e+02	14, 40, 160, 191
4.42e+02	16, 40, 160, 191
4.42e+02	17, 40, 160, 192
4.43e+02	16, 40, 160, 192

This choice of QoI maps should lead to a fullness of the convex hull formed by the 80 preliminary model evaluations at $\lambda^{(k)}$. For simplicity⁴ and visualization purposes we create a triangulation of $\lambda^{(k)}$ with $(\lambda_1, \lambda_2) \subset \mathbb{R}^2$ and use this triangularization to define the topological relation between points in \mathcal{D} in order to visualize $\mathcal{D} := \text{convhull}(Q(\lambda^{(k)}))$. We see a fair amount of fullness in \mathcal{D} in Figure 4.20 which shows the resulting data domain \mathcal{D} for the set of stations with the smallest skewness $\hat{\kappa}(Q)$ for the subdomain.

4.4.3 Subdomain Parameter Estimation for Bay St. Louis

We define and solve five stochastic inverse problems to quantify uncertainty in Manning's n values using five different QoI maps. We define $\rho_{\mathcal{D}}$ as a uniform distribution on a hyper-rectangle⁵ centered at $Q_{ref} = Q(\lambda_{ref})$

⁴It is difficult to visualize a 4 dimensional object.

⁵We choose the lengths of the sides to be 10% the length of q_i .

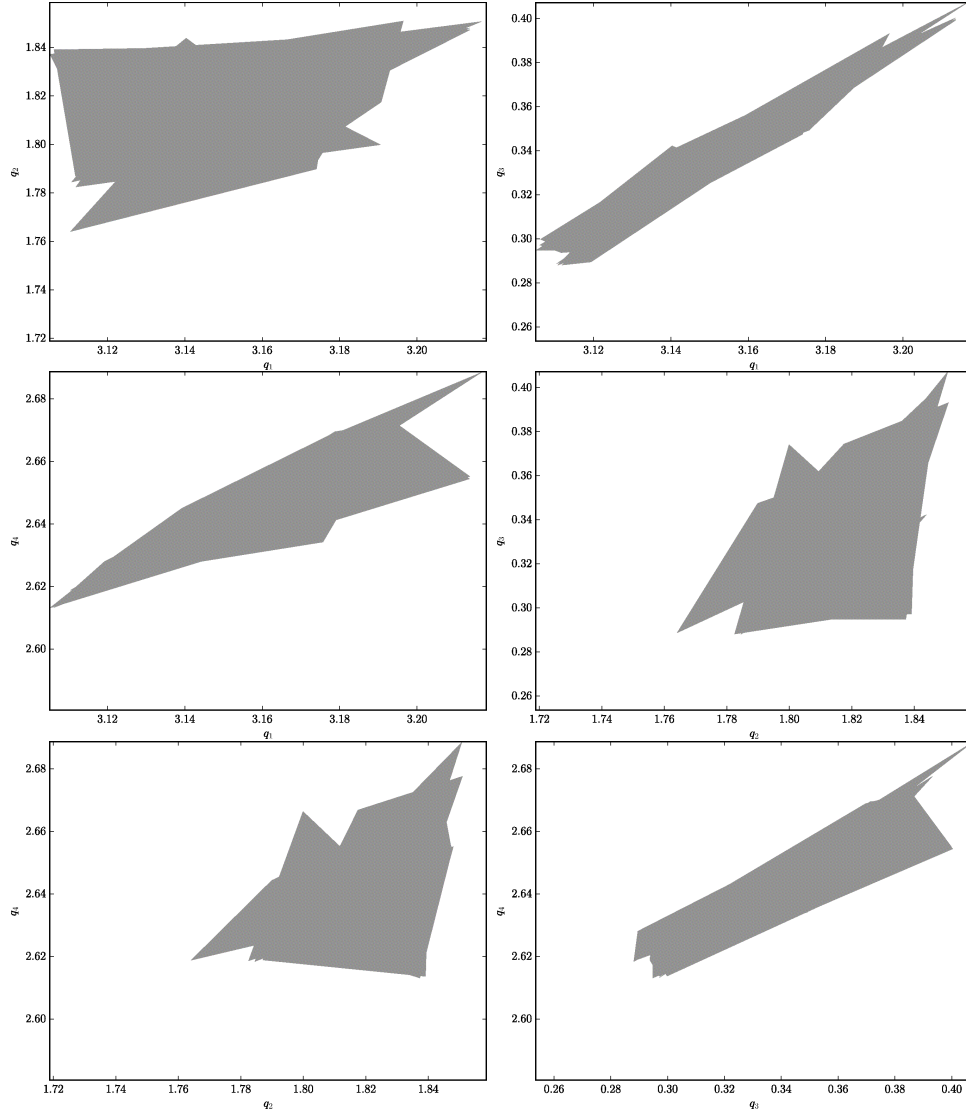


Figure 4.20: The data domain $\mathcal{D} = \text{convhull}(Q(\lambda^{(k)}))$ for the subdomain where $Q = (q_1, q_2, q_3, q_4)$ for stations 11, 40, 160, 191 respectively. Left: In order from top to bottom (q_1, q_2) , (q_1, q_4) , (q_2, q_4) . Right: In order from top to bottom (q_1, q_3) , (q_2, q_3) , (q_3, q_4) .

where $\lambda_{ref} = (0.1523, 0.1751, 0.1561, 0.0269)$. Since $\rho_{\mathcal{D}}$ is uniform on a hyper-rectangle we can exactly represent $\rho_{\mathcal{D}}$ with a simple function $\rho_{\mathcal{D},M}$ by choosing the partition $\{I_i\}$ carefully. We then follow the steps of Algorithms 1 and 2 in Section 3.2 and use 480 uniform i.i.d. random samples of Λ to estimate ρ_{Λ} .

We compare the results of the stochastic inverse problem for three QoI maps using optimal stations (11, 40, 160, 191), near optimal stations (16, 40, 160, 192), and non-optimal stations (16, 40, 22, 88). The skew numbers of the QoI maps for the optimal and near optimal sets of stations are very similar (see Table 4.7). Figure 4.21 show the 480 uniform i.i.d. random samples with respect to μ_{Λ} in the parameter space. Figures 4.22 and 4.23 shows the propagation of these samples in the data spaces for the optimal and non-optimal QoI maps respectively colored by $\rho_{\mathcal{D}}(Q(\lambda))$. We omit the data samples of the near optimal QoI map as they are visually indistinguishable from those of the optimal QoI map.

Figures 4.24 to 4.26 show the resulting approximate marginals of ρ_{Λ} for the stochastic inverse problem using the optimal, near optimal, and non-optimal stations respectively. We use 10^6 emulated samples in Algorithm 2 to approximate the volumes of the Voronoi cells. We use kernel density estimation to smooth the resulting density approximation. Let $\text{supp}(\rho_{\mathcal{D}}) = E \in \mathcal{B}_{\mathcal{D}}$, and the corresponding contour event $Q^{-1}(E) \in \mathcal{B}_{\Lambda}$. For the optimal and near optimal sets of stations, $\mu_{\Lambda}(Q^{-1}(E))$ is small; and the probability measure P_{Λ} is nearly identical for both. The corresponding estimates of the volumes of the contour events $\mu_{\Lambda}(Q^{-1}(E))$ are 7.904e-3 and 8.390e-3 for the optimal and

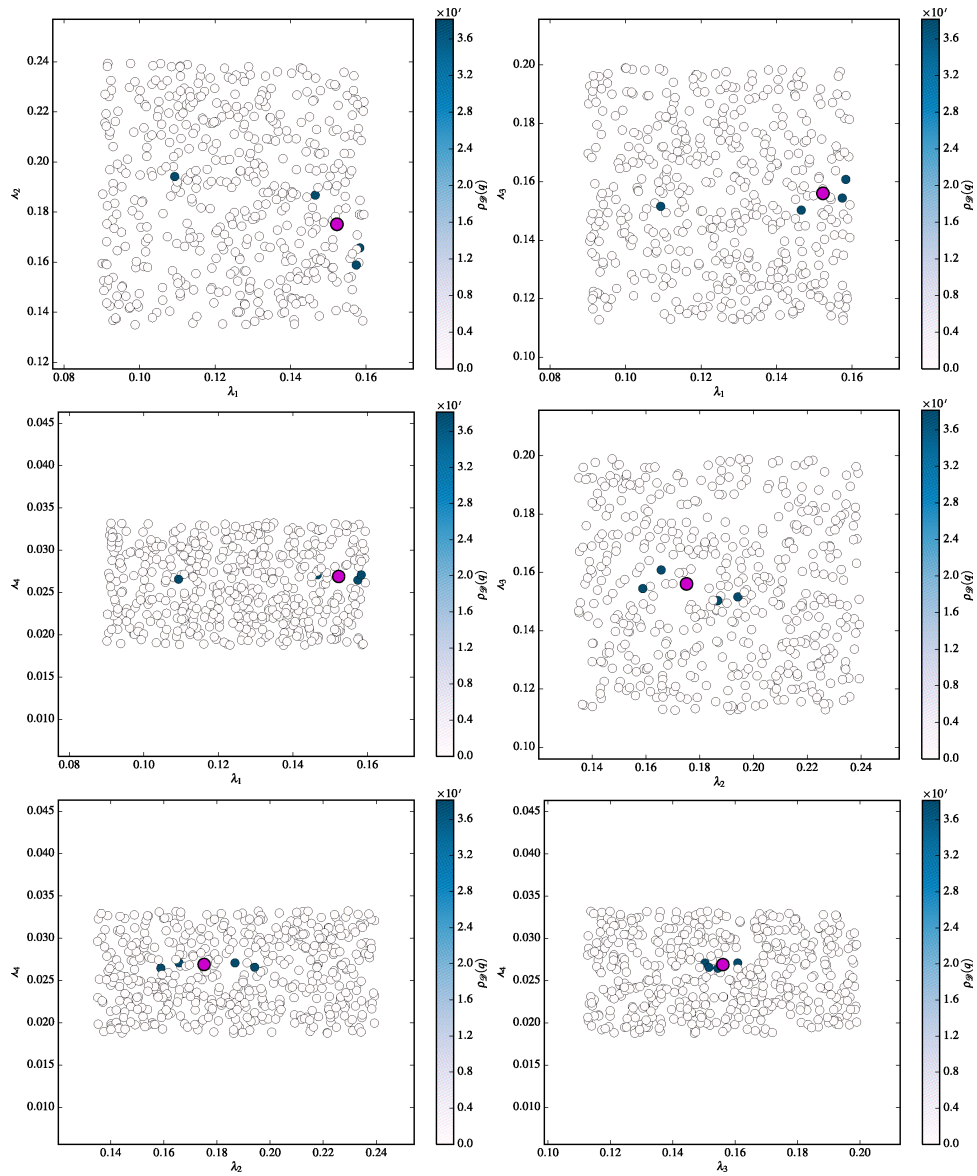


Figure 4.21: The uniform samples in the parameter space for the subdomain where $\lambda = (\lambda_1, \lambda_2, \lambda_3, \lambda_4)$ and $\lambda_{ref} = (0.1523, 0.1751, 0.1561, 0.0269)$ is marked in magenta. The samples are colored by $\rho_{\mathcal{D}}(Q)$. Left: In order from top to bottom (λ_1, λ_2) , (λ_1, λ_4) , (λ_2, λ_4) . Right: In order from top to bottom (λ_1, λ_3) , (λ_2, λ_3) , (λ_3, λ_4) .

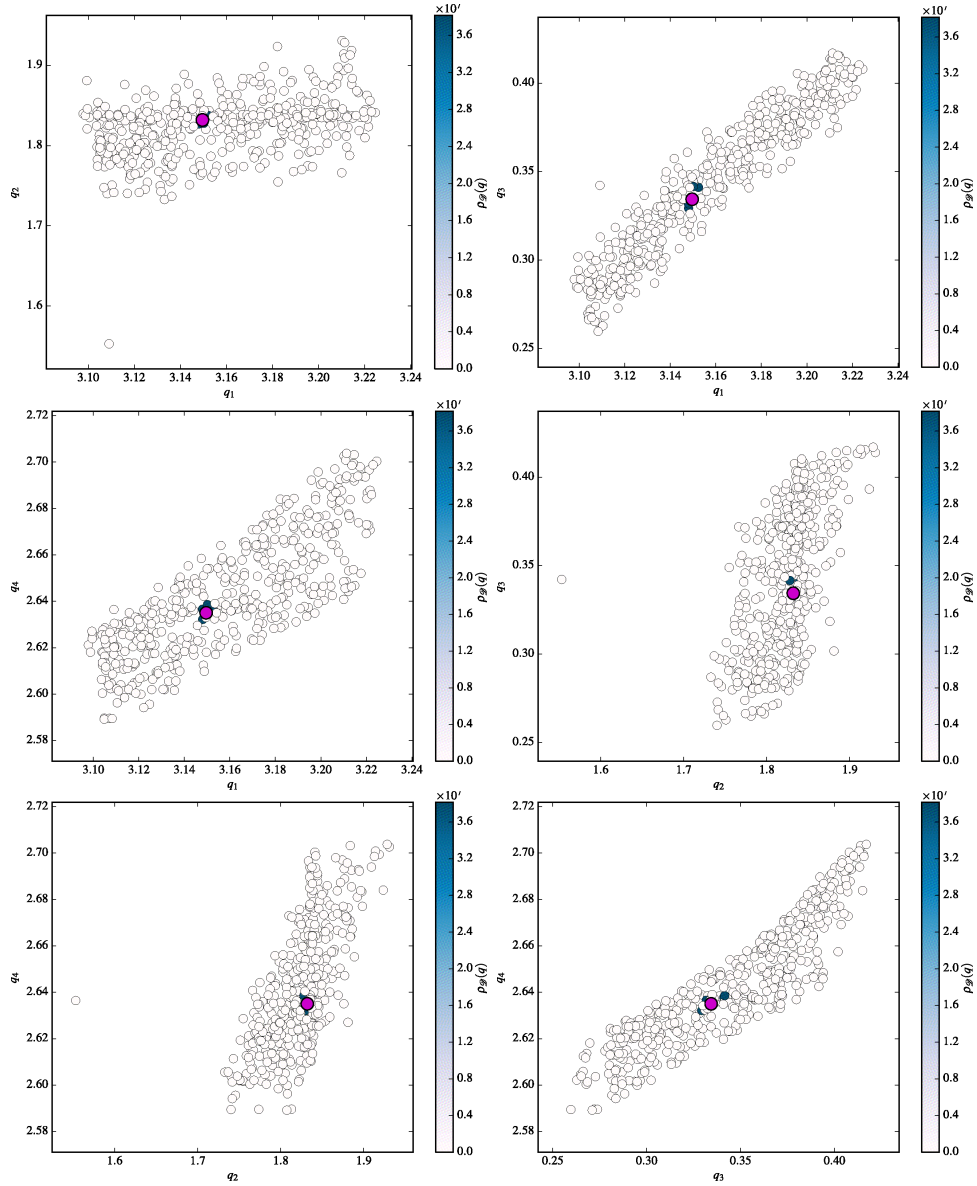


Figure 4.22: The propagation of uniform samples in the parameter space for the subdomain for optimal stations 11, 40, 160, 191 where $Q = (q_1, q_2, q_3, q_4)$ and Q_{ref} is marked in magenta. The samples are colored by $\rho_{\mathcal{D}}(Q)$. Left: In order from top to bottom (q_1, q_2) , (q_1, q_4) , (q_2, q_4) . Right: In order from top to bottom (q_1, q_3) , (q_2, q_3) , (q_3, q_4) .

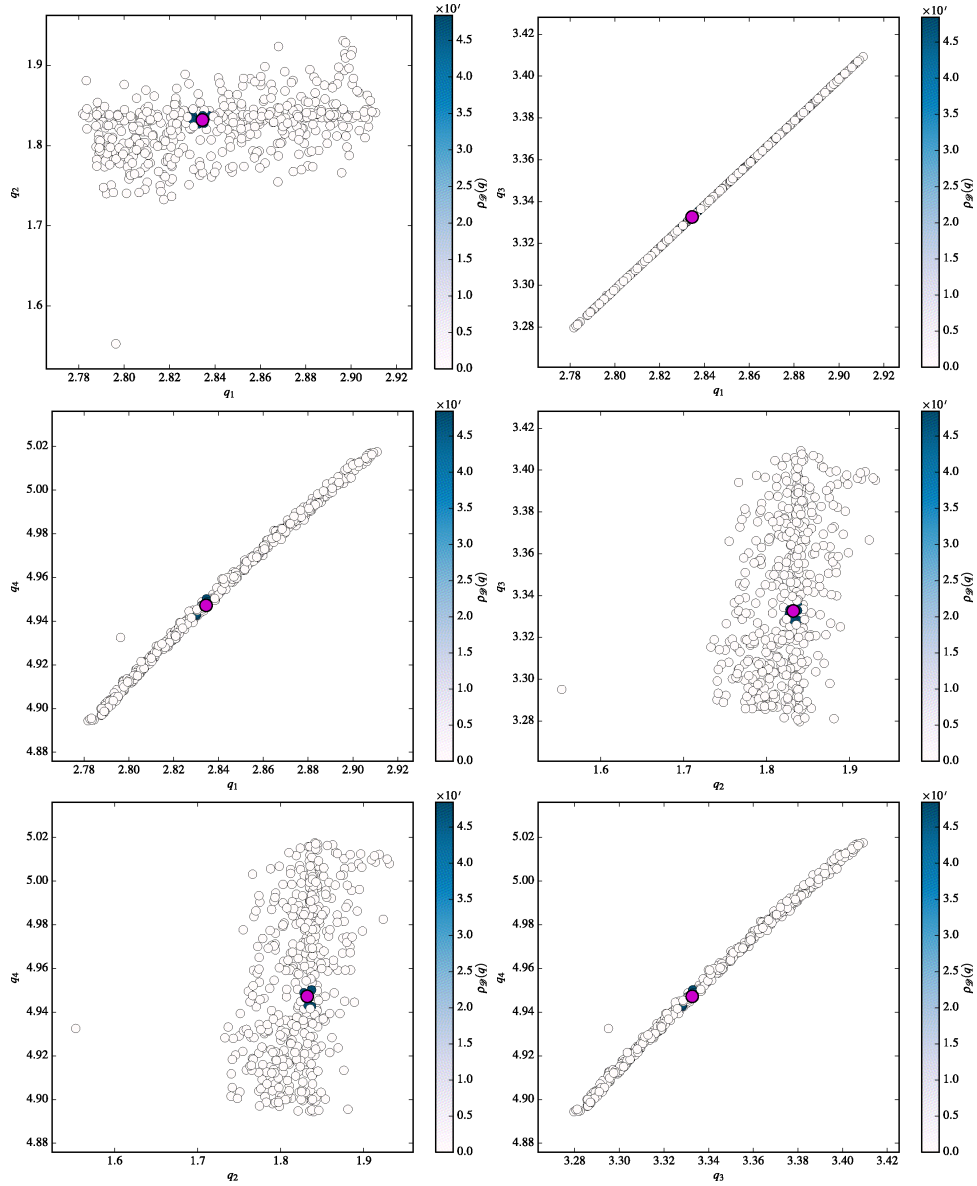


Figure 4.23: The uniform samples in the data space for the subdomain for suboptimal stations 16, 40, 22, 88 where $Q = (q_1, q_2, q_3, q_4)$ and Q_{ref} is marked in magenta. The samples are colored by $\rho_{\mathcal{D}}(Q)$. Left: In order from top to bottom (q_1, q_2) , (q_1, q_4) , (q_2, q_4) . Right: In order from top to bottom (q_1, q_3) , (q_2, q_3) , (q_3, q_4) .

near optimal sets of stations respectively. Notice that even though we have the most difficulty in identifying λ_3 the region of non-zero probability still contains the reference parameter.

However, the non-optimal QoI map (stations 16, 40, 22, 88) identifies $Q^{-1}(E)$ a larger event in the parameter space as shown in Figure 4.26. Figure 4.23 shows that the QoI map formed from the non-optimal set of stations is highly skewed in comparison to the QoI maps formed from the optimal and near optimal sets of stations. The estimated volume of the region of interest for the non-optimal QoI map $\mu_{\Lambda}(Q^{-1}(E)) = 1.917\text{e-}2$ is about 250% greater than that of $\mu_{\Lambda}(Q^{-1}(E))$ where Q is formed from an optimal or near optimal set of stations. We can examine the marginals that result if we only use a subset of the non-optimal stations [16, 40, 22] in Figure 4.27 and [16, 40] in Figure 4.28. The marginals in Figures 4.27 and 4.28 do not appear substantially different than the marginals shown in Figure 4.26 further emphasizing that QoI maps with large skew may not improve the solution to the stochastic inverse problem computed from fewer QoI with smaller skew. In other words, QoI maps with high skew in their components have solutions to the stochastic inverse problem that are similar to solutions from a QoI map with fewer component maps.

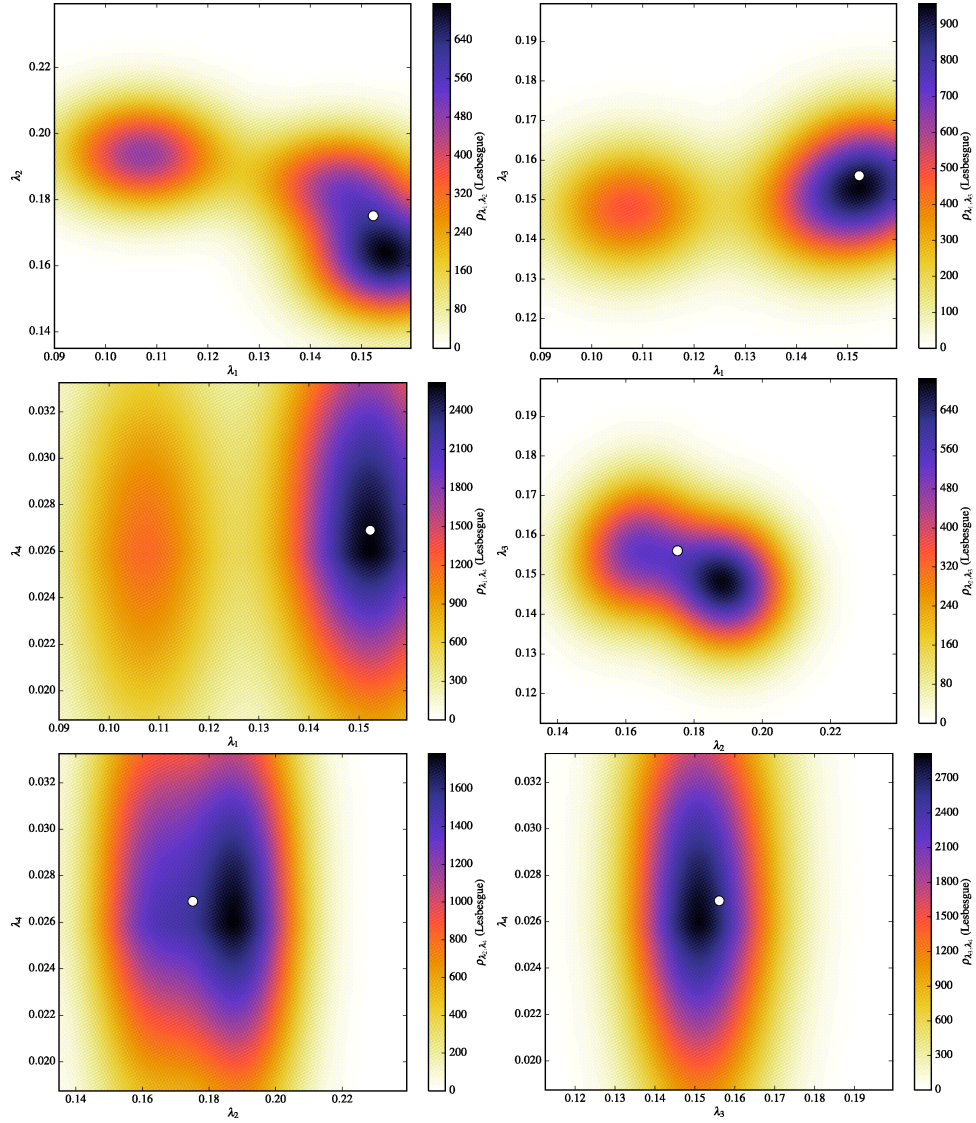


Figure 4.24: Plots of the marginals of ρ_Λ using uniform samples for optimal stations 11, 40, 160, 191 . Here, $\rho_{\mathcal{D}}$ is defined as a uniform density on a small rectangular box centered at the reference QoI values associated with $\lambda_{ref} = (0.1523, 0.1751, 0.1561, 0.0269)$. The reference value is illustrated by a white circle. Left: In order from top to bottom $(\lambda_1, \lambda_2), (\lambda_1, \lambda_4), (\lambda_2, \lambda_4)$. Right: In order from top to bottom $(\lambda_1, \lambda_3), (\lambda_2, \lambda_3), (\lambda_3, \lambda_4)$.

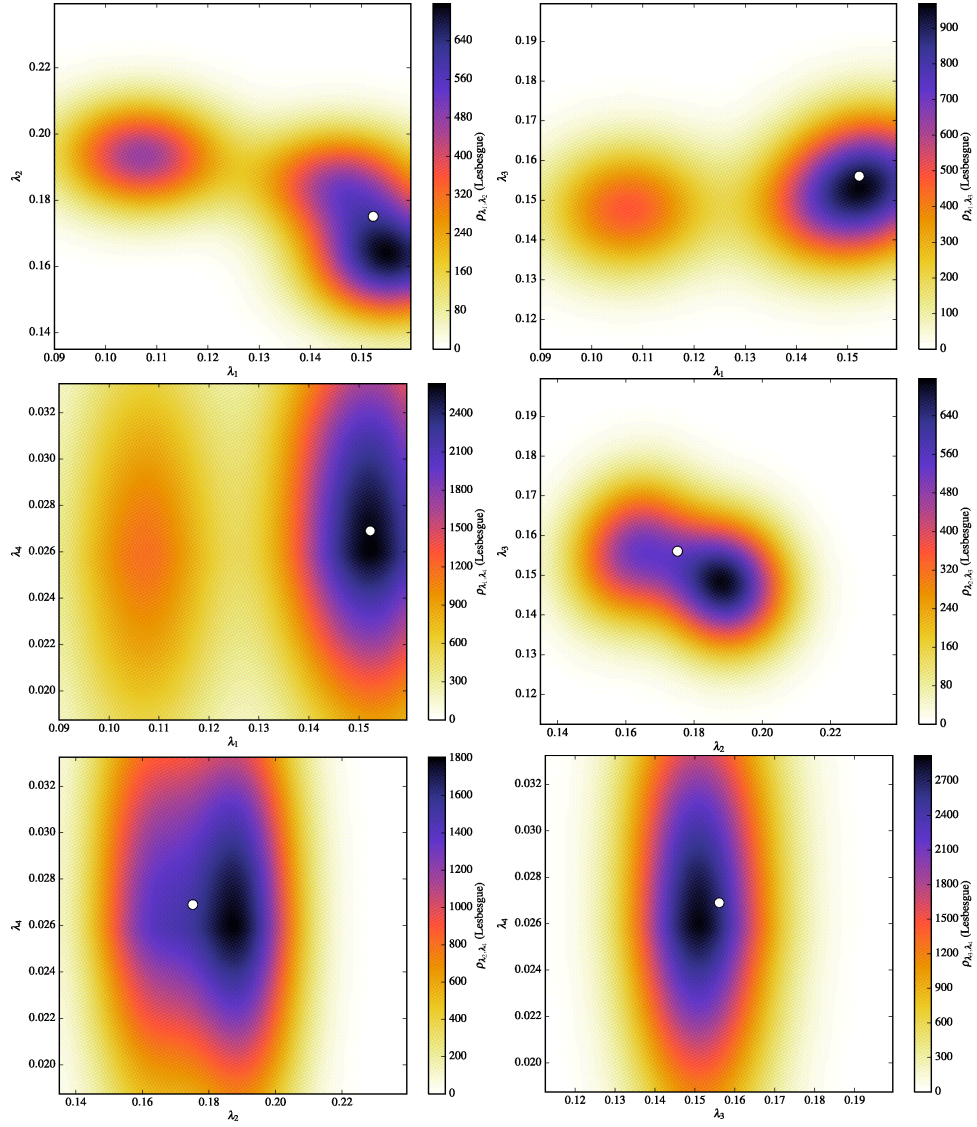


Figure 4.25: Plots of the marginals of ρ_{Λ} using uniform samples for near optimal stations 16, 40, 160, 192 . Here, $\rho_{\mathcal{D}}$ is defined as a uniform density on a small rectangular box centered at the reference QoI values associated with $\lambda_{ref} = (0.1523, 0.1751, 0.1561, 0.0269)$. The reference value is illustrated by a white circle. Left: In order from top to bottom (λ_1, λ_2) , (λ_1, λ_4) , (λ_2, λ_4) . Right: In order from top to bottom (λ_1, λ_3) , (λ_2, λ_3) , (λ_3, λ_4) .

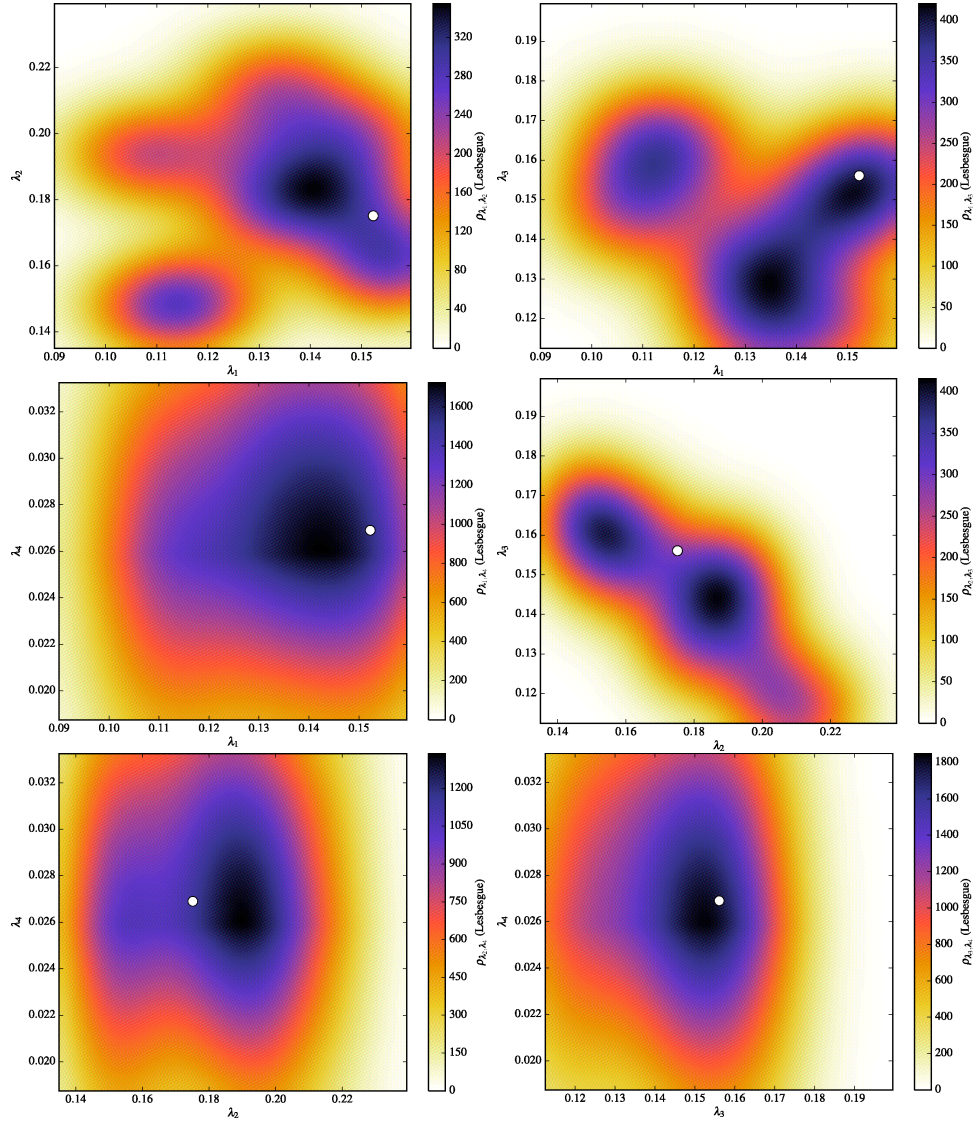


Figure 4.26: Plots of the marginals of ρ_Λ using uniform samples for suboptimal stations 16, 40, 22, 88 . Here, $\rho_{\mathcal{D}}$ is defined as a uniform density on a small rectangular box centered at the reference QoI values associated with $\lambda_{ref} = (0.1523, 0.1751, 0.1561, 0.0269)$. The reference value is illustrated by a white circle. Left: In order from top to bottom $(\lambda_1, \lambda_2), (\lambda_1, \lambda_4), (\lambda_2, \lambda_4)$. Right: In order from top to bottom $(\lambda_1, \lambda_3), (\lambda_2, \lambda_3), (\lambda_3, \lambda_4)$.

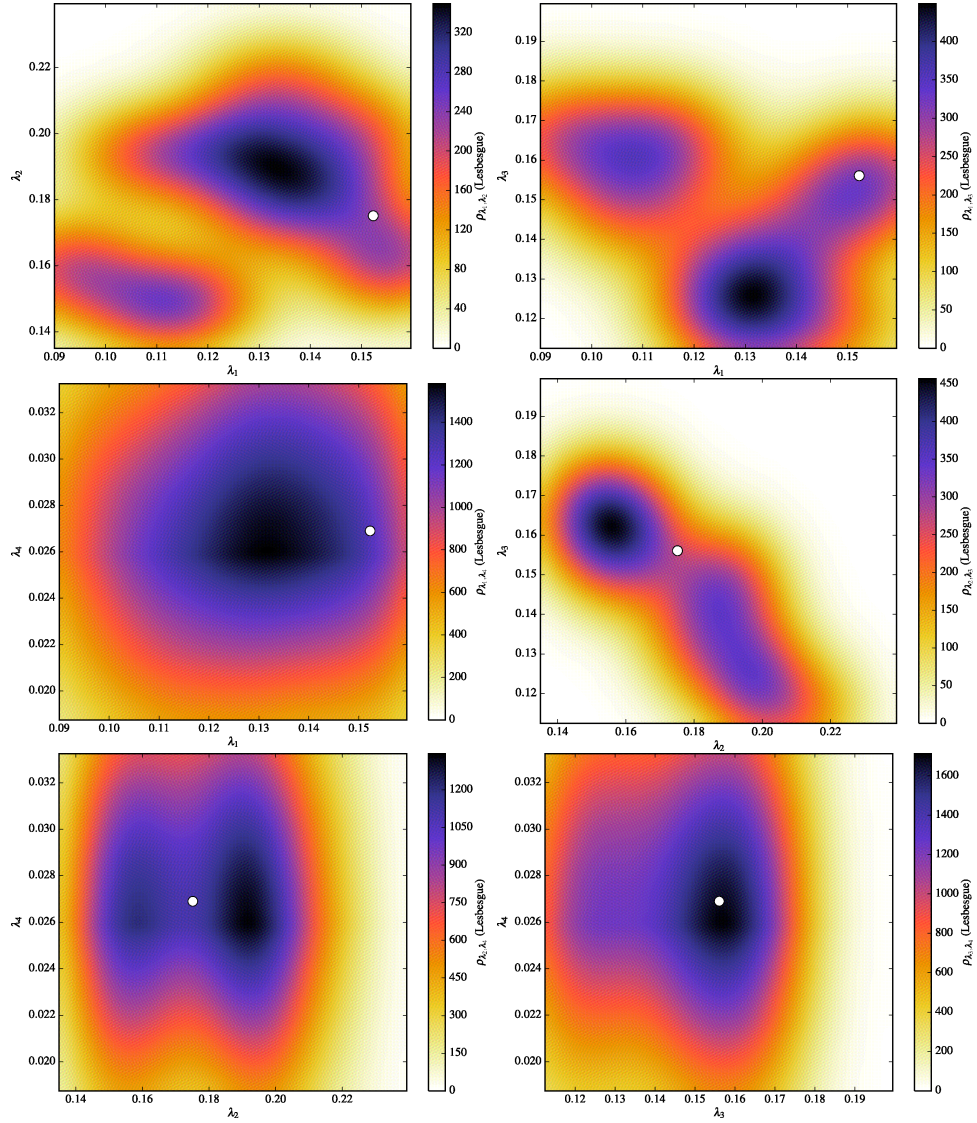


Figure 4.27: Plots of the marginals of ρ_Λ using uniform samples for stations 16, 40, 22. Here, $\rho_{\mathcal{D}}$ is defined as a uniform density on a small rectangular box centered at the reference QoI values associated with $\lambda_{ref} = (0.1523, 0.1751, 0.1561, 0.0269)$. The reference value is illustrated by a white circle. Left: In order from top to bottom (λ_1, λ_2) , (λ_1, λ_4) , (λ_2, λ_4) . Right: In order from top to bottom (λ_1, λ_3) , (λ_2, λ_3) , (λ_3, λ_4) .

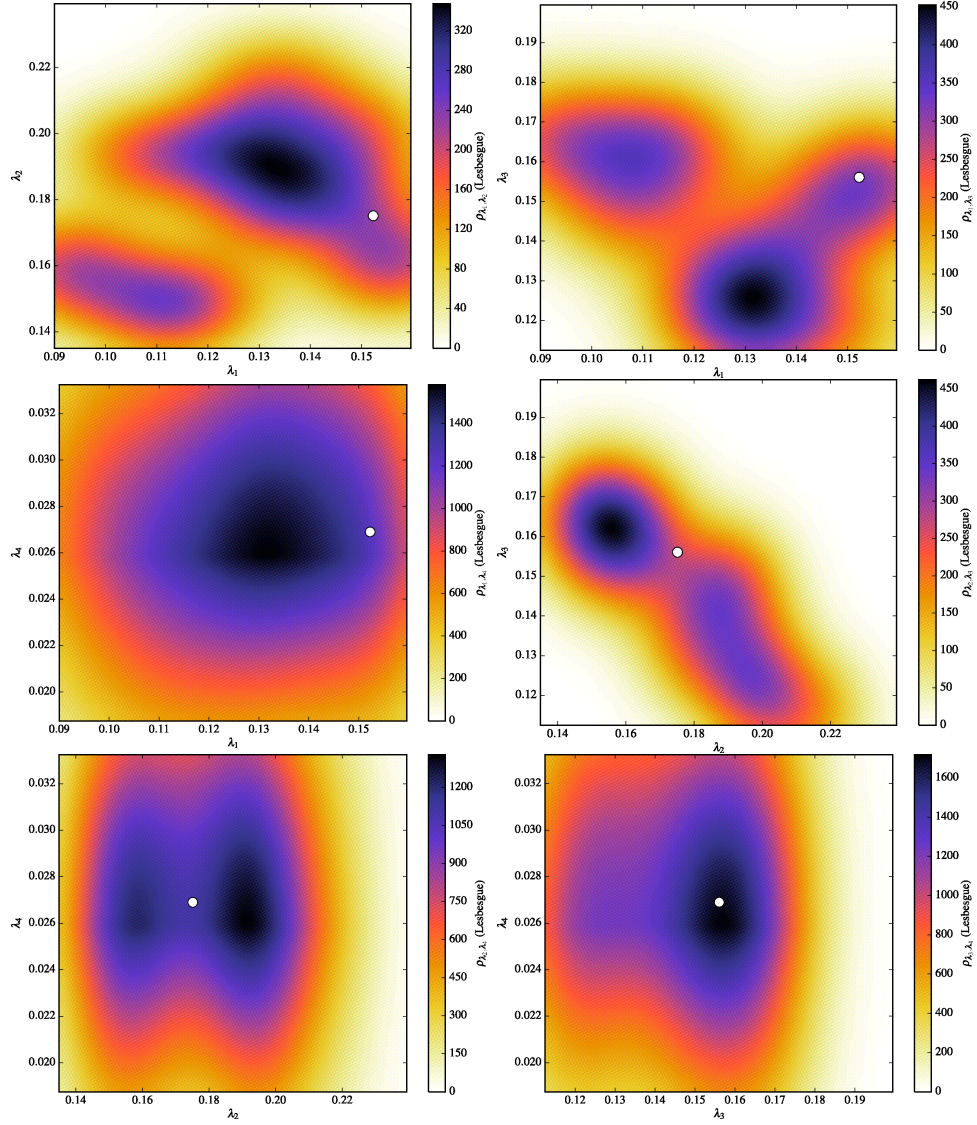


Figure 4.28: Plots of the marginals of ρ_Λ using uniform samples for stations 16, 40. Here, $\rho_{\mathcal{D}}$ is defined as a uniform density on a small rectangular box centered at the reference QoI values associated with $\lambda_{ref} = (0.1523, 0.1751, 0.1561, 0.0269)$. The reference value is illustrated by a white circle. Left: In order from top to bottom (λ_1, λ_2) , (λ_1, λ_4) , (λ_2, λ_4) . Right: In order from top to bottom (λ_1, λ_3) , (λ_2, λ_3) , (λ_3, λ_4) .

Chapter 5

Goal-Oriented Adaptive Sampling

The goal in Chapter 3 was to compute the probability (or volume) of arbitrary events $A \in \mathcal{B}_\Lambda$. Often, we are only interested in a few particular events $A \in \mathcal{B}_\Lambda$. If we wish to perform parameter estimation these sets are typically the regions of generalized contours of highest probability. However, we may choose to focus on the identification and quantification of uncertainty of other regions defined implicitly in the parameter space by important events in the data space (e.g., low probability failure thresholds, events defined by conditions on $\rho_{\mathcal{D}}$, or other “rare” events [56]). In Chapter 4 the goal was to determine inverse regions of high probability accurately which requires approximating volumes of sets in high probability areas of Λ . We accomplished this by using a regular grid of points in Λ . However, the use of finer regular grids is impractical in high dimensions due to the “curse of dimensionality”. Furthermore, it becomes more difficult to locate high probability regions in higher dimensions as the volumes of high probability regions decreases as the dimension of the probability space increases [60]. As such we do not expect any significant improvement through the use of uniform sampling. Uniform sampling converges to the true solution in probability with the same convergence rate as Monte Carlo integration, $\mathcal{O}(1/N)$. Uniform samples allow too many

samples to be placed in regions of zero or low probability¹. We do not need to accurately estimate the volume of such regions. If we only want to approximate $P_\Lambda(Q^{-1}(E))$ we only need to approximate the event $A = Q^{-1}(E) \subset \mathcal{B}_\Lambda$ for $E \cap \text{supp}(\rho_{\mathcal{D}}) \subset \mathcal{B}_{\mathcal{D}}$.

Goal-oriented adaptive sampling focuses on generating a set of samples $\{\lambda^{(j)}\}$ that implicitly define a Voronoi tessellation of Λ that is useful for approximating a particular event $A \in \mathcal{B}_\Lambda$ where the event A is implicitly defined by an event $E \subset \mathcal{B}_{\mathcal{D}}$.

Definition 5.0.1. Given a Voronoi tessellation of Λ denoted by $\{\mathcal{V}_j\}_{j=1}^N \subset \Lambda$ we say that A_N is the **Voronoi coverage** of $A \in \mathcal{B}_\Lambda$ and $\mu_k(A)$ is its volume defined by

$$A_N := \bigcup_{\lambda^{(j)} \in A, 1 \leq j \leq N} \mathcal{V}_j, \text{ and } \mu_k(A) := \mu_\Lambda(A_k) = \sum_{j=1}^N \mu_\Lambda(\mathcal{V}_j) \mathbf{1}_{\lambda^{(j)} \in A} \quad (5.0.1)$$

[19].

Definition 5.0.2. A rule for defining any N samples $\{\lambda^{(j)}\}_{j=1}^N \subset \Lambda$ is called **\mathcal{B}_Λ -consistent** if

$$\mu_\Lambda(A \Delta A_k) \rightarrow 0 \text{ as } N \rightarrow \infty, \forall A \in \mathcal{B}_\Lambda, \text{ s.t. } \mu_\Lambda(\partial A) = 0. \quad (5.0.2)$$

where Δ is the symmetric difference [19].

In other words, if $\partial A_N \rightarrow \partial A$ as $N \rightarrow \infty$ then we have a \mathcal{B}_Λ -consistent sampling scheme. It has been previously shown in [19] that if we generate

¹This also applies to uniform i.i.d. random samples.

$\{\mathcal{V}_j\}_{j=1}^N$ with a \mathcal{B}_Λ -consistent scheme and we have a probability measure $P_{\mathcal{D}} \ll \mu_{\mathcal{D}}$ on $(\mathcal{D}, \mathcal{B}_\Lambda)$ then for any event $A \in \mathcal{B}_\Lambda$, there exists $\rho_{\mathcal{D},M}$ and $\tilde{P}_{\Lambda,N}$, such that $\tilde{P}_{\Lambda,N}(A) \rightarrow P_\Lambda(A)$ as $N, M \rightarrow \infty$ [19]. We refer the interested reader to [19] for an in-depth theoretical discussion and proof of the aforementioned theorem.

If we let $\rho_{\mathcal{D}} = \mathbf{1}_E$ for some region of interest (RoI) $E \subset \mathcal{B}_{\mathcal{D}}$ then the goal is to approximate the set $Q^{-1}(E) \subset \mathcal{B}_\Lambda$. The swiftness of convergence is then controlled by two factors (1) locating the region of interest $Q^{-1}(E) \subset \mathcal{B}_\Lambda$ and (2) approximating the boundary of the RoI by placing samples so that the edges of the Voronoi cells they form approximate ∂A . The more samples we place near ∂A the better we can approximate ∂A . If we focus on placing more samples in A we will be able to better approximate both ∂A and $\rho_\Lambda(\lambda)$ for $\lambda \in A$. We will address the second concern with a probability based adaptive sampler in Section 5.1. The first concern might be addressed using a gradient based adaptive sampler.

5.1 Probability Based Adaptive Sampling

We use a goal-oriented probabilistic adaptive sampling algorithm (see Algorithm 3) to focus on placing more samples in regions of high probability and accurately approximate the volumes of the high probability regions in Λ implicitly defined by the probability measure on the data space $P_{\mathcal{D}}$ (or $\rho_{\mathcal{D}}$). We assume we know $\rho_{\mathcal{D}}$. We use Algorithm 2 to account for non-uniform samples from Algorithm 3 by estimating (or calculating) the volume of the Voronoi

cells. Algorithm 3 generates samples according to a transition probability kernel $P_t(\lambda, B(s))$. From [19] we know that any random sampling scheme with sampling density $f(\lambda) > 0$ produces a \mathcal{B}_Λ -consistent rule which implies that Algorithm 3 generates \mathcal{B}_Λ -consistent samples. Thus, Algorithm 3 generates \mathcal{B}_Λ -consistent samples².

5.2 Probability Based Adaptive Sampling Results

We compare the approximation of $\rho_{\mathcal{D}}$ using 121^2 samples on a regular grid from the idealized inlet case study in Section 4.3.1 to an approximation where samples are obtained using Algorithm 3. For the adaptive sampling, we let the number of chains $M = 80$, chain length $N = 125$, and set the $B(s)$ to be $R(s) \cap \Lambda$ where the $R(s)$ are rectangles similar to Λ centered at previous samples and scaled by parameter \mathbf{s} . The adaptive samples are shown in Figure 5.1. We adaptively generate a total of $1E4$ samples, 4703 of which are in regions of high probability compared to $670/14641$ for the regular grid of samples (see Figure 5.2). In both cases, we correctly identify a region of high probability in parameter space containing the true parameter value. This adaptive sampling algorithm seems promising as the results using the adaptive samples produce a comparable approximation to P_Λ in the region of interest by placing $\mathcal{O}(10)$ more samples in the RoI than samples on regular. Once the RoI is located this performance gain continues to increase as the number of

²The total number of samples $\{\lambda^{(i,j)}\}_{i,j}$ is $N \times M$

samples increases as shown in Section 5.3.

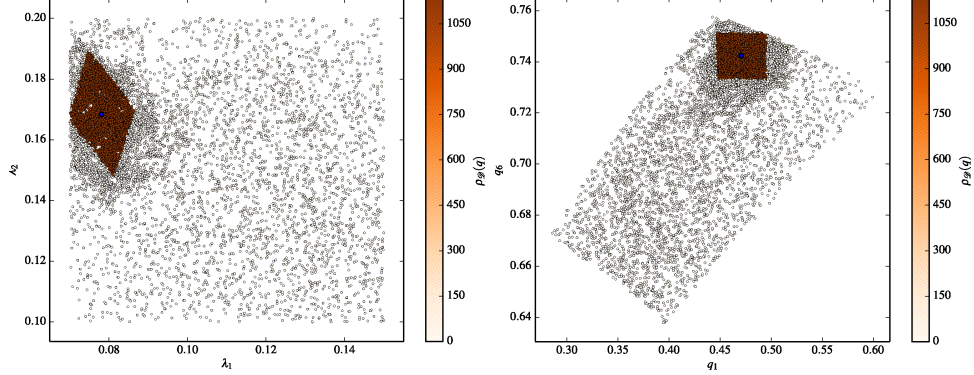


Figure 5.1: The samples used to approximate ρ_{Λ} for the idealized inlet for $Q = (q_1, q_6)$ where $\lambda_{true} = (\lambda_1, \lambda_2) = (0.0781, 0.168)$ using Algorithm 3. Left: The samples $\lambda^{(j)} \in \Lambda$. Right: The corresponding data $Q(\lambda^{(j)}) \in \mathcal{D}$.

We can easily modify this algorithm to target particular RoI in the parameter space. We assume that these areas are all defined implicitly by a specification in the data space. We could specify RoI by choosing D_k and $p_k = \mathbf{1}_{D_k}$ to uniformly prioritize certain regions of generalized contours or define p_k to prioritize certain regions more than others. The current specification of p_k is simply the definition of a simple function approximation of $\rho_{\mathcal{D}}$ on the partition D_k . Altering the choice of D_k will alter how well we represent $P_{\mathcal{D}}$ and correspondingly how well we resolve P_{Λ} . The current implementation of the algorithm only generates a preset number of samples. However, we could continue to sample Λ until each $Q^{-1}(D_k)$ contains a minimum number of samples or we have sampled a preset maximum number of samples.

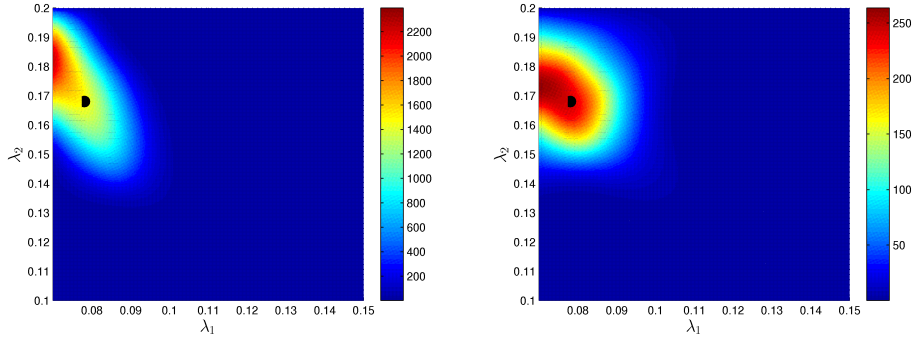


Figure 5.2: The approximation of ρ_Λ for the idealized inlet for $Q = (q_1, q_6)$ where $\lambda_{true} = (\lambda_1, \lambda_2) = (0.0781, 0.168)$. Left: The approximation of ρ_Λ using a regular grid of 121^2 samples in Algorithm 1. Right: The approximation of ρ_Λ using the adaptive sampling Algorithm 3.

5.3 Convergence of Adaptive Sampling

We can use Algorithm 1 to estimate the volume of an implicitly defined region of interest in $Q^{-1}(E) \subset \mathcal{B}_\Lambda$ for some $E \subset \mathcal{B}_\mathcal{D}$. We use the surrogate model developed from the idealized inlet case study in Section 4.3 to compare the convergence of various sampling strategies. Since the dimension is small we can exactly represent $\rho_\mathcal{D}$ with a simple function approximation and exactly calculate $\mu_\Lambda(Q^{-1}(E))$. We do this so that all of the error in the approximation of $\mu_\Lambda(Q^{-1}(E))$ is due to error in the approximation of $Q^{-1}(E) \subset \mathcal{B}_\Lambda$ which is the error that adaptive sampling aims to reduce. Recall that the convergence of any \mathcal{B}_Λ -**consistent** sampling rule is controlled by (1) locating the region of interest and (2) approximating the boundary of the region of interest. This has several implications. The better conditioned the stochastic inverse problem, the smaller the support of the implicitly defined RoI and thus $Q^{-1}(E) \subset \mathcal{B}_\Lambda$

is more difficult to approximate and locate.

To compare the performance of uniform sampling without volume emulation, uniform sampling with volume emulation (Algorithm 2), and adaptive sampling (Algorithm 3) we compare estimates of the volume of the RoI $\mu_\Lambda(Q^{-1}(E))$ for some $E \subset \mathcal{B}_\mathcal{D}$. We generate 20 sets of uniform and adaptive samples and compare the average estimate of the relative volume of the RoI for increasing numbers of samples. We define the approximate relative volume as

$$x = \frac{\tilde{\mu}_\Lambda(Q^{-1}(E))}{\mu_\Lambda(\Lambda)} \quad (5.3.1)$$

and the relative error in the relative volume as

$$e = \frac{|\tilde{\mu}_\Lambda(Q^{-1}(E)) - \mu_\Lambda(Q^{-1}(E))|}{\mu_\Lambda(Q^{-1}(E))} \quad (5.3.2)$$

for $E \subset \mathcal{D}$. We use the QoI maps $Q = (q_1, q_2), (q_1, q_6)$ from the idealized inlet problem in Section 4.3 and compare both the relative volume (Equation (5.3.1)) and the relative error (Equation (5.3.2)) in Figure 5.3. Since we are using a piecewise-linear interpolant as a surrogate model we can exactly calculate the true volume $\mu_\Lambda(Q^{-1}(E))$ and the exact relative error. Notice that in the bottom left subplot of Figure 5.3 there is a crossover point between the estimates calculated using the uniform samples and the adaptive samples. This crossover shows the point at which the adaptive sampler successfully locates the RoI. Once the adaptive sampler locates the RoI it outperforms the uniform sampler as shown in Figure 5.3.

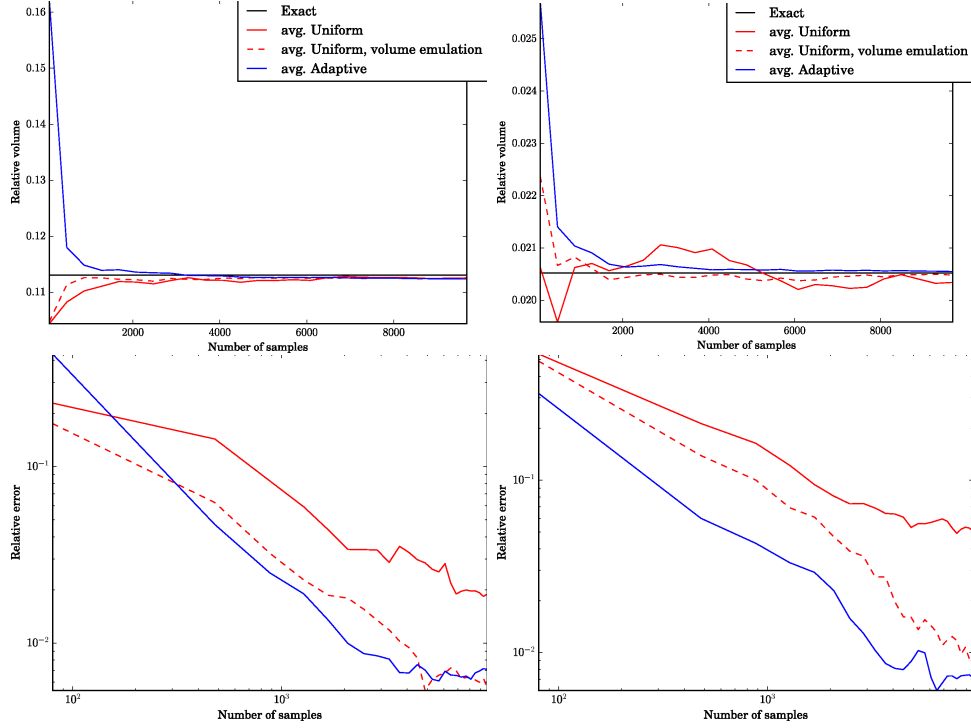


Figure 5.3: Mean results for 20 sets of uniform and adaptive samples for the idealized inlet. Top: The approximation of the relative volume of an implicitly defined region of interest $\mu_\Lambda(Q^{-1}(E))/\mu_\Lambda(\Lambda)$ for $Q = (q_1, q_2)$ on the left and (q_1, q_6) on the right respectively where $\lambda_{ref} = (\lambda_1, \lambda_2) = (0.0781, 0.168)$. Bottom: The corresponding error in the approximation of the relative volume for $Q = (q_1, q_2)$ on the left and (q_1, q_6) on the right.

The performance gain of the adaptive sampler is more significant as the difficulty in approximating the region of interest increases, or rather as the conditioning of the stochastic inverse problem improves. We must use the volume emulation Algorithm 2 to account for the non-uniformity of *both* the adaptive and uniform random samples. Volume emulation also has the added benefit of reducing the variance between solutions. The accuracy of results obtained using both uniform and adaptive samples is limited by the approximation of the volumes of the Voronoi cells via volume emulation as shown by the reported error statistics in Table 5.1 and Table 5.2. The tails of the error plots in Figure 5.3 also flatten out due to the limitations of using only 10^6 emulated samples.

Algorithm 3: A Probability Based Adaptive Sampler [32]

Let $\{\lambda^{(0,j)}\}_{j=1}^M \subset \Lambda$ denote an initial set of samples on Λ from a Latin hypercube.

Let $P_t(x, B(s))$ denote a transition probability kernel in Λ for a parameterized event $B(s)$.

Initialize $M \times 1$ vector $\mathbf{s} = \{s_j\}_{j=1}^M$ to some initial event size \mathbf{s}^0 .

Set relative size tolerance $\gamma \in (0, 1)$.

Specify subsets $\{D_k\}_{k=1}^K \subset \mathcal{D}$ and compute $p_k = \int_{D_k} \rho_{\mathcal{D}} d\mu_{\mathcal{D}}$.

for $j = 1, \dots, M$ **do**

if $Q(\lambda^{(0,j)}) \in D_{k'}$ *for some* k' **then**

 | $p_{0,j} = p_{k'}$

else

 | $p_{0,j} = 0$

end

end

Choose a user defined total number of batches N .

for $i = 1, \dots, N$ **do**

 Generate M parameter samples $\{\lambda^{(i,j)}\}_{j=1}^M$ using $P_t(\lambda^{(i-1,j)}, B(s_j))$.

for $j = 1, \dots, M$ **do**

if $Q(\lambda^{(i,j)}) \in D_{k'}$ *for some* k' **then**

 | $p_{i,j} = p_{k'}$

else

 | $p_{i,j} = 0$

end

if $p_{i,j} > (1 + \gamma)p_{i-1,j}$ **then**

 | $s_j = s_{decrease} s_j$

else if $p_{i,j} < \gamma p_{i-1,j}$ **then**

 | $s_j = s_{increase} s_j$

else

 | $s_j = s_j$

end

if $s_j/s_j^0 > s^{max}$ **then**

 | $s_j = s^{max} s_j^0$

else

 | $s_j/s_j^0 < s^{min}$

end

$s_j = s^{min} s_j^0$

end

end

Table 5.1: Statistics of adaptive volume estimates for the idealized inlet for (q_1, q_2) for 20 sets of samples.

Sample type	Relative volume		Relative error	
	\bar{x}	σ_x	\bar{e}	σ_e
9680 uniform	1.126e-01	2.452e-03	1.893e-02	1.140e-02
9680 uniform with emulation	1.125e-01	5.462e-04	5.611e-03	4.009e-03
9680 Adaptive	1.124e-01	7.035e-04	7.096e-03	4.817e-03
10^6 uniform	1.122e-01	2.302e-04	7.060e-03	2.037e-03

Table 5.2: Statistics of adaptive volume estimates for the idealized inlet for (q_1, q_6) for 20 sets of samples.

Sample type	Relative volume		Relative error	
	\bar{x}	σ_x	\bar{e}	σ_e
9680 uniform	2.034e-02	1.284e-03	5.067e-02	3.779e-02
9680 uniform with emulation	2.048e-02	2.357e-04	8.964e-03	7.442e-03
9680 Adaptive	2.055e-02	1.686e-04	7.160e-03	4.250e-03
10^6 uniform	2.050e-02	1.327e-04	5.011e-03	4.242e-03

Chapter 6

Conclusion and Future Work

6.1 Conclusion

Hurricanes annually impact the United States coast resulting in hundreds of deaths and billions of dollars in damage. The majority of damage and loss of life caused by hurricanes is due to storm surge, i.e. flooding or inundation caused by storms as they approach the coast and make landfall. The balance between wind stress and bottom stress is the primary controlling factor for storm surge [4]. Bottom stress in coastal engineering applications is usually modeled using Manning's formula which was originally developed to model bottom friction for unvegetated open channel flow. Manning's formula is not necessarily the most correct model of bottom stress in coastal engineering applications. In coastal regions vegetation, sub-grid porous media-like structures, bed forms, and erosion also contribute to bottom stress in addition to bottom friction. Despite this, Manning's formula is widely used and has proven highly useful in coastal ocean models. It is difficult and often impossible to directly observe the Manning's n coefficient in large geographic regions. The existence of the NCLD and C-CAP land cover and classification databases allow us to parameterize the spatial variance of Manning's n fields by land cover classification. With the use of expert knowledge and existing

field observations we can determine a plausible set of Manning's n coefficients to form the parameter space. This makes quantifying uncertainty in Manning's n for coastal engineering with a measure-theoretic approach to inverse problems a particularly interesting area of research. Improving estimates of bottom friction along with other modeling parameters for coastal areas will enhance predictive modeling for both storm surge and other coastal phenomena. This is especially relevant as a large percentage of the US and world population live in coastal regions.

Estimating Manning's coefficient for hurricane storm surge is an example of a deterministic inverse problem which is typical of many engineering and scientific applications. The physics-based model, M , is often given as a set of PDEs which form a map between input parameters, $\lambda \in \Lambda$, and the solution space $\{y : M(\lambda, y) = 0\}$. One set of functionals maps the solution space to the set of observable quantities in the observation space, while another set of functionals maps the solution space to the set of quantities we desire to predict. We refer to the map from the parameter space to the observation or data space as the quantity of interest (QoI) map Q [16]. We use observed data to solve the inverse problem for parameters which are then used to solve the forward predictive problem. There are two primary difficulties in solving this inverse problem. Firstly, the dimension of the observation or data space $\mathcal{D} \subset \mathbb{R}^d$ is often less than the dimension of the parameter space $\Lambda \subset \mathbb{R}^n$, $d < n$. This implies that the inverse QoI map is set-valued. Secondly, there is often error and noise in actual observed data which is not necessarily accounted for in

the model. The uncertainty in data may be modeled as a probability measure on the data space with the corresponding forward stochastic problem; given $(\Lambda, \mathcal{B}_\Lambda, P_\Lambda)$ and $Q : \Lambda \rightarrow \mathcal{D}$ determine $P_{\mathcal{D}}$ on $(\mathcal{D}, \mathcal{B}_{\mathcal{D}})$. The stochastic inverse problem is given $(\mathcal{D}, \mathcal{B}_{\mathcal{D}}, P_{\mathcal{D}})$ and $Q : \Lambda \rightarrow \mathcal{D}$ determine P_Λ on $(\Lambda, \mathcal{B}_\Lambda)$.

In Chapter 3, we summarize the theory behind solving stochastic inverse problems within a measure-theoretic framework. This framework models epistemic uncertainty with a probability distribution on the data space $\rho_{\mathcal{D}}$. Aleatoric uncertainty is captured for inverse problems with inherently set-valued inverses (i.e. when the parameter space has greater dimension than the data space) by naturally handling set-valued inverses rather than attempting to determine a single most likely parameter given a model and set of data. We briefly discuss the two sources of approximation error in solving the inverse problem (1) numerical error in the forward map and (2) numerical error in set approximation. We address how volume emulation can be used to ameliorate errors of the second type. We show how condition of the inverse problem is determined by the skewness of the Jacobian of the QoI map with respect to the parameters. This skewness dramatically influences the accuracy of the solution to the inverse problem and dictates the optimal choice of QoI. This is especially important if the solution of the inverse problem is to be later used for prediction.

In Chapter 4, we demonstrated the utility of a measure-theoretic framework for inverse problems in the estimation of Manning's n coefficients for two coastal engineering applications. We study both of these coastal engineering

applications using the ADvanced CIRCulation model for oceanic, coastal, and estuarine waters which incorporates spatially varying bottom friction fields as nodal parameters. We have applied computational measure-theoretic algorithms for quantifying uncertainty in mesoscale representations of Manning's n for an idealized inlet domain with a simple forcing scheme for two and three dimensional parameter domains. Results for the idealized inlet demonstrate the capacity numerical error has to pollute the QoI map. Refinement of the finite element mesh to adequately resolve the relevant flow scales produced noticeably smoother QoI maps with substantially different generalized contours [32].

For both the idealized inlet case study and the hurricane case study we have demonstrated that the accuracy of the solution of the inverse problem is highly dependent on the choice of the quantities of interest. Gathering physical observations or experimental measurements is often an expensive and time consuming process, the geometrical analysis of output data with respect to skewness is a valuable tool for experimental and observation network design. We can choose QoI maps based on the underlying geometric structure of the generalized contours to obtain probability measures with small support (relative to using other QoI maps). If the goal is to solve a stochastic inverse problem for parameter estimation, then identifying small regions of highly probable parameter configurations provides valuable information. These case studies demonstrate the impact that the condition of the inverse problem has on *both* the inverse and prediction problems. Hurricane simulations on meshes

fine enough to resolve inundation are computationally expensive. We employ a recently available subdomain implementation of ADCIRC [23–25] to reduce simulation time and focus on specific areas of interest rather than the much larger domain required for hurricane simulations. We have demonstrated the feasibility of parameter estimation within this measure-theoretic framework for a highly-complex physics based model of a historic hurricane with realistic bathymetry, wind fields, and land cover classification fields.

Many computational models of complex physical systems are expensive. As such we might only be able to obtain a limited number of forward solves (samples). It becomes increasingly difficult to locate high probability regions in higher dimensions as the volumes of high probability regions decreases as the dimension of the probability space increases [60]. As such we do not expect any significant improvement through the use of uniform sampling. Furthermore, uniform sampling allows too many samples to be placed in regions of zero or low probability which do not need to be accurately estimated. Thus, in Chapter 5 we developed and implemented a probability based goal-oriented adaptive sampling algorithm to place more samples in regions of high probability to accurately approximate the volumes of regions in Λ implicitly defined by sets in the data space $Q^{-1}(E) \in \mathcal{B}_{\mathcal{L}}$, where $E \in \mathcal{B}_{\mathcal{D}}$.

In order to account for the non-uniformity of both the adaptively generated samples and random uniform i.i.d. samples we employ volume emulation to estimate the volumes of the Voronoi cells. Volume emulation dramatically improves the solution by improving the disintegration of $P_{\mathcal{D}}$ for non-uniform

samples. Ideally, we desire to require as few forward model solves as possible through the use of adaptive sampling algorithms. The quality of the approximation of the probability measure calculated using adaptively generated samples is constrained by the ability to approximate volumes using volume emulation and therefore the computational cost is also partially determined by the method of nearest neighbor searches. If the goal is to determine the probability of a particular set that is implicitly defined by a set of conditions on the data space, goal-oriented adaptive sampling can help improve the accuracy of the solution of the inverse stochastic problem when we are limited by the number of forward model solves we can compute.

6.2 Future Work

We have applied a measure-theoretic framework for stochastic inverse problems to parameter estimation for a single subdomain during Hurricane Gustav to estimate Manning's coefficients for land cover classifications, or consider the parameterization uncertain. We could also examine other hurricanes, a purely tidal forcing scheme, other geographical subdomains and locations, or other coastal engineering parameters such as eddy viscosity and canopy parameters. There are many regions where we do not have land cover classification data (such as the South China Sea) where we would need to determine another appropriate spatial parameterization of bottom friction. We could also examine other physics based models both for coastal engineering and for other applications. If we augment the parameter space by a model

space we could compare models with respect to solving the inverse problem using a specified set of quantities of interest.

The choice of QoI can dramatically effect the solution to the inverse problem based on local conditioning of the Jacobian of the QoI map over the parameter space. Numerical errors in the QoI can drastically change the generalized contour geometry on the parameter space making inverse solutions unreliable. A geometric analysis of the QoI could be performed to determine the QoI most robust to numerical error for the solution of the inverse problem. Actual field or experimental data is often noisy, biased, or unsuitable; a statistical analysis of such data using Bayesian inference and other statistical modeling techniques may be used to construct probability measures $\rho_{\mathcal{D}}$ on geometrically optimal QoI ranges to be subsequently inverted using the measure-theoretic algorithms and tools developed in this project. Future research should also apply adjoint based a posteriori analysis whenever possible in both the geometric and statistical analysis to improve the efficiency of the computational algorithms and tools developed.

We have primarily focused on stochastic inverse problems in finite dimensional parameter and data spaces. Future research could develop theoretical tools to handle the proper definition of infinite-dimensional measures for the parameter spaces and data spaces. There is no translation-invariant measure for infinite dimensional spaces. An appropriate measure must be developed to solve the stochastic inverse problems when either the parameter space or the data space is infinite dimensional. This would provide insights

into the correct finite dimensional computational representation of spatially and temporally varying parameters that are members of an infinite dimensional space. We could develop the theory of functional assimilation for time varying quantities of interest and design mathematically rigorous and computationally efficient asynchronous techniques for the inversion of the probability measure on geometrically distinct QoI as they become available in time.

Goal-oriented adaptive sampling is a promising approach for estimating the probability of small sets or sets with complex geometry (i.e. threshold, failure, and extreme events). Developing new goal-oriented adaptive sampling approaches to employ gradient (adjoint) and approximate gradient based techniques will add to the arsenal of methods designed to reduce computational costs. Increasing the density of samples in (and around) a region of interest results in Voronoi cells with drastically different volumes. Currently, we employ volume emulation to account for the variation in Voronoi cell volumes. We could employ an adaptive multi-level volume emulation algorithm to reduce the cost of volume emulation, and obtain volume estimates of Voronoi cells in a more scalable and efficient manner. We could also enhance adaptive sampling by using surrogate models and/or local error estimates to efficiently utilize a limited number of forward model solves.

We have motivated this work as a way of improving and adding confidence to coastal ocean engineering models. These models are used to predict highly destructive natural events and other natural phenomena. As is we have shown that within a measure-theoretic framework for stochastic inverse

problems there are several important considerations for both inversion and prediction. The two primary sources of error in the numerical solution of the stochastic inverse problem are error in the forward model and error in the numerical approximation of sets. We employ volume emulation and a probability based goal-oriented adaptive sampling scheme to reduce errors of the second type. We have proposed possible ways to use gradient information to improve adaptive sampling in future work. We have also shown the influence that the choice of quantities of interest have on the numerical accuracy of the solution of the inverse problem. We have identified areas of possible future work that include the proper construction of the probability density on the parameter space and the choice of optimal quantities of interest with respect to skewness when using non-synthetic data. Often we deal with inverse problems in coastal engineering that produce a parameter space that has higher dimension than the data space. In this setting the inverse quantity of interest map is inherently set-valued. A measure-theoretic framework for stochastic inverse problems captures this inherently set-valued inverse and has proven a valuable tool for parameter estimation for Manning's n for coastal engineering problems.

Appendices

Appendix A

Modeling Flow Resistance with Manning's Formula

Manning's formula is used to characterize momentum loss due to bottom friction in turbulent gravity driven open-channel flow over rough beds [9, 11, 33, 38, 61]. Manning's formula in Equation (A.0.1) relates V , the mean velocity of the flow; R , the hydraulic radius; S , the slope of the channel; and n , the roughness coefficient known as Manning's n

$$V = \frac{K_n}{n} R^{2/3} S^{1/2} \quad (\text{A.0.1})$$

where $K_n = \{1 \text{ m}^{1/2}/\text{s}, 1.486 \text{ ft}^{1/3}\text{-m}^{1/6}/\text{s}\}$ for SI and Imperial units respectively [10, 11, 40, 41]. The formulation in Equation (A.0.1) is dimensionally inhomogeneous. Generally a dimensionally homogeneous form is preferred and Strickler, Dooge, and Mostafa and McDermid have provided such a formulation

$$V = M \left(\frac{R}{k_s} \right)^{1/6} \sqrt{RgS} \quad (\text{A.0.2})$$

where $M = (K_n/\sqrt{g})(k_s^{1/6}/n)$ in which k_s is the equivalent Nikuradse sand roughness [10, 11, 33, 34]. The Darcy–Weisbach and Chézy friction coefficients are also used to relate roughness to the mean velocity of open channel flow [11, 33, 38]. These roughness coefficients are related such that given one coefficient

the other two can be determined [11, 33]. Although all three of these roughness coefficients may be related, Manning's n is primarily used in hydraulic and civil engineering.

Manning's formula was originally empirically developed for use in river engineering (e.g. [10, 35, 40]). Recently, Gioia and Bombardelli have given possibly the first theoretical derivation of Manning's formula. Gioia and Bombardelli re-derive Manning's formula for turbulent flow in open channels from the Reynolds-averaged Navier-Stokes equations using scaling techniques and turbulence theory [9].

We will summarize the derivation of the dimensionally homogeneous Manning's formula by Gioia and Bombardelli to attain the relation

$$V = M \left(\frac{R}{r} \right)^{1/6} \sqrt{gRS} \quad (\text{A.0.3})$$

where r is an absolute roughness [9]. Consider a prismatic rectangular channel of height h , slope S , width b , lined with uniform roughness elements of size r reproduced in Figures A.1a and A.1b [9]. In this derivation the water surface height matches that of the channel. We limit the scope to applications where the roughness elements are small $r \ll R$ [9, 61, 62] since larger roughness elements may change the nature of the flow. We assume that the flow is turbulent since this is true for many natural flows and transition for distributed roughness (i.e. sand-grain roughness) occurs when $\frac{Vr}{\nu} \gtrsim 120$, where ν is the dynamic viscosity, as reported by Feindt [63].

Gioia and Bombardelli's derivation begins from the Reynolds-averaged

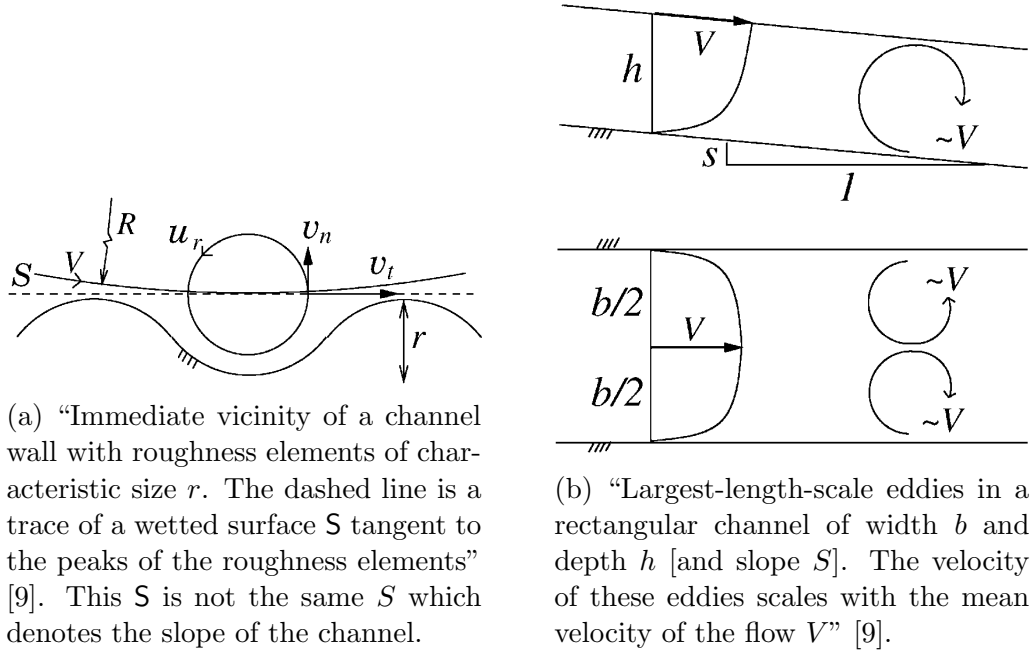


Figure A.1: Channel geometry reproduced from [9].

Navier-Stokes equations

$$\rho \frac{D\bar{\mathbf{V}}}{Dt} = \rho \left(\frac{\partial \bar{\mathbf{V}}}{\partial t} + \bar{\mathbf{V}} \cdot \nabla \bar{\mathbf{V}} \right) = \rho \mathbf{g} - \nabla \bar{p} + \nabla \cdot \boldsymbol{\tau} \quad (\text{A.0.4})$$

$$\tau_{ij} = \mu \left(\frac{\partial v_i}{\partial x_j} + \frac{\partial v_j}{\partial x_i} \right) - \rho \overline{v'_i v'_j} \quad (\text{A.0.5})$$

$$\nabla \cdot \bar{\mathbf{V}} = 0 \quad (\text{A.0.6})$$

where vector quantities are in bold, $\bar{\mathbf{V}}$ is the time-average velocity, ρ is the density, \mathbf{g} is gravitational acceleration, \bar{p} is the time-average pressure, $\boldsymbol{\tau}$ is the stress tensor, $\mu = \nu\rho$ is the dynamic viscosity (ν is the kinematic viscosity), and $\overline{v'_i v'_j}$ are the Reynolds stresses [9,10,41,63,64]. We assume a steady-uniform mean flow to attain Equation (A.0.7) from Equation (A.0.4)

$$0 = \rho \mathbf{g} - \nabla \bar{p} + \nabla \cdot \boldsymbol{\tau}. \quad (\text{A.0.7})$$

In the case of two-dimensional mean flow, $\bar{w} = 0$ and $\frac{\partial(\cdot)}{\partial z} = 0$ [63] which implies

$$\frac{\partial \bar{u}}{\partial x} + \frac{\partial \bar{v}}{\partial y} = 0 \quad (\text{A.0.8})$$

by continuity (conservation of mass). Therefore

$$\tau_{ij} = -\rho \overline{v'_i v'_j} \quad \forall \quad i, j = n, t \quad (\text{A.0.9})$$

where t denotes the direction tangent to the flow and n denotes the direction normal to the flow. Equations (A.0.7) and (A.0.9) can be combined and rewritten as

$$0 = g_t - \frac{1}{\rho} \frac{\partial \bar{p}}{\partial x_t} - \frac{\partial \overline{v'_t v'_t}}{\partial x_t} - \frac{\partial \overline{v'_t v'_n}}{\partial x_n}. \quad (\text{A.0.10})$$

The momentum equation for the normal direction is similar and omitted for brevity.

In two-dimensional channel flow (e.g. with pipe, wake, jet, and boundary layer flow), changes in the direction tangent to the flow are much smaller than changes in the direction normal to the flow $\frac{\partial}{\partial x_t} \ll \frac{\partial}{\partial x_n}$ and $\bar{v}_n \ll \bar{v}_t$ [61,63]. This implies that

$$g_t - \frac{\partial \overline{v'_t v'_n}}{\partial x_n} = 0 \quad (\text{A.0.11})$$

or more importantly

$$g_t = \frac{1}{\rho} \nabla \cdot \boldsymbol{\tau}_t \quad (\text{A.0.12})$$

where $|\boldsymbol{\tau}_t| \sim |\tau_{tn}| \sim \rho \overline{|v'_n v'_t|}$. At this point we integrate over the volume for a

unit length of the channel and apply the divergence theorem

$$\begin{aligned}
\int_0^b \int_0^h \int_0^1 g_t dV &= \frac{1}{\rho} \int_0^b \int_0^h \int_0^1 \nabla \cdot \boldsymbol{\tau}_t dV \\
bhg_t &= \frac{1}{\rho} \oint_S (\boldsymbol{\tau}_t \cdot \mathbf{n}) dS \approx \frac{1}{\rho} (b + 2h) \tau_{tn} \\
bhg_t &\sim (b + 2h) |\overline{v'_n v'_t}|
\end{aligned} \tag{A.0.13}$$

, i.e. the gravitational force is equal to the tangent force [35]. We incorporate the small angle approximation $g_t = g \sin(\arctan(S)) \approx g \tan(\arctan(S)) = gS$ into Equation (A.0.13)

$$gSbh \sim (b + 2b) |\overline{v'_n v'_t}| \tag{A.0.14}$$

which corresponds with both Leopold et. al. and Gioia and Bombardelli's derivations [9, 35]. Note that $|\overline{v'_n v'_t}| \sim |v'_n| |v'_t|$. Then all that remains is to determine appropriate forms of $|v'_n|$ and $|v'_t|$ to reduce

$$|v'_n| |v'_t| \sim \left(\frac{bh}{b + 2h} \right) gS = RgS \tag{A.0.15}$$

to Manning's formula.

These velocities, $|v'_n| |v'_t|$, are dependent upon the eddies which dominate the normal and tangent flows. Eddies of size r dominate the normal flow with velocity u_r so $|v'_n| \sim u_r$ (see Figure A.1a) [9]. There is no single eddy size that dominates the tangent flow so $|v'_t| \sim V$ [9]. We substitute these relations into Equation (A.0.15)

$$RgS \sim u_r V. \tag{A.0.16}$$

However, we still require u_r in terms of n , R , r , and/or V .

Gioia and Bombardelli use Kolmogórov’s scaling (Equation (A.0.17)) to relate u_r and V [9] which applies to anisotropic, inhomogeneous turbulence (in addition to homogeneous turbulence) according to Knight and Sirovich [9, 65]. Kolmogórov’s scaling applies if $r \gg \eta$, where η is the Kolmogórov length (i.e. the eddies of size r are within the inertial range) [9, 65]. Under these conditions, the applicable Kolmogórov scaling is

$$\frac{u_r^3}{r} \sim \varepsilon \sim \kappa \quad (\text{A.0.17})$$

where ε is the dissipation rate of turbulent kinetic energy and κ is the rate of production of turbulent kinetic energy [9, 63, 65–68]. The largest eddies are the sources of production of turbulent kinetic energy thus

$$\kappa \sim \underbrace{\frac{V^2}{h/V}}_{\text{horizontal}} + \underbrace{\frac{V^2}{b/2V}}_{\text{vertical}} \quad (\text{A.0.18})$$

since the horizontal turn over rate is h/V and the vertical turn over rate is $(b/2)/V$ (see Figure A.1b) [9]. We combine Equation (A.0.17) and Equation (A.0.18) to attain

$$\frac{u_r^3}{r} \sim \frac{V^3}{h} + \frac{2V^3}{b} = \left(\frac{2+2h}{bh} \right) V^3 = \frac{V^3}{R} \quad (\text{A.0.19})$$

and

$$u_r \sim \left(\frac{r}{R} \right)^{1/3} V \quad (\text{A.0.20})$$

[9, 67]. Finally, Equation (A.0.20) may be substituted into Equation (A.0.16) to obtain

$$V \sim \left(\frac{R}{r} \right)^{1/6} \sqrt{RgS} \quad (\text{A.0.21})$$

[9]. This implies that there exists a constant $M \geq 0$ such that

$$V = M \left(\frac{R}{r} \right)^{1/6} \sqrt{RgS} \quad (\text{A.0.22})$$

which is the desired form of the Manning's formula. See Gioia and Bombardelli for a generalization walls with roughness elements of varying sizes [9].

Appendix B

Scientific Software Contributions

BET is a Python package for measure-theoretic inverse problems and uncertainty quantification [22]. BET is named after the primary developers (Butler, Estep, Tavener) of the measure-theoretic framework for inverse problems it implements. We developed the Python package BET [22] to solve stochastic inverse problems formulated in the measure-theoretic framework described in this paper. We developed the Python package PolyADCIRC [21] to be interfaced with BET in order to solve the stochastic inverse problem for general ADCIRC parameter fields. Both Python packages utilize a number of Numpy, SciPy, and various packages from the Python Package Index. PolyADCIRC also makes use of GNU Parallel [69]. The BET package is designed to handle every step of Algorithms 1 to 3 with a variety of prepackages, modules, and methods that are called using simple Python scripts to (1) define and sample Λ efficiently, (2) determine the optimal choice of QoI, (3) compute the approximate probability measure, and (4) visualize results. The PolyADCIRC package is designed to efficiently interface between the BET package and the P(arallel)ADCIRC simulations in an HPC environment in order to obtain the QoI associated with each input sample. We provide some more specific details about these packages and functionality below.

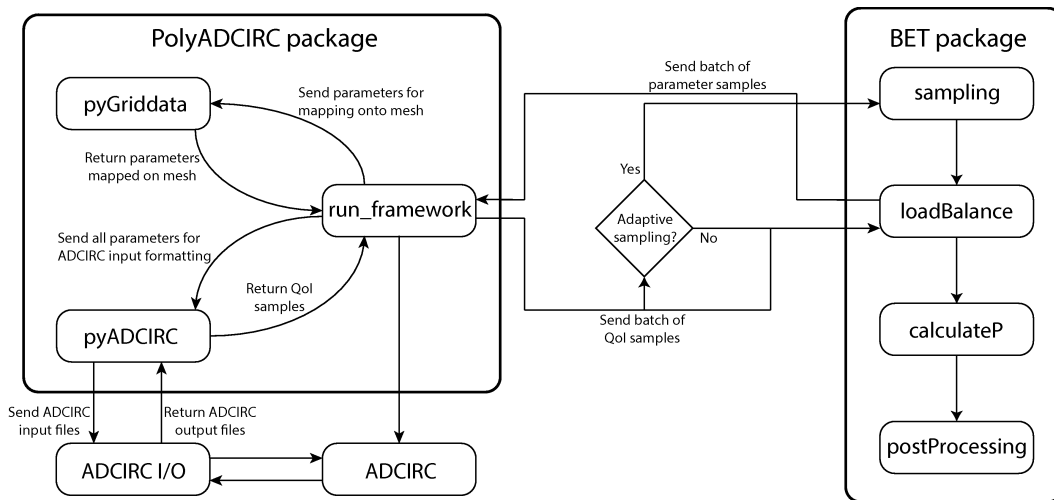


Figure B.1: The basic flowchart for the BET and PolyADCIRC packages. The BET package handles every step in Algorithm 1 while using the PolyADCIRC package to efficiently interface to the ADCIRC computational model. Note in this figure *loadBalance* is a user created interface to PolyADCIRC.

The BET package is divided into four sub-packages (1) **sampling**, (2) **sensitivity**, (3) **calculateP**, and (4) **postProcess**. The **sampling** sub-package provides the tools to sample the parameter space uniformly, adaptively, or at a set of user-defined points. The **sampling** sub-package provides modules to efficiently sample the forward model and can take into account the most recent QoI values to adaptively choose new batches of input parameters. This requires the user to create an interface that is specific to the model and/or HPC infrastructure in order to implicitly construct the maps from parameter samples to the associated QoI, e.g. as we do with PADCIRC using the PolyADCIRC package described below. The **sensitivity** sub-package allows the user

to approximate the Jacobian of Q at a given set of samples and determine the optimal set of QoI to use to create a well-conditioned stochastic inverse problem. Once the data sets containing parameter and QoI values are obtained, they are post-processed using the `calculateP` sub-package to obtain the approximate probability measure using Algorithm 1. Within `calculateP` is a module named `simpleFun` used to create simple function approximations of $P_{\mathcal{D}}$ that are inverted according to Algorithm 1. The `calculateP` sub-package provides several options for approximating the volume of the Voronoi cells $\{\mathcal{V}_j\}$ associated with each parameter sample including using various Monte Carlo approximations or more accurate approximations based on triangulations of the Voronoi cells. The `postProcess` sub-package can be used to visualize the approximate probability densities and marginals, the approximate data domain, \mathcal{D} , and the parameter domain. The `postProcess` sub-package also provides methods for sorting probability data, identifying regions of high probability, and saving data in parallel.

Parallelization in BET is implemented using `mpi4py`, however, `mpi4py` is *not* necessary for installation. BET implements Algorithm 3 using independent generalized chains. Each generalized chain $\{\lambda(\cdot, j)\}$ is independent from all other chains $\{\lambda(\cdot, k)\}$, $k \neq j$ so parallelization for a sampling a serial model is trivial. Given n processors M/n generalized chains are distributed per processor where M is the total number of generalized chains. Results are periodically saved at each step and collected using `mpi4py.MPI.Comm.Allgather` as a final step and saved. This allows the option of loading the saved samples

later or continuing with the parallel methods in `calculateP` or `postProcess`. If you have a parallel computational model we currently suggest you use the serial version of the sampling routines and write a python wrapper for your model (`loadBalance`) that runs batches of samples simultaneously based on the computational resource requirements of your model. All of the methods in the `calculateP` module of `calculateP` provide performance benefits with run in parallel. The implementations of Algorithms 1 to 3 are trivially parallelizable as they rely on Monte Carlo integration and generalized chains which are independent. However, parallelization may become less trivial as we implement more sophisticated integration and sampling methods such as a 2-level volume emulation scheme or a gradient based adaptive sampling scheme. The current parallelization allows for large numbers of emulated samples to be used for volume emulation so that we can approximate the volumes of Voronoi cells even in high dimensions.

The PolyADCIRC package is divided into three sub-packages (1) `pyADCIRC`, (2) `pyGriddata`, and (3) `run_framework`. The `run_framework` sub-package provides the framework to simultaneously run PADCIRC simulations with varying Manning's n and bathymetry fields. The `pyGriddata` sub-package provides various methods and classes to create the parametrization vectors shown in Figure 4.2 using a slightly modified version of GridData (`Griddata_v1.32.F90`) to map the land classification contributions to the computational mesh. GridData is a FORTRAN program originally developed by Seizo Tanaka and C.H.Lab at the University of Notre Dame [26]. The `pyADCIRC` sub-package

provides the methods and data structures used to interact with and alter PAD-CIRC formatted files. In the numerical examples shown, `pyADCIRC` creates the necessary formatted input files for ADCIRC based on the mesh parameter values returned by `pyGriddata`. Following completion of the model simulations for each batch of parameter samples, `pyADCIRC` reads in the formatted output files and returns the requested QoI values. The `PolyADCIRC` package was originally developed to execute parameter sweeps of Manning's n fields and simple bathymetry alterations; however, it can be adapted to handle other ADCIRC input parameters such as the location of a canopy or eddy viscosity. The `PolyADCIRC` package was originally developed for TACC HPC systems, but it can be adapted to run on other Linux based HPC systems. The `PolyADCIRC` package also provides modules to interface with a slightly modified version of Subdomain ADCIRC [25], however these modules have not yet been made publicly available. Note an earlier version of this material was previously published in [32]. Both of these Python packages are available online open source at <https://github.com/UT-CHG>.

Bibliography

- [1] E. Blake, C. Landsea, E. Gibney, and N. Asheville, *The deadliest, costliest, and most intense United States tropical cyclones from 1851 to 2006 (and other frequently requested hurricane facts)*. NOAA/National Weather Service, National Centers for Environmental Prediction, National Hurricane Center, 2007. www.nhc.noaa.gov/pdf/NWS-TPC-5.pdf.
- [2] M. Craft, “Hurricane Sandy’s Economic Damage Could Reach \$50 Billion, Egecat Estimates,” *Huffington Post*, November 01 2011. www.huffingtonpost.com/2012/11/01/hurricane-sandy-economic-damage_n_2057850.html.
- [3] J. Schubert, B. Sanders, M. Smith, and N. Wright, “Unstructured Mesh Generation and Landcover-based Resistance for Hydrodynamic Modeling of Urban Flooding,” *Advances in water resources*, vol. 31, no. 12, pp. 1603–1621, 2008.
- [4] C. Dawson, E. Kubatko, J. Westerink, C. Trahan, C. Mirabito, C. Michoski, and N. Panda, “Discontinuous Galerkin methods for modeling Hurricane storm surge,” *Advances in Water Resources*, vol. 34, no. 9, pp. 1165–1176, 2011. DOI: 10.1016/j.advwatres.2010.11.004.
- [5] R. Luettich and J. Westerink, *Formulation and numerical implementa-*

- tion of the 2D/3D ADCIRC finite element model version 44. XX.* R. Luettich, 2004.
- [6] R. Luettich and J. Westerink, *ADCIRC User Manual: A (Parallel) Advanced Circulation Model for Oceanic, Coastal AND Estuarine Waters*. University of North Carolina at Chapel Hill and University of Notre Dame, version 49 ed., April 1 2010.
- [7] S. Bunya, J. Dietrich, J. Westerink, B. Ebersole, J. Smith, J. Atkinson, R. Jensen, D. Resio, R. Luettich, C. Dawson, *et al.*, “A High-Resolution Coupled Riverine Flow, Tide, Wind, Wave, and Storm Surge Model for Southern Louisiana and Mississippi. Part I: Model Development and Validation,” *Monthly Weather Review*, vol. 138, no. 2, pp. 345–377, 2010. <http://dx.doi.org/10.1175/2009MWR2906.1>.
- [8] L. Noarayanan, K. Murali, and V. Sundar, “Manning’s n Co-efficient for Flexible Emergent Vegetation in Tandem Configuration,” *Journal of Hydro-environment Research*, vol. 6, no. 1, pp. 51–62, 2012.
- [9] G. Gioia and F. A. Bombardelli, “Scaling and Similarity in Rough Channel Flows,” *Physical review letters*, vol. 88, no. 1, p. 14501, 2001.
- [10] J. Dooge, *Channel Flow Resistance: Centennial of Manning’s Formula*, ch. The Manning Formula in Context, pp. 136–185. Littleton, Colorado: Water Resources Publications, 1992.
- [11] B. Yen, “Open Channel Flow Resistance,” *Journal of Hydraulic Engineering*, vol. 128, no. 1, pp. 20–39, 2002.

- [12] G. E. Box and N. R. Draper, *Empirical model-building and response surfaces*, vol. 424. Wiley New York, 1987.
- [13] R. C. Smith, *Uncertainty Quantification: Theory, Implementation, and Applications*, vol. 12. SIAM, 2013.
- [14] G. Forzieri, M. Degetto, M. Righetti, F. Castelli, and F. Preti, “Satellite Multispectral Data for Improved Floodplain Roughness Modelling,” *Journal of Hydrology*, vol. 407, no. 1, pp. 41–57, 2011. <http://dx.doi.org/10.1016/j.jhydrol.2011.07.009>.
- [15] M. E. Agnew, “Surge and Wave Propagation over Wetlands with Respect to Storm Forward Speed,” Master’s thesis, University of Notre Dame, 2012.
- [16] J. Breidt, T. Butler, and D. Estep, “A Measure-Theoretic Computational Method for Inverse Sensitivity Problems I: Method and Analysis,” *SIAM Journal on Numerical Analysis*, vol. 49, no. 5, pp. 1836–1859, 2011. DOI:10.1137/100785946.
- [17] T. Butler and D. Estep, “A numerical method for solving a stochastic inverse problem for parameters,” *Annals of Nuclear Energy*, vol. 52, no. 0, pp. 86–94, 2013. <http://www.sciencedirect.com/science/article/pii/S0306454912001806>.
- [18] T. Butler, D. Estep, S. Tavener, C. Dawson, and J. Westerink, “A Measure-Theoretic Computational Method for Inverse Sensitivity Problems III: Multiple Quantities of Interest,” *SIAM/ASA Journal on Un-*

- certainty Quantification*, vol. 2, no. 1, pp. 174–202, 2014. <http://epubs.siam.org/doi/abs/10.1137/130930406>.
- [19] T. Butler, D. Estep, S. Tavener, T. Wildey, C. Dawson, and L. Graham, “Solving Stochastic Inverse Problems using Sigma-Algebras on Contour Maps,” 2014. <http://arxiv.org/pdf/1407.3851>.
- [20] T. Butler, D. Estep, and J. Sandelin, “A Computational Measure Theoretic Approach to Inverse Sensitivity Problems II: A Posteriori Error Analysis,” *SIAM Journal on Numerical Analysis*, vol. 50, no. 1, pp. 22–45, 2012. <http://epubs.siam.org/doi/abs/10.1137/100785958>.
- [21] L. Graham, “PolyADCIRC.” online, 2013. <https://github.com/UT-CHG/PolyADCIRC>.
- [22] L. Graham, S. A. Mattis, T. Butler, and S. Walsh, *BET Package*. University of Texas at Austin, 2013. <https://github.com/UT-CHG/BET>.
- [23] J. S. Simon, “A Computational Approach for Local Storm Surge Modeling,” Master’s thesis, North Carolina State University, 2011. <http://repository.lib.ncsu.edu/ir/handle/1840.16/7179>.
- [24] A. Altuntas, “Downscaling Storm Surge Models for Engineering Applications,” Master’s thesis, North Carolina State University, 2012. <http://repository.lib.ncsu.edu/ir/bitstream/1840.16/8035/1/etd.pdf>.
- [25] A. Altuntas and J. S. Simon, “Subdomain ADCIRC v.50 User Guide,” tech. rep., North Carolina State University, <http://www4.ncsu.edu/~jwb/subdomain/>, 2013.

- [26] S. Tanaka, *Quick Manual of GRID_DATA*. University of Notre Dame, Oct 2012.
- [27] S. Walsh, “Optimal Choice of Quantifies of Interest for the Stochastic Inverse Problem.” Personal Communication, 2015.
- [28] J. Dietrich, S. Bunya, J. Westerink, B. Ebersole, J. Smith, J. Atkinson, R. Jensen, D. Resio, R. Luettich, C. Dawson, *et al.*, “A high-resolution coupled riverine flow, tide, wind, wind wave, and storm surge model for southern Louisiana and Mississippi. Part II: Synoptic description and analysis of Hurricanes Katrina and Rita,” *Monthly Weather Review*, vol. 138, no. 2, pp. 378–404, 2010. <http://dx.doi.org/10.1175/2009MWR2907.1>.
- [29] A. Kennedy, U. Gravois, B. Zachry, J. Westerink, M. Hope, J. Dietrich, M. Powell, A. Cox, R. Luettich Jr, and R. Dean, “Origin of the Hurricane Ike forerunner surge,” *Geophysical Research Letters*, vol. 38, no. 8, p. L08608, 2011.
- [30] M. Hope, J. Westerink, A. Kennedy, P. Kerr, J. Dietrich, C. Dawson, C. Bender, J. Smith, R. Jensen, M. Zijlema, *et al.*, “Hindcast and validation of Hurricane Ike (2008) waves, forerunner, and storm surge,” *Journal of Geophysical Research: Oceans*, vol. 118, no. 9, pp. 4424–4460, 2013.
- [31] J. Dietrich, J. Westerink, A. Kennedy, J. Smith, R. Jensen, M. Zijlema, L. Holthuijsen, C. Dawson, R. Luettich Jr, M. Powell, *et al.*, “Hurricane

- Gustav (2008) waves and storm surge: Hindcast, synoptic analysis, and validation in Southern Louisiana,” *Monthly Weather Review*, vol. 139, no. 8, pp. 2488–2522, 2011.
- [32] T. Butler, L. Graham, D. Estep, C. Dawson, and J. Westerink, “Definition and solution of a stochastic inverse problem for the manning’s n parameter field in hydrodynamic models,” *Advances in Water Resources*, vol. 78, no. 0, pp. 60 – 79, 2015.
- [33] B. Yen, “Dimensionally homogeneous Manning’s formula,” *Journal of hydraulic engineering*, vol. 118, no. 9, pp. 1326–1332, 1992.
- [34] B. C. Yen, “Channel Flow Resistance: Centennial of Manning’s Formula,” in *Channel Flow Resistance: Centennial of Manning’s Formula*, (Littleton, Colorado), Water Resources Pub, 2004.
- [35] L. B. Leopold, G. M. Wolman, and J. P. Miller, *Fluvial processes in geomorphology*. San Francisco: W. H. Freeman, 1964.
- [36] W. Myers, D. Knight, J. Lyness, J. Cassells, F. Brown, D. WEISBACH, *et al.*, “Resistance coefficients for inbank and overbank flow.,” *Proceedings of the ICE-Water Maritime and Energy*, vol. 136, no. 2, pp. 105–115, 1999.
- [37] H. H. .-H. H. Barnes, *Roughness characteristics of natural channels*, vol. 1849. Washington: U.S. Govt. Print. Off, 1967.
- [38] J. Bathurst, “Flow resistance estimation in mountain rivers,” *Journal of Hydraulic Engineering*, vol. 111, no. 4, pp. 625–643, 1985.

- [39] N. Clifford, A. Robert, and K. Richards, “Estimation of flow resistance in gravel-bedded rivers: A physical explanation of the multiplier of roughness length,” *Earth Surface Processes and Landforms*, vol. 17, no. 2, pp. 111–126, 1992.
- [40] G. J. Arcement, V. R. Schneider, and U. S. F. H. Administration, “Guide for Selecting Manning’s Roughness Coefficients for Natural Channels and Flood Plains United States Geological Survey Water-supply Paper 2339,” Tech. Rep. 2339., For sale by the Books and Open-File Section, U.S. Geological Survey, 1989.
- [41] V. T. . Chow, *Open-channel hydraulics*. Caldwell, N.J: Blackburn Press, 2008.
- [42] S. Lane, “Acting, predicting and intervening in a socio-hydrological world,” *Hydrology and Earth System Sciences*, vol. 18, no. 3, pp. 927–952, 2014.
- [43] T. V. Wamsley, M. A. Cialone, J. M. Smith, J. H. Atkinson, and J. D. Rosati, “The potential of wetlands in reducing storm surge,” *Ocean Engineering*, vol. 37, no. 1, pp. 59–68, 2010.
- [44] N. Kouwen and T. E. Unny, “Flexible roughness in open channels,” *Journal of the Hydraulics Division*, vol. 99, no. 5, pp. 713–728, 1973.
- [45] E. Mignot, A. Paquier, and S. Haider, “Modeling floods in a dense urban area using 2D shallow water equations,” *Journal of Hydrology*, vol. 327, no. 1, pp. 186–199, 2006.

- [46] G. Schumann, P. Matgen, L. Hoffmann, R. Hostache, F. Pappenberger, and L. Pfister, “Deriving distributed roughness values from satellite radar data for flood inundation modelling,” *Journal of Hydrology*, vol. 344, no. 1, pp. 96–111, 2007.
- [47] S. C. Medeiros, S. C. Hagen, and J. F. Weishampel, “Comparison of floodplain surface roughness parameters derived from land cover data and field measurements,” *Journal of Hydrology*, vol. 452, pp. 139–149, 2012.
- [48] T. Tao and N. Kouwen, “Remote sensing and fully distributed modeling for flood forecasting,” *Journal of Water Resources Planning and Management*, vol. 115, no. 6, pp. 809–823, 1989.
- [49] J. Yang, P. Reichert, and K. C. Abbaspour, “Bayesian uncertainty analysis in distributed hydrologic modeling: A case study in the thur river basin (switzerland),” *Water resources research*, vol. 43, no. 10, 2007.
- [50] J. W. Hall, L. J. Manning, and R. K. Hankin, “Bayesian calibration of a flood inundation model using spatial data,” *Water Resources Research*, vol. 47, no. 5, 2011.
- [51] T. Butler, M. Altaf, C. Dawson, I. Hoteit, X. Luo, and T. Mayo, “Data Assimilation within the Advanced Circulation (ADCIRC) Modeling Framework for Hurricane Storm Surge Forecasting,” *Monthly Weather Review*, vol. 140, no. 7, pp. 2215–2231, 2012.
- [52] Y. Ding and S. Wang, “Identification of Manning’s roughness coeffi-

- icients in channel network using adjoint analysis,” *International Journal of Computational Fluid Dynamics*, vol. 19, no. 1, pp. 3–13, 2005.
- [53] NOAA Coastal Services Center, “Coastal Change Analysis Program Regional Land Cover.” online, March 2013.
- [54] T. Butler, L. Graham, S. A. Mattis, and S. Walsh, “A measure-theoretic interpretation of sample based numerical integration with applications to inverse and prediction problems under uncertainty.” in preparation, July 2015.
- [55] R. Khatibi, J. Williams, and P. Wormleaton, “Identification problem of open-channel friction parameters,” *Journal of Hydraulic Engineering*, vol. 123, no. 12, pp. 1078–1088, 1997.
- [56] T. Butler and T. Wildey, “Utilizing Surrogate Models and Error Estimates to Accurately Predict Probabilities of Events,” *In preparation*, 2014. Submitted.
- [57] J. Dietrich, M. Zijlema, J. Westerink, L. Holthuijsen, C. Dawson, R. Luettich, R. Jensen, J. Smith, G. Stelling, and G. Stone, “Modeling hurricane waves and storm surge using integrally-coupled, scalable computations,” *Coastal Engineering*, vol. 58, no. 1, pp. 45–65, 2011.
- [58] T. A. C. C. (TACC), “Stampede User Guide.” <https://portal.tacc.utexas.edu/user-guides/stampede>, January 2015.
- [59] “Reference tables for Manning’s n values for Channels, Closed Conduits Flowing Partially Full, and Corrugated Metal Pipes.” <http://www>.

fsl.orst.edu/geowater/FX3/help/8_Hydraulic_Reference/Mannings_n_ Tables.htm, 2015.

- [60] A. Tarantola, *Inverse Problem Theory and Methods for Model Parameter Estimation*. SIAM, 2005.
- [61] V. Nikora, D. Goring, I. McEwan, and G. Griffiths, “Spatially averaged open-channel flow over rough bed,” *Journal of Hydraulic Engineering*, vol. 127, no. 2, pp. 123–133, 2001.
- [62] J. Jiménez, “Turbulent flows over rough walls,” *Annu. Rev. Fluid Mech.*, vol. 36, pp. 173–196, 2004.
- [63] F. M. White, *Viscous Fluid Flow*. Boston: McGraw-Hill, 3rd ed., 2006.
- [64] J. P. Bonnet, M. N. Glauser, I. U. of Theoretical, and A. Mechanics, “Eddy structure identification in free turbulence shear flows: selected papers from the IUTAM symposium entitled: “Eddy structures identification in free turbulent shear flows,” Poitiers, France, 12-14 October 1992,” in *Eddy structures identification in free turbulent shear flows*, vol. 21, (Boston), Kluwer Academic Publishers, 1993.
- [65] B. Knight and L. Sirovich, “Kolmogorov inertial range for inhomogeneous turbulent flows,” *Physical review letters*, vol. 65, no. 11, pp. 1356–1359, 1990.
- [66] S. Pope, *Turbulent flows*. Cambridge university press, 2000.
- [67] U. Frisch, *Turbulence: the legacy of A.N. Kolmogorov*. Cambridge: Cambridge University Press, 1995.

- [68] D. Lohse, “Crossover from High to Low Reynolds Number Turbulence,” *Phys. Rev. Lett.*, vol. 73, pp. 3223–3226, Dec 1994.
- [69] O. Tange, “Gnu parallel - the command-line power tool,” *login: The USENIX Magazine*, vol. 36, pp. 42–47, Feb 2011.
- [70] T. A. C. C. (TACC), “Lonestar User Guide.” <https://portal.tacc.utexas.edu/user-guides/lonestar>, January 2015.
- [71] M. T. Ayvaz, “A linked simulation–optimization model for simultaneously estimating the manning’s surface roughness values and their parameter structures in shallow water flows,” *Journal of Hydrology*, vol. 500, pp. 183–199, 2013.
- [72] H. M. Azamathulla and R. D. Jarrett, “Use of gene-expression programming to estimate manning’s roughness coefficient for high gradient streams,” *Water resources management*, vol. 27, no. 3, pp. 715–729, 2013.
- [73] O. Bakken, P. Krogstad, A. Ashrafiyan, and H. Andersson, “Reynolds number effects in the outer layer of the turbulent flow in a channel with rough walls,” *Physics of Fluids*, vol. 17, p. 065101, 2005.
- [74] G. Barenblatt, *Scaling, self-similarity, and intermediate asymptotics: dimensional analysis and intermediate asymptotics*, vol. 14. Cambridge University Press, 1996.
- [75] S. Bradford and B. Sanders, “Finite-volume model for shallow-water flooding of arbitrary topography,” *Journal of Hydraulic Engineering*,

- vol. 128, no. 3, pp. 289–298, 2002.
- [76] G. Brown, “The history of the Darcy-Weisbach equation for pipe flow resistance,” in *Proceedings of the 150th Anniversary Conference of ASCE* (Editors J. Rogers and A. Fredrich), pp. 34–43, 2002.
- [77] T. D. Butler, *Computational Measure Theoretic Approach to Inverse Sensitivity Analysis: Methods and Analysis*. PhD thesis, Fort Collins, CO, USA, 2009. AAI3385166.
- [78] V. Calo, N. Collier, M. Gehre, B. Jin, H. Radwan, and M. Santillana, “Gradient-based Estimation of Manning’s Friction Coefficient from Noisy Data,” *Journal of Computational and Applied Mathematics*, vol. 238, pp. 1–13, 2012.
- [79] F. Carollo, V. Ferro, and D. Termini, “Flow velocity measurements in vegetated channels,” *Journal of Hydraulic Engineering*, vol. 128, no. 7, pp. 664–673, 2002.
- [80] M. Carr, “Formation of Martian flood features by release of water from confined aquifers,” *Journal of Geophysical Research*, vol. 84, no. 13, pp. 2995–3007, 1979.
- [81] J. Christoffersen and I. Jonsson, “Bed friction and dissipation in a combined current and wave motion,” *Ocean Engineering*, vol. 12, no. 5, pp. 387–423, 1985.
- [82] S. Darby, “Effect of riparian vegetation on flow resistance and flood potential,” *Journal of Hydraulic Engineering*, vol. 125, no. 5, pp. 443–

454, 1999.

- [83] C. Dawson and J. Proft, “Coupled discontinuous and continuous galerkin finite element methods for the depth-integrated shallow water equations,” *Computer Methods in Applied Mechanics and Engineering*, vol. 193, no. 3, pp. 289–318, 2004.
- [84] S. L. Dingman and K. P. Sharma, “Statistical development and validation of discharge equations for natural channels,” *Journal of Hydrology*, vol. 199, no. 1, pp. 13–35, 1997.
- [85] C. R. Doering and P. Constantin, “Energy dissipation in shear driven turbulence,” *Phys. Rev. Lett.*, vol. 69, pp. 1648–1651, Sep 1992.
- [86] E. T. Engman, “Roughness coefficients for routing surface runoff,” *Journal of Irrigation and Drainage Engineering*, vol. 112, no. 1, pp. 39–53, 1986.
- [87] M. Fathi-Maghadam and N. Kouwen, “Nonrigid, nonsubmerged, vegetative roughness on floodplains,” *Journal of Hydraulic Engineering*, vol. 123, no. 1, pp. 51–57, 1997.
- [88] J. Finnigan, “Turbulence in Plant Canopies,” *Annual Review of Fluid Mechanics*, vol. 32, no. 1, pp. 519–571, 2000.
- [89] C. Fischenich, “Resistance due to vegetation,” tech. rep., DTIC Document, 2000.
- [90] G. Freeman, W. Rahmeyer, and R. Copeland, “Determination of resistance due to shrubs and woody vegetation,” tech. rep., DTIC Document,

2000.

- [91] G. E. Freeman, R. R. Copeland, W. Rahmeyer, and D. L. Derrick, “Field determination of manning’s n value for shrubs and woody vegetation,” *Proc. of the Wetlands Engineering River Restoration Conference, ASCE, Denver, Colorado*, 1998.
- [92] R. García Díaz, “Analysis of manning coefficient for small-depth flows on vegetated beds,” *Hydrological Processes*, vol. 19, no. 16, pp. 3221–3233, 2005.
- [93] L. Graham, T. Butler, C. Dawson, D. Estep, and J. J. Westerink, “Definition and solution of a stochastic inverse problem for the Manning’s n parameter field: Hurricane Gustav Case Studies,” *In Preparation*, 2015. In preparation.
- [94] W. Grant and O. Madsen, “The continental-shelf bottom boundary layer,” *Annual Review of Fluid Mechanics*, vol. 18, no. 1, pp. 265–305, 1986.
- [95] J. C. Green, “Effect of macrophyte spatial variability on channel resistance,” *Advances in Water Resources*, vol. 29, no. 3, pp. 426–438, 2006.
- [96] R. Hessel, V. Jetten, and Z. Guanghai, “Estimating Manning’s n for steep slopes,” *Catena*, vol. 54, no. 1, pp. 77–91, 2003.
- [97] C. Homer, J. Dewitz, J. Fry, M. Coan, N. Hossain, C. Larson, N. Herold, A. McKerrow, J. VanDriel, and J. Wickham, “Completion of the 2001 National Land Cover Database for the Conterminous United States,”

- Photogrammetric Engineering and Remote Sensing*, vol. 73, no. 4, p. 337, 2007.
- [98] M. Horritt, “A methodology for the validation of uncertain flood inundation models,” *Journal of Hydrology*, vol. 326, no. 1, pp. 153–165, 2006.
- [99] J. Järvelä, “Flow resistance of flexible and stiff vegetation: a flume study with natural plants,” *Journal of Hydrology*, vol. 269, no. 1, pp. 44–54, 2002.
- [100] C. James, A. Birkhead, A. Jordanova, and J. O’sullivan, “Flow resistance of emergent vegetation,” *Journal of Hydraulic Research*, vol. 42, no. 4, pp. 390–398, 2004.
- [101] P. A. Johnson, “Uncertainty of hydraulic parameters,” *Journal of hydraulic engineering*, vol. 122, no. 2, pp. 112–114, 1996.
- [102] R. Kadlec, “Overland flow in wetlands: vegetation resistance,” *Journal of Hydraulic Engineering*, vol. 116, no. 5, pp. 691–706, 1990.
- [103] A. Kennedy, U. Gravois, B. Zachry, R. Luettich, T. Whipple, R. Weaver, J. Reynolds-Fleming, Q. Chen, and R. Avissar, “Rapidly installed temporary gauging for hurricane waves and surge, and application to Hurricane Gustav,” *Continental Shelf Research*, vol. 30, no. 16, pp. 1743–1752, 2010.
- [104] I. Kinnmark, *The Shallow Water Wave Equations: Formulation, Analysis and Applications, Vol 15 of Lecture Notes in Engineering*. Springer-

Verlag, New York, 1985.

- [105] B. Kironoto and W. Graf, “Turbulence characteristics in rough uniform open-channel flow,” *Proceedings of the ICE - Water Maritime and Energy*, vol. 106, pp. 333–334, 01 December 1994.
- [106] G. Kite and N. Kouwen, “Watershed modeling using land classifications,” *Water Resources Research*, vol. 28, no. 12, pp. 3193–3200, 1992.
- [107] N. Kouwen, “Modern approach to design of grassed channels,” *Journal of irrigation and drainage engineering*, vol. 118, no. 5, pp. 733–743, 1992.
- [108] N. Kouwen and M. Fathi-Moghadam, “Friction factors for coniferous trees along rivers,” *Journal of Hydraulic Engineering*, vol. 126, no. 10, pp. 732–740, 2000.
- [109] N. Kouwen and R.-M. Li, “Biomechanics of vegetative channel linings,” *Journal of the Hydraulics Division*, vol. 106, no. 6, pp. 1085–1103, 1980.
- [110] P. Krogstad, R. Antonia, and L. Browne, “Comparison between rough- and smooth-wall turbulent boundary layers,” *Journal of Fluid Mechanics*, vol. 245, pp. 599–599, 1992.
- [111] D. Lawrence, “Macroscale surface roughness and frictional resistance in overland flow,” *Earth Surface Processes and Landforms*, vol. 22, no. 4, pp. 365–382, 1997.
- [112] D. Lawrence *et al.*, “Hydraulic resistance in overland flow during partial and marginal surface inundation: Experimental observations and modeling,” *Water Resources Research*, vol. 36, no. 8, pp. 2381–2393, 2000.

- [113] N. Loder, J. Irish, M. Cialone, and T. Wamsley, “Sensitivity of hurricane surge to morphological parameters of coastal wetlands,” *Estuarine, Coastal and Shelf Science*, vol. 84, no. 4, pp. 625–636, 2009.
- [114] D. Lynch and W. Gray, “A wave equation model for finite element tidal computations,” *Computers and Fluids*, vol. 7, pp. 207–228, 1979.
- [115] O. Madsen and M. Rosengaus, “Spectral wave attenuation by bottom friction: experiments,” in *Coastal Engineering (1988)*, pp. 849–857, ASCE, 1988.
- [116] W. A. Marcus, K. Roberts, L. Harvey, and G. Tackman, “An evaluation of methods for estimating manning’s n in small mountain streams,” *Mountain Research and Development*, pp. 227–239, 1992.
- [117] T. I. Marjoribanks, R. J. Hardy, and S. N. Lane, “The hydraulic description of vegetated river channels: the weaknesses of existing formulations and emerging alternatives,” *Wiley Interdisciplinary Reviews: Water*, vol. 1, no. 6, pp. 549–560, 2014.
- [118] D. C. Mason, D. M. Cobby, M. S. Horritt, and P. D. Bates, “Floodplain friction parameterization in two-dimensional river flood models using vegetation heights derived from airborne scanning laser altimetry,” *Hydrological Processes*, vol. 17, no. 9, pp. 1711–1732, 2003.
- [119] A. Mehta, “Bed friction characteristics of three tidal entrances,” *Coastal Engineering*, vol. 2, pp. 69–83, 1978.

- [120] M. Muleta and J. Nicklow, “Sensitivity and Uncertainty Analysis Coupled with Automatic Calibration for a Distributed Watershed Model,” *Journal of Hydrology*, vol. 306, no. 1, pp. 127–145, 2005.
- [121] H. Nepf, “Drag, turbulence, and diffusion in flow through emergent vegetation,” *Water resources research*, vol. 35, no. 2, pp. 479–489, 1999.
- [122] P. Nielsen, *Coastal bottom boundary layers and sediment transport*, vol. 4. River Edge, N.J: World Scientific, 1992.
- [123] T. Oden, R. Moser, and O. Ghattas, “Computer Predictions with Quantified Uncertainty,” tech. rep., The Institute for Computational Engineering and Sciences, The University of Texas at Austin, 2010.
- [124] S. Orlandini, “On the spatial variation of resistance to flow in upland channel networks,” *Water resources research*, vol. 38, no. 10, pp. 15–1, 2002.
- [125] F. Pappenberger, K. Beven, M. Horritt, and S. Blazkova, “Uncertainty in the calibration of effective roughness parameters in hec-ras using inundation and downstream level observations,” *Journal of Hydrology*, vol. 302, no. 1, pp. 46–69, 2005.
- [126] E. Pasche and G. Rouve, “Overbank flow with vegetatively roughened flood plains,” *Journal of Hydraulic Engineering*, vol. 111, no. 9, pp. 1262–1278, 1985.
- [127] O. Pouliquen, “Scaling laws in granular flows down rough inclined planes,” *Physics of fluids*, vol. 11, p. 542, 1999.

- [128] M. Raupach, R. Antonia, and S. Rajagopalan, “Rough-wall turbulent boundary layers,” *Appl. Mechanics Revs.*, vol. 44, pp. 1–25, 1991.
- [129] D. Schwanenberg and M. Harms, “Discontinuous Galerkin finite-element method for transcritical two-dimensional shallow water flows,” *Journal of Hydraulic Engineering*, vol. 130, no. 5, pp. 412–421, 2004.
- [130] J. Smith and S. McLean, “Spatially averaged flow over a wavy surface,” *Journal of Geophysical research*, vol. 82, no. 12, pp. 1735–1746, 1977.
- [131] I. Sraj, K. T. Mandli, O. M. Knio, C. N. Dawson, and I. Hoteit, “Uncertainty quantification and inference of manning’s friction coefficients using {DART} buoy data during the tōhoku tsunami,” *Ocean Modelling*, vol. 83, no. 0, pp. 82 – 97, 2014.
- [132] I. Takken and G. Govers, “Hydraulics of interrill overland flow on rough, bare soil surfaces,” *Earth Surface Processes and Landforms*, vol. 25, no. 13, pp. 1387–1402, 2000.
- [133] L. N. Trefethen, A. Trefethen, S. C. Reddy, T. A. Driscoll, *et al.*, “Hydrodynamic stability without eigenvalues,” *Science*, vol. 261, no. 5121, pp. 578–584, 1993.
- [134] T. Von Karman, “Progress in the statistical theory of turbulence,” *Proceedings of the National Academy of Sciences of the United States of America*, vol. 34, no. 11, p. 530, 1948.
- [135] T. Von Karman, “On the statistical theory of turbulence,” *Proceedings of the National Academy of Sciences of the United States of America*,

vol. 23, no. 2, p. 98, 1937.

- [136] C. Vreugdenhil, *Numerical Methods for Shallow Water Flow*. Kluwer Academic Publishers, Dordrecht, Germany, 1994.
- [137] J. J. Westerink, R. A. Luettich, J. C. Feyen, J. H. Atkinson, C. N. Dawson, H. J. Roberts, M. D. Powell, J. P. Dunion, E. J. Kubatko, and H. Pourtaheri, “A basin to channel scale unstructured grid hurricane storm surge model applied to southern Louisiana,” *Mon. Wea. Rev.*, vol. 136, pp. 833–864, 2008.
- [138] N. Wilson and R. Shaw, “A higher order closure model for canopy flow,” *Journal of Applied Meteorology*, vol. 16, no. 11, pp. 1197–1205, 1977.
- [139] E. E. Wohl, “Uncertainty in flood estimates associated with roughness coefficient,” *Journal of Hydraulic Engineering*, vol. 124, no. 2, pp. 219–223, 1998.
- [140] F. Wu, H. Shen, and Y. Chou, “Variation of roughness coefficients for unsubmerged and submerged vegetation,” *Journal of Hydraulic Engineering*, vol. 125, no. 9, pp. 934–942, 1999.
- [141] D. Yu and S. Lane, “Urban fluvial flood modelling using a two-dimensional diffusion-wave treatment, part 2: development of a sub-grid-scale treatment,” *Hydrological Processes*, vol. 20, no. 7, pp. 1567–1583, 2005.
- [142] D. Yu and S. N. Lane, “Urban fluvial flood modelling using a two-dimensional diffusion-wave treatment, part 1: mesh resolution effects,”

Hydrological Processes, vol. 20, no. 7, pp. 1541–1565, 2006.

- [143] “Hurricane Ike.” http://en.wikipedia.org/wiki/Hurricane_Ike, November 26 2012.
- [144] “Hurricane Katrina.” http://en.wikipedia.org/wiki/Hurricane_Katrina, Nov 26 2012.
- [145] “Hurricane Sandy.” http://en.wikipedia.org/wiki/Hurricane_Sandy, Nov 26 2012.

Vita

Lindley C. Graham was born in the Silicon Valley in California. In 2006, he entered the Massachusetts Institute of Technology in Cambridge, Massachusetts with a National Achievement Scholarship and the Robert C. Byrd Scholarship. During the summers of 2007 - 2009 he interned at Build-It-Yourself and Aurora Flight Sciences in Cambridge, Massachusetts, and at Jet Propulsion Laboratory as a part of the National Air and Space Administration Space Grant program. While at the Massachusetts Institute of Technology he also worked at the Humans and Automation Lab as an undergraduate student researcher. He received the degree of Bachelor of Science in Aerospace Engineering from the Massachusetts Institute of Technology in 2010. He began graduate studies at the Institute for Computational Engineering and Sciences at the University of Texas at Austin in 2010. He was awarded a National Science Foundation Graduation Research Fellowship (Grant. No. DGE-11100007) in 2011. He received the Master of Science degree in Computational Science, Engineering, and Mathematics in May, 2012.

Permanent address: lichgraham@gmail.com

This dissertation was typeset with L^AT_EX[†] by the author.

[†]L^AT_EX is a document preparation system developed by Leslie Lamport as a special version of Donald Knuth's T_EX Program.